REPUBLIQUE DU CAMEROUN
Paix – Travail – Patrie
****
UNIVERSITE DE YAOUNDE I
FACULTE DES SCIENCES
DEPARTEMENT DE PHYSIQUE
****
CENTRE DE RECHERCHE ET DE FORMATION
DOCTORALE EN SCIENCES, TECHNOLOGIES ET GEOSCIENCES
LABORATOIRE DE MECANIQUE, MATERIAUX ET STRUCTURES

REPUBLIC OF CAMEROUN
Peace – Work – Fatherland
****
UNIVERSITY OF YAOUNDE I
FACULTY OF SCIENCE
DEPARTMENT OF PHYSICS
****
POSTGRADUATE SCHOOL OF SCIENCES, TECHNOLOGY AND GEOSCIENCES
LABORATORY OF MECHANICS, MATERIALS AND STRUCTURES

Vibrations energy harvesters based on trees, cantilever beams, flexible tubes and variation of parameters

THESIS
Submitted in partial fulfilment of the requirements for the awards of Doctorat of Philosophy (Ph.D) degree in Physics

Par : **TOKOUE NGATCHA Dianorré**
Masters in Physics

Sous la direction de
WOAFO Paul
Professor

Année Académique : 2018

UNIVERSITÉ DE YAOUNDÉ I
UNIVERSITY OF YAOUNDE I

FACULTÉ DES SCIENCES
FACULTY OF SCIENCE

DÉPARTEMENT DE PHYSIQUE
DEPARTMENT OF PHYSICS

ATTESTATION DE CORRECTION DE LA THÈSE DE DOCTORAT/Ph.D

Nous, Professeur **NANA NBENDJO Blaise Roméo** et Professeur **KOFANE Timoléon Crépin**, respectivement Examinateur et Président du jury de la Thèse de Doctorat/Ph.D de Monsieur **TOKOUE NGATCHA Dianorré**, Matricule **10W1543**, préparée sous la supervision du Professeur **WOAFO Paul**, intitulée « **VIBRATIONS ENERGY HARVESTERS BASED ON TREES, CANTILEVR BEAMS, FLEXIBLE TUBES AND VARIATION OF PARAMETERS**», soutenue le **Mardi, 18 septembre 2018**, en vue de l'obtention du grade de Docteur/Ph.D en Physique, Spécialité **Mécanique, Matériaux et Structures,** Option **Mécanique Fondamentale et Systèmes Complexes,** attestons que toutes les corrections demandées par le jury de soutenance ont été effectuées.

En foi de quoi, la présente attestation lui est délivrée pour servir et valoir ce que de droit.

Fait à Yaoundé le 02 OCT 2018

Examinateur	Le Chef de Département de Physique	Le Président du jury
Prof. NANA NBENDJO Blaise Roméo	Prof. NDJAKA Jean-Marie Bienvenue	Prof. KOFANE Timoléon Crépin

Dedications

I dedicate this work :

- To my father Mr. ***NGATCHA*** named ***Chabeun Dja Kambeu***. Daddy, may you find in this work a real satisfaction. Today, I am what you always dreamed what I should be.

- To my mother Mrs. ***Deutchou Yvette***, whose love me. Mummy, everything is still clear in my mind as if it happened yesterday. 25 years ago, you held me by the hand to accompany me on the way to school. Mom a quarter of a century later, half a lifetime, I bring you this book marking the end of my studies. It only remains for me, to bring you the fruit of these 25 years of study. For this personal legacy, thank you Mum.

- To my brothers and sisters: Mr. ***Eromio Tchoketcha Ngatcha***, Mr. ***Bertrand Danga Ngatcha***, Mr. ***Calvier Tchoua Ngatcha***, Mr. ***Palvin Tchana Ngatcha***, Mrs. ***Synthianie Pamen Ngatcha***, Mrs. ***Leslie Ngatcha Ngatcha*** and my ***entire family*** for your patience and tolerance because I could not support you financially when you had much more need. After this art of passion, I promise you more than ever to meet your needs;

  Daddy, ***mummy***,***brothers and sisters*** you are my family and I am proud of each one of you. Beloved elder brother, although dead, you live in us. When you were born, Dad gave you the name ***TANKOUA***. Three days later, he added Jeanvion.***Jeanvion TANKOUA***, you were not only a brother, but also and especially a friend. You live forever in our hearts.

Acknowledgements

The present PhD work has been prepared in the Laboratory of Modelling and Simulation in Engineering, Biomimetics and Prototypes (LaMSEBP) of the Department of Physics, Faculty of Science, University of Yaounde I (UYI) Cameroon. Therefore I would like to acknowledge those who participated to its accomplishment.

– The Almighty Father for all his marvelous and overabundant gifts, the always living Lord Jesus for his precious teachings, the Holy Spirit for his unspeakable power;

– First, I would like to thank Prof. ***Paul WOAFO***, my supervisor for all his support and encouragement throughout the course of my research. I feel very privileged to have been given the opportunity to work with such a brilliant academic, and sincere person;

– I thank Prof. ***Jean-Marie Bienvenu NDJAKA***, the new head of the Department of Physics, Faculty of Science, UYI and the teaching staff of the Department for their valuable teachings and fruitful encouragements;

– I am grateful to Prof. ***Timoléon Crépin KOFANE***, the past head of the Department of Physics, Faculty of Science, UYI for his powerful management of the Department, valuable teachings and fruitful advices;

– I wish to express my acknowledgments to all the members of the jury who have accepted to discuss and appreciate the results of this thesis, in spite of their numerous duties: the president of jury Prof. ***Timoléon Crépin KOFANE***, of the University of Yaoundé I; the members of jury namely Prof. ***Bernard ESSIMBI ZOBO***, Prof. ***Clément TCHAWOUA***, Prof. ***Blaise Roméo NANA NBENDJO*** of the University of Yaoundé I and Prof. ***René YAMAPI*** of the University of Douala;

– I wish to express my acknowledgments to Prof. ***NANA Nbendjo***, my Masters thèsis promoter for the challenge he is by now, for most student in

the lab. May his principles and rigor open to him new horizon and major prospects;

– During the period of my PhD work, I recived assistance of LaMSEBP collaborator. Many thanks to Dr. ***NANA Bonaventure*** of the University of Bamenda, for the valuable exchanges, advices and for providing invaluable insight into the field of electrical generators and power conversion technologies. Receive my gratitude;

– I have the opportunity to express my thanks to all the teaching staff and personnel of the Department of Physics, Faculty of Science, for both University of Dschang and University of Yaoundé 1, for their valuable teachings and their fruitful advices since my first year in those institutions;

– I wish to express my thanks to Dr ***SIFEU TAKOUGANG Kingni*** of the University of Maroua for his encouragements advices and for reading this manuscript. Once more thank you;

– I thank also Dr ***ABOBDA Théodore Lejuste*** of the University of Yaoundé I, for the warm welcome in the laboratory, and for reading this manuscript;

– I would like to thank all my elders of LaMSEBP: Dr. ***TALLA Françis***, Mr. ***CHAMGOUE***, Mr. ***NOTUE KADJIE***, Dr. ***GOUNE chengui*** for your fruitful exchanges during my stay;

– I would like to thank all my lab mates batch of LaMSEBP: Mrs. ***TSAPLA FOTSA***, Mr. ***METSEBO***, Mr. ***NDEMANOU***, Mr. ***OUMBE TEUKAM***, Mr. ***NWAGOUM TUWA*** for fruitful interactions during the seminars and my presentations at the LaMSEBP;

– Ultimately, however, it is with the support of my closest friends and family that has made it possible for me to struggle through and come out at the other side. I thank each and every one of them for this, especially my girl friend, who has witnessed the whole process from beginning to end. All her patience, love and support make me realize just how lucky truly I am to have her in my life;

– Finally, to my darling Mother who is responsible for setting me on this path.....what shall we race for next?

Contents

List of Tables

List of Figures

List of Abbreviations

AC: **A**lternative **C**urrent
DC: ***D***irect ***C***urrent
CMOS: ***C***omplementary ***M***etal ***O***xide ***S***emiconductor
EHs: **E**nergy **H**arvesting
EHC: **E**nergy ***H***arvesting ***C***ircuit
eVEHs: **e**lectrostatics-**V**ibration **E**nergy **H**arvesting
FET: **F**ield **E**ffect **T**ransistor
LED: **L**ight **E**mitted **D**iode
LV: **L**ow **V**oltage
M2M: **M**achine-to-**M**achine
MEMs: **M**icro **E**lectromechanical **S**ystems
MOSFET: **M**etal **O**xide **S**emiconductor **F**ield **E**ffect **T**ransistor
ODEs: **O**rdinary **D**ifferential **E**quations
PA: **P**ower **A**mplifier
PDEs: **P**artial **D**ifferential **E**quations
PZT: **P**iezoelectric material
RK: **R**unge-**K**utta
SDEs: **S**tochastic **D**ifferential **E**quations
SPIH: **S**pringless **P**roximity **I**nertial **H**arvester
USB: **U**niversal **S**erial **B**us
VEHs: **V**ibration **E**nergy **H**arvesting
WANs: **W**ireless **A**ccess **N**etwork
WEH: **W**ind **E**nergy **H**arvesting
WSNs: **W**ireless **S**ensors **N**otes

Abstract

The aim of this thesis is to **study vibrations energy harvesters based on trees, cantilever beams, flexible tubes and variable geometric and physical parameters**. We first consider a design and testing of a device able of harvesting energy from trees vibrations. An experimental laboratory prototype constituted of a cantilever beam and an electromagnetic transducer is constructed. The vibration of the cantilever beam is generated by a rotative fan. We also investigate a pendulum electromechanical energy harvesting system (EHs) consisting of an electromechanical pendulum subjected to a wind excitation. The effects of a spring constant and of pendulum length have been analysed. For the both cases, the output voltage and power response of the system are analysed in terms of load resistance. A field investigation is carried out to find the amount of power that can be harvested with our device in our meteorological context. Because of the low-voltage amplitude of the vibration energy harvester (VEH), we propose a circuit to rectify and boost a low AC voltage to a high DC voltage. The circuitry uses Schottky diode and a voltage multiplier (octuplet) circuit for its optimum performance.

This thesis aims also focus on an electrostatic vibration energy harvester (e-VEH) system with variable area, variable permittivity, and variable radius. Nonlinear oscillator equations are established for each case, and solved analytically and numerically. The power produced by each configuration of the harvester is presented in terms of resistive load, frequency and external excitation.

A promising application is an increasing interest in the field of implantable biosensors. One of the application of this thesis considers the conversion of a pulsating fluid pressure in elastic tubes into electrical energy using a cylindrical electrostatic vibration energy harvester (e-VEH) attached to the tube. A special attention is paid on the case of blood flow in order to have energy that can be used to power artificial organs such as artificial pacemaker. It is found that the amount of power of the order of of $P_{\max} = 0.47\ mW$ can be obtained in the case of conversion of the pulsatile blood pressure into electrical energy for cylinder length of 30.0 mm and diameter of 25.0 mm.

Keywords: Vibration energy harvester, flow-induced-vibration, electromagnetic converters, electrostatic converters, AC-DC power conversion, Cylindrical electrostatic energy harvester, artificial pacemaker.

Résumé

L'objectif de cette thèse est d'**étudier les récupérateurs d'énergie basés sur les vibrations des plantes, des poutres en porte-à-faux, des tubes flexibles et la variation des caractéristiques géométriques et physiques**. Nous commençons par la conception et l'étude d'un dispositif capable de récolter de l'énergie à partir des vibrations des arbres. Un prototype expérimental de laboratoire constitué d'une poutre en porte-à-faux et d'un transducteur électromagnétique est construit. La vibration de la poutre en porte-à-faux est générée par un ventilateur rotatif. Nous étudions également un système de récolte d'énergie électromécanique pendulaire constitué d'un pendule électromécanique soumis à une excitation du vent. Les effets de la constante du ressort et de la longueur de pendule sont analysés. Pour les deux cas expérimentaux, la tension de sortie et la puissance électrique du système sont analysées en fonction de la résistance de charge. Un test sur le terrain est mené afin de déterminer la quantité de puissance qui peut être récoltée avec notre dispositif dans notre contexte météorologique. A cause de la faible-amplitude de tensions produites, nous avons proposé un circuit pour redresser et amplifier les faibles-tensions alternatives en des tensions continues élevées. Le circuit qui a été proposé utilise la diode Schottky et un multiplieur de tension (octuplet) pour sa performance optimale.

Un autre objectif de cette thèse est de mettre un accent sur les récupérateurs d'énergie à transduction électrostatique avec une surface variable, une permittivité variable et un rayon variable. La puissance produite par chaque configuration est présentée en fonction de la résistance de charge, de la fréquence et de l'amplitude d'excitation externe.

L'une des applications de ce travail considère la conversion des vibrations des artères due aux impulsions sanguines ou de la pression des fluides dans des tubes élastiques en énergie électrique en utilisant les convertisseurs d'énergie électrostatique de forme cylindrique et fixé au tube. Une attention particulière est portée sur le cas du flux sanguin afin d'avoir de l'énergie qui peut être utilisée pour alimenter des organes artificiels tels que le stimulateur artificiel. On constate qu'une puissance de l'ordre de $P_{\max} = 0.47\ mW$, peut être obtenue dans le cas de la conversion de la pulsation artérielle en énergie électrique pour un capteur de longueur $30.0\ mm$ et de diamètre $25.0\ mm$.

Mots clés: Récupérateur d'énergie vibrante, convertisseurs électromagnétiques, convertisseurs électrostatiques, conversion de courant AC-DC, récupérateur d'énergie électrostatique cylindrique, activateur cardiaque artificiel.

General Introduction

Modern conjecture reserves the use of the term *energy harvesting* (EHs) or *energy scavenging* to describe the process by which energy is harvested from ambient resources such as wind, solar radiation, thermal gradients and vibrations/motions to be either stored or used directly to power low-energy electronics (typically in the microwatt order), or to be used in the field of implantable biosensors. Energy harvesting is the scavenging of ambient energy in order to make an autonomous power of electronic devices for numerous applications, most particularly electronics and electrical systems ranging from wireless sensor networks (WSNs) to medical implants [1]-[4]. In past decade, this field of research has generated a lot of interest within the scientific community and industrial area since it provides a route for the realization of alternatives for the conventional battery.

Vibration-powered generators are typically, although not exclusively, inertial spring and mass systems. The transduction mechanisms are employed to extract energy from kinetic energy system. Kinetic energy generators convert energy in the form of mechanical movement present in the application environment into electrical energy. Transducers have been recently implemented in several designs for fluid flow energy harvesting. They are envisioned for use in generating micro- and milli-watts for powering remote sensor networks and small-scale electronic devices. Wireless systems are becoming ubiquitous; examples include Wireless sensor networks (WSNs) which have become a very significant enabling technology over the past few years [5]. Wireless sensor nodes can be used in many important fields such as remote environmental monitoring, bearing fault diagnosis and target tracking due to the advantages of small size, cheap cost, and intelligence [6]-[8]. Usually, the power supply of the wireless sensor network is mostly designed to be based on batteries which have limited lifetimes, either needing to be replaced or

the fuel replenished from time to time.

Mechanical vibration energy, as a potential power source for wireless sensor nodes, has received much more attention from researchers all over the world. The use of sensor networks for remote monitoring within forests is becoming widespread. Use of these networks in forests is occurring for detection and monitoring of forest fires [9], monitoring of various environmental data [10], monitoring wildlife passages [11] and much more. We conceived the idea of harvesting energy from tree movement due to the problem of energy supply that currently affects users of remote wireless sensors nodes located under the canopies of trees in forests [10].

Trees and plants are the remarkable elements which are always presents in our environment. During the airflow, they are excited and then, vibrated. These observation of trees/plants vibrations as results of wind flow show the gradual participation of the trees/plants as far as the wind flow intensity increases. Those vibrations are always permanently present and unexploited. Then comes the idea to exploit vibrational trees motion into electrical energy through transducer mechanisms. In literature, trees/plants are treated as beams. Beams are three dimensional structures, where two dimensions are negligible according to the third dimension. Depending to their boundaries conditions, trees/plants are treated as a cantilever beams. The case of cantilever beams as a typical dynamic system in engineering, link to simply illustrated the characteristics of a system on its modal base.

Enthusiasm in the emerging field of mechatronics has driven several energy transducer designs. Significant amount of energy harvesting research works has been conducted with a focus on piezoelectric materials, which generate a voltage upon the application of mechanical stress. Results thus far have been promising, as the materials generate a high voltage useful for manipulation in electrical circuitry. An alternative to the piezoelectric approach is the method of employing electromagnetic induction or electrostatic mechanism. Of these, electrostatic devices are found to be the most suitable approach for harvesting mechanical energy for micro application since they are compact, sensitive to low level mechanical energy, easier to integrate in small scale systems, not requiring smart materials, simple

to fabricate, inexpensive and simply structured using less circuitry. The above transduction mechanisms can be attached on trees and thus constitute nodes for energy harvesting. This problem has not yet be considered.

The first aim of this thesis is devoted to the **conversion of trees and cantilever beams vibrations into electrical energy**. The concept of macro energy harvesting from ambient vibration has been a subject of great attention in recent years. Many researchers have considered the design and performance optimization of vibration energy harvesters due to air flow [12]-[16]. And also, the concept of micro application, the use of biomedical sensors and instrumentation for monitoring patient health will be an important tool in the near future. Sensor networks are often deployed in conditions of minimal lighting and thermal gradient such as densely wooded environments, where even normal wind energy harvesting is limited. Although the principle of electromagnetic induction has been used for many years to harvest mechanical energy, we will first use this mechanism to answer this question: ***can the motion of the trees themselves be a possible source of energy harvester?*** The originality of this first part, is the combination of experimental and theoretical analysis as well as the consideration of a tree as mechanical system. In other way, the use of pendulum to harvest energy has been considered recently [14], [17]-[19]. Here, ***we investigate experimentally and theoretically on the parameters which can affect an electromechanical pendulum energy harvesting system (EHS) subjected to a wind excitation***. The effects of a spring constant and of pendulum length will be analysed.

The power level of the vibrational micro generators is very low, ranging from few microwatts to tens of mille watts, appearing in AC form. But the electronic loads require DC voltage for their operation. Therefore, the AC voltage of the vibrational micro generator output has to be processed by a suitable power converter to produce the required and applicable DC voltage for the load. We thus address two major challenges: a) ***how to efficiently convert low AC voltage waveform to DC voltage?*** and b) ***how to boost the low voltage to a sufficiently high level to charge a battery?***

Fixing electrostatic energy harvesters on trees may lead to the variation of its

geometrical parameters resulting on the variation of capacitance, plate area, and distance between the plates. One can also use a special mechanism so that tree or beam vibration result in the variation of permittivity of the material between the plates of electrostatic energy harvester. In that case, an analysis is required. This leads to the second device analysed in this thesis with the following questions: ***How does the variation of the electrostatic energy harvester parameters affects the characteristics of the generated electrical energy?*** Some electrostatic energy harvester configurations comparable to what is considered had been analysed. For instance Yildiring and Külah [20] proposed an electrostatic energy harvesting technique utilizing droplet-based micro flow for continuous power generation. Dudka et *al.* [21] study focused on the architecture of a wideband electrostatic vibration energy harvester having a low start-up voltage employing a high-voltage integrated interface. Recently, Basset et *al.* [22] presented an advanced study of an electrostatic vibration energy harvester with combined effect of electrical nonlinearities and mechanical impact. However, a study considering the main variable parameters is not yet available.

Today, there is an increasing interest in the field of implantable biosensors. A promising application is the use of implanted electrode arrays. The last question of this thesis is: ***Can we extend the electrostatic configuration of electrostatic energy harvester to convert the expansion and contraction of an artery (due to pulsatile blood pressure changes) into electrical energy?***

Therefore, the main problems considered in the thesis are follows:

- ♠ Put in place energy harvesters which convert the trees vibration into electrical energy: carry out the study theoretically, experimentally on prototypes and in the field;
- ♠ Design and study a new AC-DC power amplifier;
- ♠ Analyzed the effects of variation of parameters of an electrostatic energy harvester;
- ♠ Extend the electrostatic energy harvester to the conversion of artery vibration into electricity.

The thesis structure is as follows. After the general introduction, we will first present in ***chapter one*** a literature review on previous research works on energy harvesters. Next, we will present in ***chapter two*** the mathematical, numerical and experimental methods used to solve the problems of this thesis. The ***chapter three*** will present the results for the magnetic conversion of tree/beam vibration into electrical energy. ***chapter four*** deals with the results on electrostatic conversion of tree/beam vibration into electrical energy with an extension to the conversion of pulsatile blood pressure into electrical energy. Finally, a general conclusion will be given containing the main results obtained in the thesis and some perspectives.

Chapter One

Literature review

1.1 Introduction

This chapter first concentrates on review of vibrational energy harvesters and the conversion mechanism for useful application in engineering. Secondly, we present an electrical circuit for power rectification and boosting. Next, wind induced vibration on trees is presented. We end with the problem statement.

1.2 General theory of vibration-to-electricity conversion methods

Energy harvesting is the process by which energy readily available from the environment is captured and converted into usable electrical energy. Some EHs sources such as motion or vibrations has been demonstrated as a viable alternative to batteries to power electronic devices. Energy harvesting methods are categorized into two major groups including motive and non-motive. The motive class contains mostly vibrational and kinetic energy transforming method such as piezoelectric [23]-[30], electromagnetic [31]-[36], electrostatic [37]-[43], and magnetostrictive [44]-[46] conversions, while the non-motive one, includes solar, thermal conversions and etc [3].

Kinetic energy harvesting requires a transduction mechanism to generate electrical energy from motion, and the generator will require a mechanical system that couples environmental displacements to the transduction mechanism. The design of the mechanical system should maximize the coupling between the kinetic energy source and the transduction mechanism and will depend entirely upon the characteristics of the environmental motion. Vibrational tree energy is best suited

to electromagnetic generators with the mechanical magnet component attached to a cantilever beam which acts as the fixed coil reference [41]. The cantilever beam transmits the vibrations to the attached magnet producing a relative displacement between a fixed coil reference. Such a system will possess a resonant frequency which can be designed to match the characteristic frequency of the application environment. This approach magnifies the environmental vibration amplitude by the quality factor of the resonant system.

The transduction mechanism itself can generate electricity by exploiting the relative displacement occurring within the system. In this case of relative displacement, either the velocity or position can be coupled to a transduction mechanism. Velocity is typically associated with electromagnetic transduction while relative position is associated with electrostatic transduction. Each transduction mechanism exhibits different damping characteristics and this should be taken into consideration while modelling the generators. The mechanical system can be increased in complexity, for example, by coupling linear displacements into rotary generators.

1.2.1 Piezoelectric Converter

Piezoelectric ceramics have been used for many years to convert mechanical energy into electrical energy [41]. This sub-section describes the range of up to date piezoelectric generators described in the literature. The piezoelectric effect was discovered by *Jacques Curie* and *Pierre Curie* in 1880. They found that if certain crystals were subjected to mechanical strain, they became electrically polarized and the degree of polarization was proportional to the applied strain. Conversely, these materials deform when exposed to an electric field. Piezoelectric materials are widely available in many forms including single crystal (e.g. quartz), piezoceramic (e.g. lead zirconate titanate or PZT), thin film (e.g. sputtered zinc oxide), screen printable thick-films based upon piezoceramic powders [47], [48] and polymeric materials such as polyvinylidenefluoride (PVDF) [49] as shown in Fig. 1.1.

From the literature review, it can be surmised that piezoelectric-based vibration energy harvesting devices are very often configured as a cantilever beam with

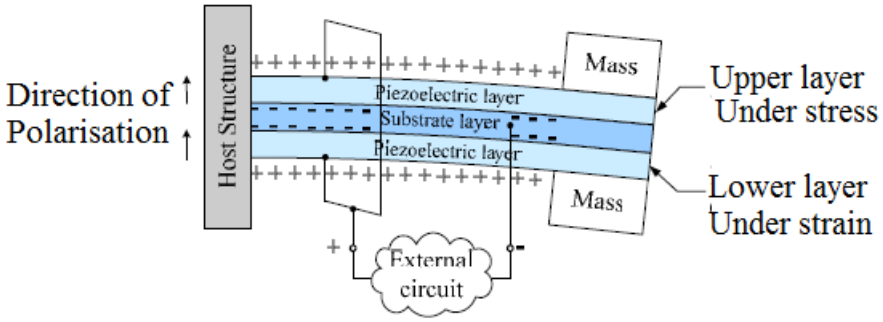

Figure 1.1: *Schematics of a unimorph piezoelectric cantilever-based vibration energy harvesting devices.*

an end mass, as shown in Fig. 1.1. There is good reason for this: a cantilever results in one of the least stiff structures for a given volume. This means that the cantilever offers both a low resonant frequency and a high average strain in its materials for a given volume. Both of these characteristics are useful for a vibration energy harvester; a high average strain in the piezoelectric layers translates directly into a high power output and, from information gleaned from the literature review, it seems that the higher acceleration amplitude vibrations tend to occur at the lower frequency values, i.e. below 200 Hz [35], [50].

1.2.2 Electromagnetic converter

Electromagnetic induction, discovered by *Faraday* in 1831, is the generation of electric current in a conductor located within a magnetic field. The conductor typically takes the form of a coil and the electricity is generated by either the relative movement of the magnet and coil, or because of changes in the magnetic field. In the former case, the amount of electricity generated depends upon the strength of the magnetic field, the velocity of the relative motion and the number of turns of the coil. One of the most effective methods for energy harvesting is to produce electromagnetic induction by means of permanent magnets, a coil and a resonating cantilever beam [41]. In principle, either the magnets or the coil can be chosen to be mounted on the beam while the other remains fixed. It is generally preferable, however, to have the magnets attached to the beam as these can act as the inertial mass as shown in Fig. 1.2.

The generalized schematic diagram depicted in Fig.1.2 is applicable to describe

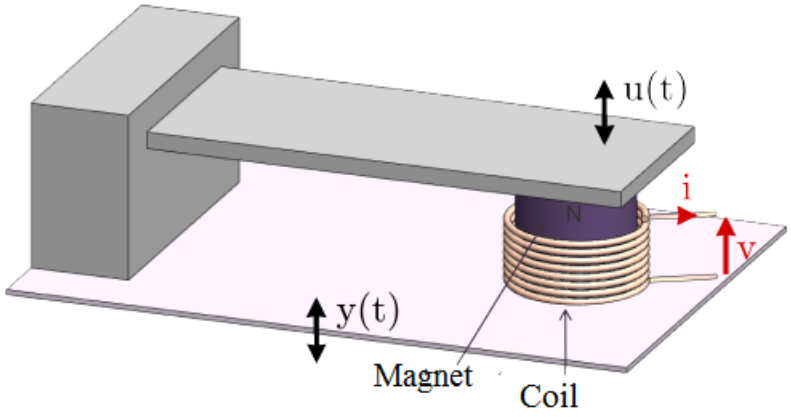

Figure 1.2: *The generalized schematic diagram of electromagnetic transducer structure.*

the operation of electromagnetic generators. The damper c, effectively represents the electromagnetic transduction mechanism, i.e. the magnet and coil arrangement.

1.2.3 Electrostatic converter

This subsection is devoted to electrostatic generators. Initially the basic concepts and operating principles are outlined. A review of electrostatic-based generators published to date is presented as well as their structure and an outline of their performance. A capacitor consists of two plates which are electrically isolated from each other typically by air, vacuum or an insulator. The charging of the plates by a battery of voltage V creates equal but opposite charges on the plates, Q leading to a storage of the charge when the voltage source is disconnected. The fundamental definition of the capacitance of such a capacitor is given by

$$C = \frac{Q}{V}, \tag{1.1}$$

where C is the capacitance in farads, Q is the charge on the plate in coulombs and V is the voltage on the plates in volts. For a parallel plate capacitor, C is given by

$$C = \varepsilon \frac{A}{d}, \tag{1.2}$$

where ε is the permittivity of the material between the plates in Fm^{-1} , A is the area of the plates in m^2 and d is the gap between the plates in meter (m).

If ε_0 is the permittivity of free space, Eqs. (1- 2) can be expressed in terms of the dielectric constant or relative permittivity, $k = \varepsilon_r = \varepsilon/\varepsilon_0$, of the insulator material:

$$C = k\varepsilon_0 \frac{A}{d}. \tag{1.3}$$

The voltage across a parallel plate capacitor is given by

$$V = \frac{Qd}{\varepsilon A}. \tag{1.4}$$

The energy stored in a capacitor, with plate charge Q and potential difference V, is given by

$$E = \frac{QV}{2} = \frac{CV^2}{2} = \frac{Q^2}{2C}. \tag{1.5}$$

If the charge on the plates is held constant the perpendicular force between the plates is given by

$$F = \frac{Q^2 d}{2\varepsilon A}. \tag{1.6}$$

If the voltage between the plates is held constant the perpendicular force between the plates is given by

$$F = \frac{\varepsilon A V^2}{2d}. \tag{1.7}$$

The work done against the electrostatic force between the plates provides the harvested energy. Electrostatic generators can be classified into three type [51]: (1). In-plane overlap varying. (2). In-plane gap closing. (3). Out-of-plane gap closing. These are illustrated in Fig. 1.3 [52].

Electrostatic devices can be divided into two categories:

– Electret-free electrostatic devices that use energy cycles to convert mechanical energy into electrical energy.

Electret-free devices operate in either charge- or voltage-constrained systems. So there are two possible extremes of operation. In both cases, the mechanical work done is converted into electrical energy.

– Electret-based electrostatic devices that use electrets to directly convert mechanical energy into electricity.

Electret-based devices are very similar to electret free devices. The main difference is the additional electret layers that are applied to one or both plates of the

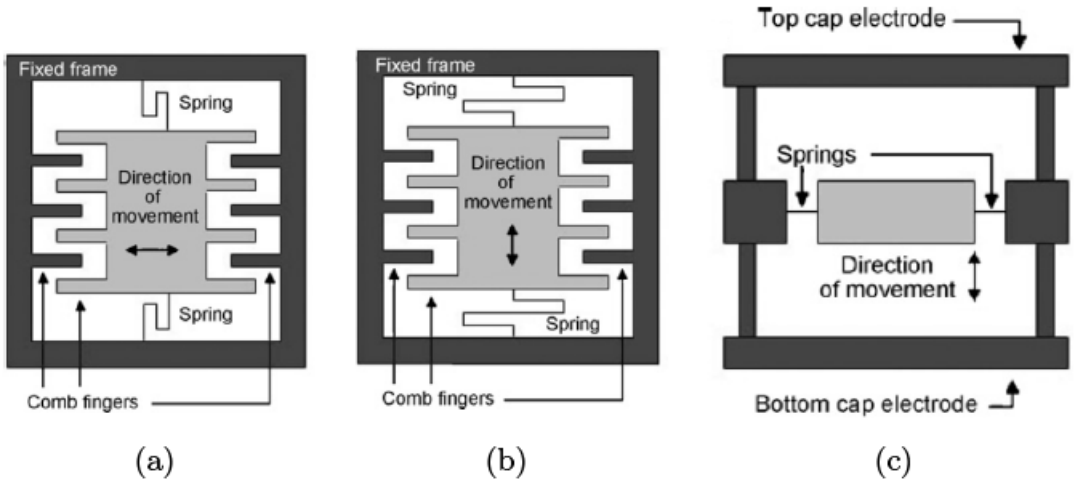

Figure 1.3: *Schematic of different types of Electrostatic generators: (a) In-plane overlap varying, (b) In-plane gap closing, (c) Out-of-plane gap closing [52].*

capacitor for polarisation purposes as described in Table 1.1.

Table 1.1: Electrostatic force variation for the three configurations.

Structure	**Charge constrained**	**Voltage constrained**
In-plane overlap varying	$F_e \propto 1/x^2$	F_e constant
In-plane gap closing	$F_e \propto x$	$F_e \propto 1/x^2$
Out-of-plane gap closing	F_e constant	$F_e \propto 1/x$

Where x is the gap between the plates and F_e the electrostatic force.
VEHs with electrostatic transduction (e-VEH) display interesting features that can make a difference with the other transduction mechanisms. They are particularly suitable for fabrication using silicon-based microelectromechanical systems (MEMS) technologies through a full batch fabrication process [53]-[55].

1.2.4 Other converters.

Other microgenerators use the magnetostrictive properties of ferromagnetic materials, i.e. their ability to deform under the application of magnetic field. The most commonly used material, due to its good magnetostrictive properties, is Tefenol-D. At magnetic saturation, the maximum relative deformation of this material can reach 1.6 $\mu m/cm$. In the case of energy harvester (EH), generators have been

developed using the magnetostrictive effect alone. This is the case of Wang et *al.* [56] of North Carolina State University, who exploit the reverse magnetostrictive effect by placing a magnetostrictive material directly on a beam. The deformation induce a magnetic field which will vary inside a coil, creating an electric current (Fig. 1.4 (a)). Their prototype harvest 200 μm and 0.15 V at 58 Hz.

A second approach for using the properties of Terfenol D is the exploitation of the important stresses generated to deform a piezoelectric material sandwiched between two magnetostrictive plates (Fig. 1.4 (b)). For example, this type of PZT-Terfenol hybrid converter has been implemented by Dai et al of the University of Chongqing in China, which recover a power of 1.1 V for 1 g of acceleration at 50 Hz [57].

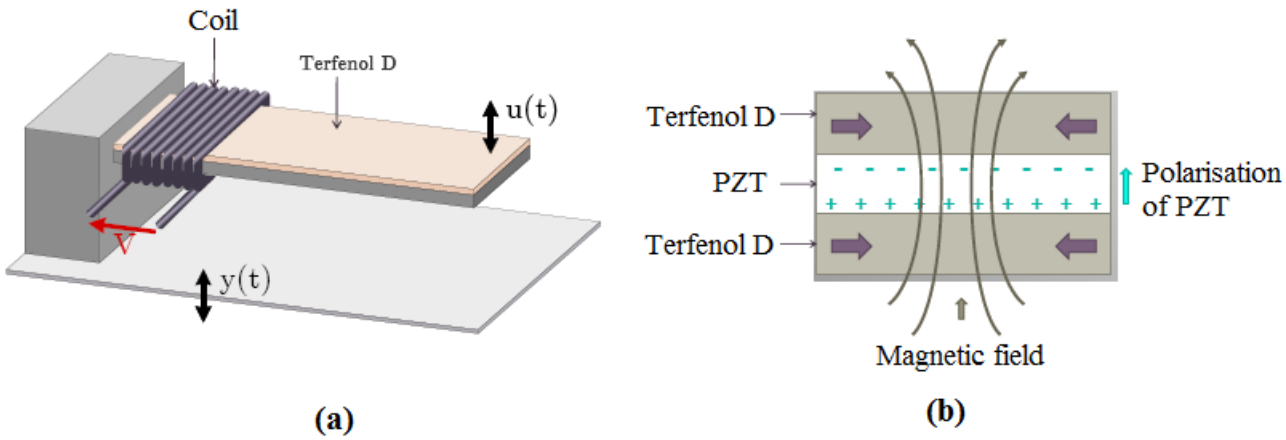

Figure 1.4: *Useful Principles of magnetostrictive generator for vibration energy harvester: (a) Useful of effect alone, (b) Experimental structure of converter.*

Assessment of mechanical energy converters

Each type of converter has both advantages and disadvantages, as described in Table 1.2

Table 1.2: Advantages and disadvantages of mechanical energy converters.

Type of converter	**Advantages**	**Disadvantages**
Piezoelectric	.High output voltage .High capacitance .No mechanical stops needed .High energy density .No separate external energy source Needed . Compatible with micro fabrication .No need to control gaps	.Not compatible with standard CMOS processes .Piezoelectric materials have poor coupling coefficients .Depolarization and ageing problems .Charge leakage and high output impedance . Brittle and expensive material
Electromagnetic	.No separate external voltage source is needed .No mechanical stops are needed needed .High output current .Long life .Robustness	.Bulk and cannot be scaled well to smaller size . Difficult to integrate with micro systems .Difficult to fabricate .Low output voltage .Expensive material .Low efficiency at low frequencies
Electrostatic	.Easier to integrate with micro systems and electronics .High output voltage .Low cost systems can be built .High coupling coefficient .No smart materials needed .Can be scaled well to smaller size	. Low capacitance .Separate voltage sources are sometimes needed .Mechanical stops needed .Capacitance causes damping, which reduces motion .High impact of parasitic Capacitance .Need to control gaps or plates area
Magnetostrictive	.High coupling force .No polarization .Flexibility	.Difficult to integrate with MEMS .Brittle material .Nonlinear effect .Need of eventual magnet of polarization

The problem that each approach must address is that low-frequency vibration is only sufficient to generate an extremely low output of power. To overcome this difficult challenge, we selected the electrostatic method because of its potential to achieve low frequency power generation. In addition, among energy conversion

principle, the electromagnetic micro generators have the highest energy density [42], [58]. Electromagnetic and electrostatic micro generators are hence considered for this work. The output voltage of those describe mechanism transduction produce low-AC-voltage. For the practical application, this voltage need to be transform, then the following subsection present an electrical circuit of rectifier and amplifier of vibrational energy harvesting.

1.3 Electrical circuit of rectifier and amplifier of vibrational energy harvesting

Vibration-driven generators are very attractive due to the availability of the vibration energy in the environment. The typical output voltage of an electromagnetic microgenerator is sinusoidal and the voltage amplitude is very low. Due to practical demands, a fair amount of attention has been focused recently on low-voltage ($<$1 V) energy harvesting circuits [59]-[64]. These efforts aim to address two major challenges: a) how to efficiently convert low AC voltage waveform to DC voltage (necessary for vibrational and RF energy harvesters [62]), and b) how to boost the low voltage to a sufficiently high level to charge a battery. A highly efficiency power management circuit is as important as the harvester itself. The micro generator output has to be proceeded by power converter to produce a suitable DC output voltage to meet the requirement of the end application. There are significant challenges in converting the power generated from such devices to usable form. For this reason, numerous works have been published on the energy harvester power management circuits. In 2006, Stark et *al.* [65], proposed an interesting converter for micro power electrostatic generators. In 2007, Xu et *al.* [66] designed, fabricated and tested a pulsed- resonant AC-DC converter for harvesting energy from low-voltage (of about 1.2 V) and low power ($1-100\ \mu W$) with output frequency in the $10\ Hz - 1\ kHz$ range. In 2010, Dwari and Parsa [62] presented an AC-DC step-up converter for low voltage energy harvesting. This consists of a boost converter in parallel with a buck-boost converter, which are operated in the positive half cycle and negative half cycle respectively. In 2011, Cheng et *al.* [64] proposed a circuit for voltage multiplication of self-powered AC/DC con-

verter with (0.35 V) minimum input. This constitutes an improvement of the former converters which require external power supply or a self-start up circuitry to achieve usable voltage level when the ambient energy level is relatively low.

1.3.1 Different types of rectifiers and amplifiers circuits

Generally, the AC-DC converter consists of a full-bridge diode rectifier, a dc-link capacitor and a high frequency DC-DC converter. To address the problems of the conventional two-stage converters, direct AC-to-DC converters are proposed [65]-[67]. This arrangement of two-stage power conversion has several disadvantages for the electromagnetic micro generator: 1) Diode voltages in a bridge rectifier are difficult to overcome for low input voltage; 2) input current is much higher than output current, leading to more losses in diodes; and 3) a rectifier offers a nonlinear load, which makes the converter unsuitable for energy harvesting.

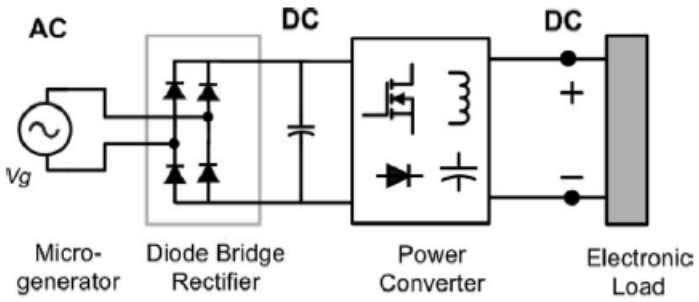

Figure 1.5: *Block diagrams of Conventional two-stages power conversion consisting diode bridge rectifier [65]-[67].*

The conventional power converters use diode bridge rectifiers and condition the micro generator outputs in two stages (Fig.1.5). Hence, they are inefficient and may not be a feasible option for very low voltage micro generators. Moreover, they are not conducive for optimum energy harvesting.

To address these issues, direct AC-DC boost converters can be used. A dual-polarity boost converter (Fig. 1.6) topology for such AC-DC conversion was recently reported in [58].

This converter uses two inductors, and the output DC bus is split into two series-connected capacitors. The fundamental principle behind the proposed topology

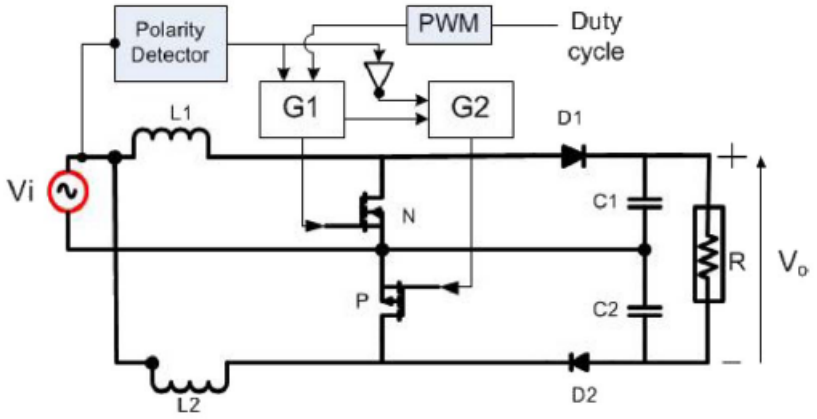

Figure 1.6: *Block diagram: Reported dual polarity boost converter [58].*

is the use of two boost converters, each operating in one half cycle of the AC voltage. Each capacitor is charged only in the respective half cycle. However, they discharge to the load, continuously causing large voltage drops. Extremely large capacitors are needed to make the voltage ripple acceptable. This makes the converter response very slow.

A single-stage boost type power converter Fig.1.7 was proposed by Dwari et *al.* [62]. In these converters, bridge rectification is avoided.

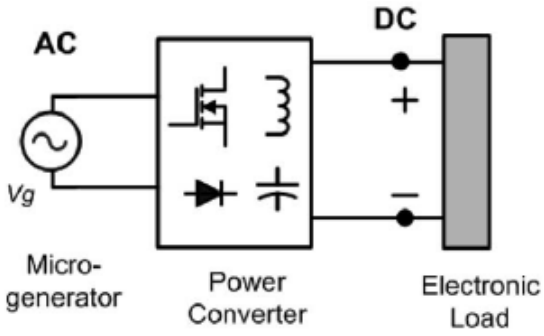

Figure 1.7: *Block diagrams of Conventional Direct ac-to-dc power conversion [62].*

A direct AC-to-DC converter is proposed in [68]. The proposed converter, as shown in Fig. 1.8, consists of a boost converter (inductor $L1$, switch $S1$, and diode $D1$) in parallel with a buck-boost converter (inductor $L2$, switch $S2$, and diode $D2$). In this converter, the negative output to input voltage gain of a buck-boost converter is utilized to step-up the negative half input voltage of the micro generator to a positive high- DC output voltage. The output DC bus is realized by using

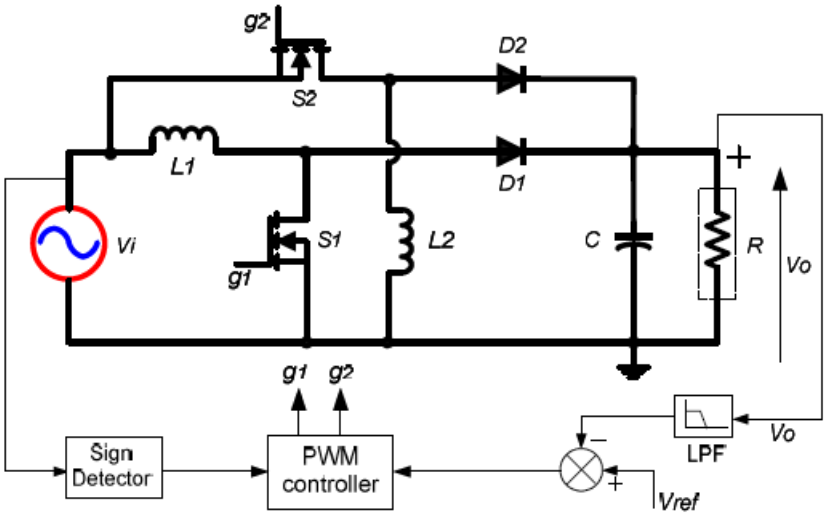

Figure 1.8: *Proposed direct ac-to-dc converter [68].*

a single capacitor. The output capacitor is charged by the boost converter in the positive half cycle and by the buck-boost converter in the negative half cycle. Therefore, it resolves the problems present in a dual-polarity boost converter. Rohan Dayal et *al.*, 2011 [60] proposed split-capacitor topology utilizes an n- and p-MOSFET pair to form the bidirectional switch which does not need floating gate drivers. The circuit diagram for the split-capacitor topology is shown in Fig. 1.9. A single inductor L is used for the boost operation in both half cycles. The converter utilizes three capacitors to boost the low a AC voltage. Split capacitors $C2$ and $C3$ are charged in alternate half cycles.

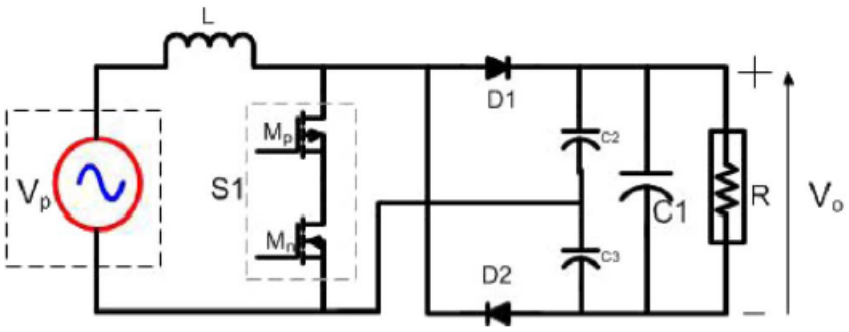

Figure 1.9: *Proposed direct ac-dc converter: Split-capacitor topology [60].*

Looking through literature, one can realize that: (1) these converters absorb energy from the AC line only when the rectified line voltage is higher than the DC

link voltage; therefore, (2) these kinds of converters need input current supply for a start-up circuit. The control of the converter also requires input line polarity sensing; in another hand, (3) these converter response is very slow. For a low-power application, it is difficult to realize such drivers. One of the aim of this thesis is to find a way to design the harvesting circuitry (i.e. the circuitry that is usually connected to the generator to condition and/or manage the generated electrical power) such that it boosts the output power level of the device.
The electrical circuit is analysed. First a load resistance circuit is used to assess the performance of the harvester. Next a basic energy storing circuit is examined that stores the generated energy inside a capacitor.

1.3.2 Circuit with load resistance

A circuit with load resistance is shown in Fig. 1.10.

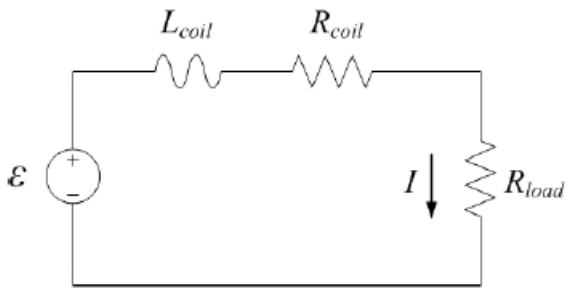

Figure 1.10: *Load resistor circuit.*

The coil is modeled as a series connection of the harvester input voltage ($e(t) = \varepsilon$) induced by the moving magnet, a coil inductance (L_{coil}), and a coil resistance (R_{coil}). A load resistor (R_{load}) is connected to the coil and completes the electrical circuit. When the magnet is moving and inducing a voltage, a current (I) flows through the circuit. To find the circuit equation, one can apply *Kirchhoff's* voltage law by summing voltage rises clockwise around the circuit. This gives

$$e(t) - L_{Coil}\frac{di(t)}{dt} - (R_{coil} + R_{load})\, i(t) = 0 \tag{1.8}$$

Invoking the coupling relation between the induced voltage and the radial velocity of the magnet,

$$e(t) = -Bl\dot{x} \tag{1.9}$$

the circuit equation becomes

$$L_{Coil}\frac{di(t)}{dt} + (R_{coil} + R_{load})\, i(t) = -Bl\dot{x} \tag{1.10}$$

Because the induced voltage depends upon the coupling factor and the radial velocity of the magnet, the current through the coil will depend upon the position and velocity of the magnet.

– If the coil is not connected to an external circuit, then:
$i(t) = 0$, and $e(t) = -Bl\dot{x}$ which is the induced voltage.

– If the coil is connected to a variable resistance R_{load}, then: $i(t) \neq 0$, and $e(t) = V_{load} = R_{load}i(t)$ which is the voltage across the load resistor. The potential useful power produced by the harvester is the power dissipated across the load resistor. This power (P_{load}) is

$$P_{load} = R_{load}i^2(t) = \frac{V_{load}^2}{R_{load}}. \tag{1.11}$$

The total energy consumed by the load resistor (E_{load}) is

$$E_{load} = \int_{t=0}^{T} P_{load}dt, \tag{1.12}$$

where T is the run time of a numerical simulation or the run time of the experiment. The average power ($\bar{P}_{load}$) is this energy divided by the run time, or

$$\bar{P}_{load} = \frac{E_{load}}{T} = \frac{1}{T}\int_{t=0}^{T} P_{load}dt. \tag{1.13}$$

1.3.3 Circuit in presence of energy storage

Due to the load resistor circuit only dissipates the generated energy, an energy storage circuit is needed. In literature some interested circuits have been developed

to efficiently store electrical power and regulate the voltage to a load circuit [59], [60], [62], [64]. In the works of D. J. Inman et *al.* [3], a basic energy storage circuit was implemented to simplify the analysis and to demonstrate the harvester's ability to produce and store useful energy. Fig. 1.11 shows the schematic of this circuit.

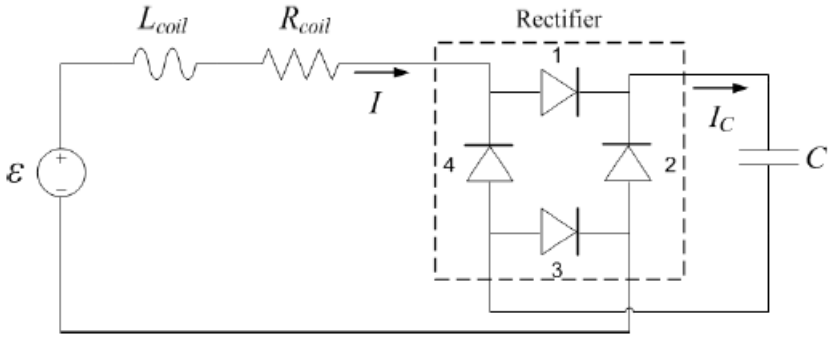

Figure 1.11: *Basic energy storing circuit.*

The coil is again treated as an input voltage in series with an inductor and a resistor. The terminals of the coil are connected to a full wave rectifier, and the outputs of the rectifier are connected to a capacitor (C). The rectifier is a bridge circuit consisting of four diodes. An alternating current (I) enters the full wave rectifier and is converted into a direct current (I_C). The direct current from the rectifier maintains a consistent voltage polarity across the capacitor. This prevents the alternating current from the coil from damaging the capacitor. The diode bridge also prevents the capacitor from discharging through the coil when energy is not being produced. There is a minimum voltage required to bias the diodes in the bridge. This results in some loss of output voltage from the rectifier and consequently some loss of energy. For the basic energy storage circuit in Fig. 1.11, the amount of charge stored on the capacitor (q) is

$$q(t) = q(0) + \int_{\tau=0}^{t} i(\tau) d\tau. \tag{1.14}$$

Where $q(0) = q_0$ is the initial amount of charge on the capacitor and τ is a dummy variable. The energy stored on the capacitor E_C is define in Eqs. (1.5) and the voltage across the capacitor is given in Eqs. (1.4). A number of basic architectures

for energy transfer circuits have been reported in the literature, all of which fall into two main types: inductive circuits and charge pump circuits. Inductive energy transfer circuits are magnetic based circuits consisting of inductors that play an important role in transferring energy. A charge pump is a type of DC to DC converter that uses capacitors as storage component to create higher or lower voltages. The charge pump energy transfer circuit used for electrostatic energy harvesting uses a charge pump and a fly back circuit to transfer the harvested energy.

1.4 Wind induced vibration on trees

Wind flow energy is an important source for energy harvesting for wireless and portable devices. However, the use of flow energy is very limited because of the low efficiency and high cost of small scale turbine systems. Thus new technologies are needed to achieve high performance, low cost, small scale flow energy harvesting systems. Such a system should also be compact, easy to integrate and maintenance free. It is desirable to produce electrical energy at any wind velocity and maintain its performance at any scale. Potentially, is welcomed to Wind induced vibration on trees conversion which can provide these merits. However, wind induced vibration on trees conversion requires a cyclic excitation to produce continuous electric power. To use wind induced vibration on trees conversion for flow energy harvesting. ***The challenge lies in how to convert the wind flow or river current to a cyclic excitation***.

This section focuses on wind energy harvesting, which can be an active power source for WSNs, and for portable and wearable devices in environments. Wind is one of the most common types of mechanical energy sources It is free, clean, inexhaustible, environmentally-friendly and sustainable. The wind's kinetic energy can be captured by wind capturing devices, converted first into mechanical power and then into electrical power to supply various applications. The environmental impact of wind energy harvesters is relatively low. Unlike electricity extracted from fossil fuels, wind energy harvesters consume no fuel and emit no air pollution during operation. Wind energy can be harvested using three types of mechanical

energy converters: electromagnetic, electrostatic and piezoelectric.

Mechanical energy harvesting involves converting mechanical energy into electrical power. In effect, there are three main steps in harvesting mechanical energy: (a) capturing the energy from the environment and converting it into mechanical vibration power; (b) converting mechanical power into electrical power; (c) processing and storing electrical energy in a storage device or supplying it directly to a load [69]. The main energy flow for this system is illustrated in Fig. 1.12.

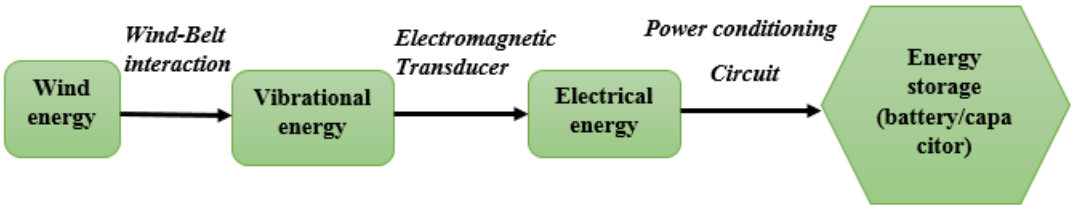

Figure 1.12: *Energy flow of the wind-driven transducer*

The power density, P, in the wind is related to the cube of the wind speed and this is expressed in the following equation [71]:

$$P = \frac{1}{2}\rho_{air}.U^3. \tag{1.15}$$

where ρ_{air} is the air density and U is the wind speed. This equation shows that the wind speed is the most important parameter for any wind energy harvesting technology and in choosing a location for a wind power plant.

Some researchers have investigated energy harvesting based on an elastic flutter model in order to improve energy harvesting efficiency at a low wind speed. Considering that environmental energy sources may manifest as dynamic vibrations, vibration-based energy harvesting technologies were also well explored to convert minute environmental vibrations [35], [41], [70]. Frayne and his group originated the idea to create a new type of wind generator based on the phenomenon of belt-flutter to harvest energy from air flows utilizing elastic structures. Fei Fei, John D. Maib, and Wen Jung Li 2011 [15] discussed a novel type of energy converter using the aerodynamic principle known as flutter. The objective was to harvest energy from low-speed wind flows in order to power electronic appli-

cations such as wireless sensor networks or outdoor lighting systems. Xue-Feng He and Jun Gao 2013 [71] used Impact to decrease the applicable wind speeds of flow-induced-vibration wind energy harvesting systems with MEMS harvesting elements. Wind is responsible of a chronical mechanical excitation of trees. It appears that little investigation into converting the mechanical energy of tree movement to electrical energy has been previously performed. Some work has been performed to harvest energy from trees using other methods, including the voltree bioenergy harvester [12], which the company claims *"converts living plant metabolic energy to useable electricity"*. This method of energy harvesting, using voltage differences within a living tree, has been described in publication [72]. A wind flow-induced-tree vibration energy harvesting system. When wind blows, the flow field is disturbed and the dynamic wind load on the flexible cantilever (tree) is enlarged. When wind speed increases to a specified critical value (the critical wind speed), the frequency of the dynamic wind load is close to the first natural frequency of the cantilever, which causes the cantilever to vibrate.

The aerodynamic force modelling the interaction between wind and isolated tree can be written in the following form the (Taylor, 1952; Blevins, 1977) [73], [74]

$$F = \frac{1}{2}\rho_{air}.A_E.C_D.\left|U\right|.U \tag{1.16}$$

Where A_E is the lateral area of structure and C_D the aerodynamic coefficient or air, U is the relative velocity of the structure. This force is responsible to tree vibration. The vibration (or oscillation) of flexibles trees are modelled in literature as a mode of Euler cantilever beam, that is subjected to small transversal displacement with negligible shearing. The tree beam is presumed to be isotropic, uniform whose bending moment depend linearly on the curvature.
It's well known in literature that a general equation governing the linear dynamic of transversal vibration of a beam is

$$\rho s\frac{\partial^2 y}{\partial t^2} + EI\frac{\partial^4 y}{\partial x^2} = 0 \tag{1.17}$$

When the excited aerodynamic force $F(t)$ act on the tree, the equation with nonlinear terns can permit us to foresee the behaviours of the structure. And

taking into account the dissipation and external excitation, we obtain

$$\rho s\frac{\partial^2 y}{\partial t^2}+\lambda\frac{\partial y}{\partial t}+EI\frac{\partial^4 y}{\partial x^2}+f_{NL}=F(t) \tag{1.18}$$

where λ is the damping coefficient and f_{NL} is a nonlinear force which can be a material nonlinearity or geometric one.

1.5 Problem statement of the thesis

As mentioned earlier, energy harvesting technologies from ambient low frequency vibration based on piezoelectric, electrostatic, and electromagnetic transduction mechanisms are used for running wireless sensors and low-powered electronics [75], [76]. ***This thesis presents a work to harvest the energy from trees vibrations, cantilever beams, flexible tubes and variation of parameters***. **Although the principle of electromagnetic induction has been used for many years to harvest mechanical energy, it has never been used in this specific application**.

Some research works offered a number of possible methods by which energy may be extracted from tree movement such as indicated in Ref. [12]. The ***first aim of this thesis is devoted to the conversion of trees and cantilever beams vibrations into electrical energy***. **The originality of this work part is the combination of experimental and theoretical analysis as well as the consideration of a tree as mechanical system**.

Achieving VEHs voltage level may be difficult when the ambient energy level is relatively low, the harvester size small, or the transduction scheme produces low voltage. Due to this, VEHs need to be rectified and boosted for many useful applications. However, there are major disadvantages in using the two-stage power converters to condition the outputs of the electromagnetic micro generators. First, for very low-voltage electromagnetic micro generators, rectification is not feasible by the use of conventional diodes. Second, if the diode bridge rectification is feasible, the forward voltage drops in the diodes will cause a large amount of losses and make the power conversion very inefficient. ***This thesis thus presents new circuit approaches of a passive AC/DC converter***.

In most cases, piezoelectric and electrostatic devices are more appropriate for small-scale harvesters while electromagnetic devices are better for large-scale. In spite of advances in energy harvesting using piezoelectric and electromagnetic approaches, the electrostatic approach retains a number of advantages: it is compact, sensitive to low mechanical energy, easier to integrate in small-scale systems, does not require smart materials, is simple to fabricate, its energy density can be modified geometrically, is low-cost and has a simple structure with less circuitry. However, it is also one of the least efficient with a low output power. So enhancing the output power density from electrostatic harvesters remains challenging [69]. Most reported variable capacitors for electrostatic energy harvesting depend on vibration to modify the area of the capacitor plates or the gap between them. Since research studies on this issue are very limited, a study considering the major variable parameters is not yet available. So, ***an analysis of the variation of the electrostatic energy harvester parameters on the generated electrical energy is considered in the second main point of this thesis***.

In case of biomedical implant, technological developments in the MEMS industry have led to miniaturization of many of the transducer systems. With further effort, the power consumption of these devices has been reduced to the order of μW to mW level. These developments have opened a new and interesting research area; supplying energy to these micro systems as an alternative to batteries, which have a finite life and are large in size. Considering implantable and embedded microsystems that should operate and survive on their initial energy supply, these ambient energy sources are attractive alternatives [77]. Various wirelessly powered devices have also been introduced; however, they require an interface for operation. Therefore, intra corporal energy harvesting devices may be an attractive alternative. In principle, intra corporal energy can be replenished, thereby providing continuous power to implanted microsystems. However, sources of intra corporeal energy for implanted microsystems are limited due to minimal movement or vibration. ***The last objective of this thesis is to extend the electrostatic configuration of electrostatic energy harvester to convert the expansion and contraction of an artery (due to pulsatile blood pressure changes) into electrical energy by electrostatic induction***.

1.6 Conclusion

In this chapter, we have provided some background on vibration energy harvesters. This has enabled us to state the problem of the thesis and its technology interests. The following chapter will be devoted to the mathematical formalisms, numerical, analog and experimental methods used to solve the problems of this thesis.

CHAPTER TWO

MATHEMATICAL FORMALISMS, NUMERICAL, ANALOG AND EXPERIMENTAL METHODS

2.1 Introduction

This chapter presents the ***Mathematical, numerical simulation, analog and experimental methods*** used to solve the problems of the thesis. It is divided in five sections: *Section II.2* presents the mathematical formalisms and the numerical methods used to solve the differential equations as well as the hardware and software used. In *section II.3*, materials and methods for experimental study are presented. *Section II.4* is devoted to the basic principles of VEHs techniques. The conclusion of the chapter appears in *section II.5*.

2.2 Mathematical formalisms and numerical methods

Generally, physics/engineering problems are modelled using rate-equations describing their dynamical behaviours. To solve the rate-equations describing the VEHs, one uses some mathematical formalisms and numerical methods which are presented here.

2.2.1 Mathematical formalism

Here, we present two analytical formalisms: the Galerkin procedure and the principle of harmonic balance method.

2.2.1.1) Galerkin procedure

Hayfeh and mook in 1979 [78] used a combination of the Galerkin procedure and the method of harmonic balance to determine the nonlinear frequencies of

beams. The basis governing equation for most of the studies of nonlinear beam vibration is a partial differential equations (PDEs) of the following form.

$$\rho S\frac{\partial^2 y}{\partial t^2}+\lambda\frac{\partial y}{\partial t}+EI\frac{\partial^4 y}{\partial x^4}+\frac{ES}{2l}\frac{\partial^2 y}{\partial x^2}\int_0^l\left(\frac{\partial y}{\partial x}\right)^2 dx=F(x,t) \tag{2.1}$$

The boundary conditions of a cantilever beam are

$$\begin{aligned} &y(0,t)=0;\quad \left.\frac{\partial y}{\partial x}\right|_{x=0,t}=0 \quad at \quad x=0\\ &\left.\frac{\partial^2 y}{\partial x^2}\right|_{x=l,t}=0;\quad \left.\frac{\partial^3 y}{\partial x^3}\right|_{x=l,t}=0 \quad at \quad x=l \end{aligned} \tag{2.2}$$

The Galerkin method suggets the solution as an expansion in terms of the linear free oscillation modes $\phi_m(x)$. That is,

$$y(x,t)=\sum_{m=1}^{N} q_n(t)\phi_m(x) \tag{2.3}$$

The free oscillation mode $\phi_m(x)$ are solutions of the following eigenvalue problem:

$$\phi_m^{IV}(x)-\omega_m\phi_m(x)=0, \tag{2.4}$$

where

$$\phi_m(x)=\phi_m^{''}(x)=0 \quad at \quad a \quad hinged \quad end, \tag{2.5}$$

and

$$\phi_m(x)=\phi_m^{'}(x)=0 \quad at \quad a \quad clamped \quad end. \tag{2.6}$$

The eigenvalues ω_m are the natural frequencies. The eigen function are orthogonal. To show this, we consider Eqs. (2-4) for two different values of m :

$$\phi_i^{IV}(x)-\omega_i^2\phi_i(x)=0 \quad and \quad \phi_j^{IV}(x)-\omega_j^2\phi_j(x)=0 \tag{2.7}$$

It follows that

$$\left(\omega_j^2-\omega_i^2\right)\int_0^l \phi_i(x)\phi_j(x)dx=\int_0^l\left(\phi_i\phi_j^{IV}-\phi_j\phi_i^{IV}\right)dx \tag{2.8}$$

Integrating by parts leads to:

$$\left(\omega_j^2 - \omega_i^2\right) \int_0^l \phi_i \phi_j dx = \left[\phi_i \phi_j^{'''} - \phi_i^{'} \phi_j^{''} + \phi_i^{''} \phi_j^{'} - \phi_i^{'''} \phi_j\right]_0^l \tag{2.9}$$

It follows from Eqs. (2-5) and Eqs. (2-6) that

$$\int_0^l \phi_i \phi_j dx = 0 \quad if \quad i \neq j \tag{2.10}$$

For convenience, we choose the amplitude of $\phi_m(x)$ such that

$$\int_0^l \phi_i \phi_j dx = \delta_{ij} = \begin{cases} 1 & if \quad i = j \\ 0 & if \quad i \neq j \end{cases} \tag{2.11}$$

Substituting (Eqs.(2-2)) into (Eqs.(2-1)), multiplying by $\phi_n(x)$ and integrating over the length, we obtain a set of ordinary differential equation (ODEs) Finally, the first modal solution of the eigenvalue problem is:

$$\phi_1(x) = -\frac{\sin(k_1) + \sinh(k_1)}{\cos(k_1) + \cosh(k_1)} \left[\cos(k_1 x) - \cosh(k_1 x)\right] + \left(\sin(k_1 x) + \sinh(k_1 x)\right) \tag{2.12}$$

For the numerical simulation, the value of k_1 corresponding to the first mode is given as $k_1 = 1.875$.

2.2.1.2) Principle of harmonic balance method

The harmonic balance method is a method of widest utility for obtaining a periodic solution of a nonlinear differential equation [79]. It can be used to determine an approximate periodic solution of vibrating energy harvester that can be excited by known steady-state periodic vibrations. Let us consider the following differential equation:

$$\ddot{x} + x = f(\dot{x}, x, t) \tag{2.13}$$

where the dot over x refers to the differentiation with respect to time t. The function f is such that $f(\dot{x}, x, t+T) = f(\dot{x}, x, t)$. The function contains explicitly the time t. The harmonic solution of equation to a first approximation is expressed under the form

$$x(t) = a\cos(\omega t) + b\sin(\omega t) = A\cos(\omega t + \phi) \tag{2.14}$$

where $A = \sqrt{a^2 + b^2}$ is the amplitude of oscillations, ω the pulsation of the sinusoidal excitation and $\phi = \arctan(b/a)$ the phase at the origin. Replacing Eqs. (2-14) into Eqs. (2-13) and equating separately the coefficient of sine and cosine terms which have the same harmonics, one obtains after neglecting harmonics order greater than one, a system of algebraic equations which are the amplitude equations. This method is the principle of harmonic balance, used to obtain small and intermediate amplitudes solutions. It will be used in the following chapter to determine the amplitude of vibration of the mechanical part of the transducer mechanism.

2.2.2 Numerical methods

Numerical method will be used in this thesis in order to get more accurate solution or to validate the analytical solution obtained from differential equations describing the physical system.

2.2.2.1) Principle of dichotomy method or the bisection method

The bisection method in mathematics is a root-finding method that repeatedly bisects an interval and then selects subinterval in which a root must lie for further processing. It is a very simple and robust method, but it is also relatively slow. Because of this, it is often used to obtain a rough approximation to a solution which is then used as a starting point for more rapidly converging methods. The method is also called the interval halving method, the binary search method, or the dichotomy method.
This method is combination of analytical and numerical methods because it is used to get numerically the solution of a polynomial equation with a high order obtained

analytically on an interval of solution [79]. Thus, for a polynomial equation which is monotonous with the following form:

$$f(x) = a_n x^n + a_{n-1} x^{n-1} + ... + a_1 x + a_0, \tag{2.15}$$

the equation allows a root x_0 in the interval $[a; \quad b], \quad if \quad f(a) \prec 0 \prec f(b)$. Let note the middle of interval $[a; b]$, if the product $f(a)f(c) \prec 0$, then a_0 is contained in $[a; c]$. This interval is divided several times with the previous method in order to get the approximate solution root of the function $f(x)$. This method will be used in the next chapter in order to have the roots of some polynomial equations obtained in the study amplitude equation of one of the vibration energy harvesting systems.

2.2.2.2) Fourth-order Runge-Kutta method for ODEs

When the steady-state of the excited vibrations is not linear any more, analytic solutions are not easy or just approximate, numerical integration is an interesting way to obtain information about the dynamic behaviours. Many different methods have been proposed and used in an attempt to solve accurately various types of nonlinear ODEs and PDEs. However, there are a handful of methods known and used universally (i.e., Runge-Kutta, Adams Bashforth-Moulton and backward differentiation formulae methods). From the Runge-Kutta family of algorithms come the most well-known and used methods for numerical integrations [80], [81]. Let us consider the first order differential equation

$$\frac{dy}{dx} = f(x, y) \tag{2.16}$$

with $y(x_0) = y_0$. This equation can also be under a vectorial form (y and f being vectors). The aim of the RK4 method is to find solutions $y(x + h)$ after each time step h of x, the next solution as a function of the previous one. This method stipulates that:

$$y(x + h) = y(x) + \frac{1}{6}(L_1 + 2L_2 + 2L_3 + L_4) \tag{2.17}$$

where

$$\begin{aligned} L_1 &= hf(x, y(x)); \\ L_2 &= hf(x + \tfrac{h}{2}, y(x) + \tfrac{L_1}{2}); \\ L_3 &= hf(x + \tfrac{h}{2}, y(x) + \tfrac{L_2}{2}); \\ L_4 &= hf(x + h, y(x) + L_3). \end{aligned} \tag{2.18}$$

This procedure needs in its iteration only the initial value $y(x_0) = y_0$, to calculate all the other values taken by the function y at other times separated by the time step t. Mechanical and engineering problems often simulate complex, nonlinear models of dynamic systems acted upon by noise. Ordinary RK method cannot solve such problems. Ordinary RK-method incurs significant errors when treating stochastic problems. In the following, we will present RK-algorithm for numerical integration of stochastic differential equations (SDEs): *Heun's* algorithm and *Kasdin's* algorithm for SDEs. They will be used to improve the accuracy of SDEs over the traditional approaches.

2.2.2.3) Heun's algorithmic method for SDEs

The next approach, *Heun's* method [82], [83] introduces a new idea for constructing an algorithm to solve the unpredictable vibrating phenomena.

$$\dot{y}(t) = f(t, y(t)) \quad over \quad [a, \quad b] \tag{2.19}$$

with $y(t_0) = y_0$

To obtain the solution point (t_1, y_1), we can use the fundamental theorem of calculus and integrate $\dot{y}(t) \quad over \quad [t_0, t_1]$ to get

$$\int_{t_0}^{t_1} f(t, y(t))dt = \int_{t_0}^{t_1} \dot{y}(t)dt = y(t_1) - y(t_0), \tag{2.20}$$

where the the integral of $\dot{y}(t)$ is the desired function $y(t)$. When Eqs. (2-20) are solved for $y(t_1)$, the result is

$$y(t_1) = y(t_0) + \int_{t_0}^{t_1} f(t, y(t))dt \tag{2.21}$$

Now a numerical integration method can be used to approximate the definite

integral in Eqs.(2-21). If the trapezoidal rule is used with the step size $h = t_1 - t_0$, then the result is

$$y(t_1) \approx y(t_0) + \frac{h}{2}(f(t_0, y(t_0)) + f(t_1, y(t_1))) \tag{2.22}$$

Notice that the formula on the right-hand side of Eqs. (2-22) involves the yet to be determined value $y(t_1)$. To proceed, we use an estimate for $y(t_1)$. *Euler's* solution will suffice for this purpose. After it is substituted into Eqs. (2-22), the resulting formula for finding (t_1, y_1) is called ***Heun's method***:

$$y_1 = y(t_0) + \frac{h}{2}(f(t_0, y_0) + f(t_1, y_0 + hf(t_0, y_0))) \tag{2.23}$$

The process is repeated and generates a sequence of points that approximates the solution curve $y = y(t)$. At each step, *Euler's* method is used as a prediction, and then the trapezoidal rule is used to make a correction to obtain the final value. The general step for Heun's method is

$$\begin{aligned} p_{k+1} &= y_k + hf(t_k, y_k), \qquad t_{k+1} = t_k + h \\ y_{k+1} &= y_k + \tfrac{h}{2}(f(t_k, y_k) + f(t_{k+1}, p_{k+1})). \end{aligned} \tag{2.24}$$

This method will be used to simulate the fluctuation component of the wind speed on the cantilever beam.

2.2.2.4) Kasdin method for SDEs

This subsection presents a Runge-Kutta (RK) algorithm for the numerical integration of stochastic differential equations. Consider for simulation the Ito SDEs

$$\dot{y}(t) = f(y, t) + g(y, t)\omega(t) \tag{2.25}$$

For this issue, *Kasdin* in 1995 [84] proposed the modified forms of Runge-Kutta algorithm because of its stability and small errors.
If $y(t)$is the solution of the differential equation

$$\dot{y}(t) = f(y, t) \tag{2.26}$$

Then $y(t)$ is approximated at time $t_{k+1} = t_k + h$, given its value at t_k by the following set of equations:

$$\begin{aligned} y_{k+1} &= y_k + \alpha_1 K_1 + \alpha_2 K_2 + ... + \alpha_4 K_4 \\ K_1 &= hf(t_k, y_k) \\ K_j &= hf\left(t_k + c_j h, y_k + \sum_{i=1}^{j-1} a_{ji} K_i\right) \end{aligned} \tag{2.27}$$

where h is the time step. These equations are an order$-n$ RK integrator. The coefficients $\alpha_i, \quad c_i, \quad and \quad a_{ji}$ are chosen in the deterministic case to ensure that simulates the solution with error of order. That is,

$$\dot{y}(t) = f(y, t) \tag{2.28}$$

The stochastic version of Eqs. (2-27), using Eqs. (2-25), is given by

$$\begin{aligned} y_{k+1} &= y_k + \alpha_1 K_1 + \alpha_2 K_2 + ... + \alpha_n K_n \\ K_1 &= hf(t_k, y_k) + hg(t_k, y_k) w_1 \\ K_j &= hf\left(t_k + c_j h, y_k + \sum_{i=1}^{j-1} a_{ji} K_i\right) + hg\left(t_k + c_j h, y_k + \sum_{i=1}^{j-1} a_{ji} K_i\right) w_j \end{aligned} \tag{2.29}$$

where w_j is a vector random process. The coefficients in Eqs. (2-27) are found by matching coefficients of a Taylor expansion of both Eqs. (2-26) and (2-27) to order h^n . It is well known that the resulting equations are underdetermined and that there are thus many order RK integrators.

The RK solution for y_k is given by the linear version of the stochastic equations (II-29):

$$\begin{aligned} y_{k+1} &= y_k + \alpha_1 K_1 + \alpha_2 K_2 + ... + \alpha_n K_n \\ K_1 &= hf_k(t_k, y_k) + hg_k(t_k, y_k) w_1 \\ K_j &= hf\left(t_k + c_j h\right)\left(y_k + \sum_{i=1}^{j-1} a_{ji} K_i\right) + hg\left(t_k + c_j h\right) w_j \end{aligned} \tag{2.30}$$

For a fourth-order solution, there are 14 unknowns and 13 equations. Table 2.1 lists one possible set of coefficients with the extra degree of freedom eliminated by requiring that $a_{41} = 0$.

Table 2.1: Runge-Kutta coefficients for fourth-order time-invariant solutions (method A).

Coefficients	Fourth order	Coefficients	Fourth order
α_1	0.47012396888046	a_{41}	0
α_2	0.36597075368373	a_{42}	0.48257353309214
α_3	0.08906615686702	a_{43}	0.26171080165848
α_4	0.07483912056879	q_1	2.12709852335625
a_{21}	2.71644396264860	q_2	2.73245878238737
a_{31}	−6.95653259006152	q_3	11.22760917474960
a_{32}	0.78313689457981	q_4	13.36199560336697

This other method will be used to simulate the blood pulsation through the artery.

2.2.3 Hardware and software

During the course of this work, we used a Laptop computer running Window 7 operating system and four major softwares: Fortran, Matlab, PSpice and Maple.

2.3 Basic Principles of energy harvester

In this section, we introduce the basic principles of EHs that will be used to design and build the VEHs in this thesis. A VEHS must be able to perform all the basic operations which describe the differential equation characterizing its dynamics such as: the basic principle of electromagnetism and the basic principle of electrostatics.

2.3.1 Basic Principles of electromagnetic energy harvester

The technical foundation of energy harvesting through electromagnetic conversion has been well established. According to *Faraday's* law of induction, when a wire is moved relative to a magnetic field, or vice versa, an electromotive force is created. If the wire is connected through an electrical load, current will flow, and thus electrical energy is generated, as schematically shown in Fig. 2.1.

In a simple case of a coil moving through a perpendicular magnetic field of a

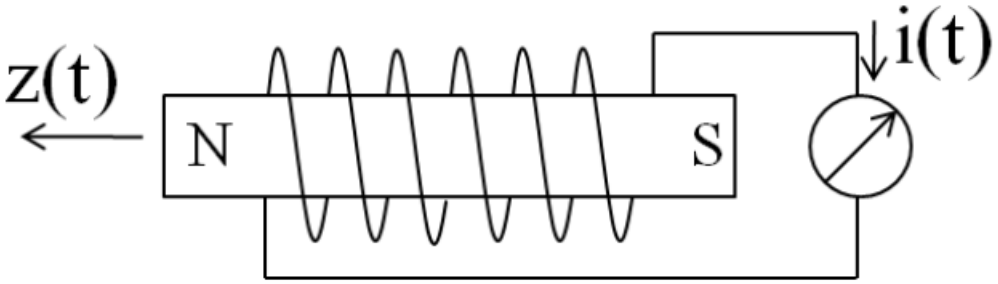

Figure 2.1: *Base Principe of Electromagnetic induction.*

constant strength, the maximum open-circuit induced voltage across the coil is

$$V(in \quad volt) = N\frac{d\phi}{dt} \tag{2.31}$$

where N is the number of coils turns. ϕ is the magnetic flux in Webers. This expression was determined by *Faraday* empirically. The dynamic model of an electromagnetic shaker in the case of a permanent magnet moving through a coil can be expressed as

$$V(in \quad volt) = Bl\dot{z} \tag{2.32}$$

where $\dot{z}$ is the velocity of the permanent magnet,B magnetic field, and l the total length of the coil. The same model also presents an expression of *Laplace* force

$$f = Bli, \tag{2.33}$$

where i is the induced current.

2.3.2 Basic principles of electrostatic energy harvester

Electrostatic transducers are largely used in MEMS transducers due to advantages such as sensitivity, fast response, precision, relatively easy fabrication, or integration with complementary metal oxide semiconductor (CMOS) technology. Two main principles of electrostatic transduction motions are presented in Fig. 2.2. These two types of motions are the main technological applications in planar MEMS. By charging two bodies with equal and opposite charges (+q and -q),

capacitive-type attraction forces between the two bodies can be generated potentially. Charging can be done by means of an external voltage.

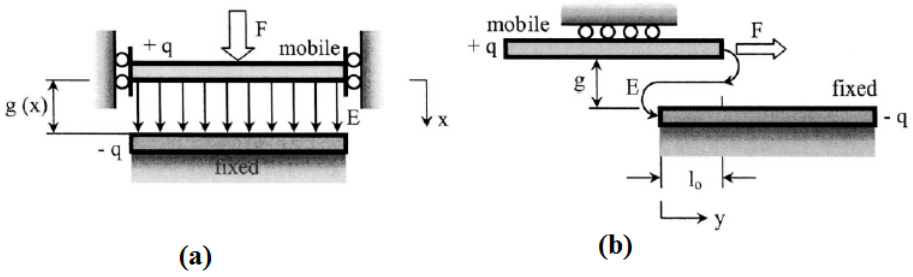

Figure 2.2: *Principle of electrostatic transduction motions: (a) transversal configuration; (b) longitudinal configuration.*

(a). In-plane transverse (parallel-plate) transduction

The capacitance of a transverse-type transducer is:

$$C(x) = \frac{\varepsilon A}{g_x} = \frac{\varepsilon . l_y . l_z}{(g_0 - x)} \tag{2.34}$$

where ε is the electric permittivity, l_y is the plate dimension (plate width) perpendicular to the plane, l_z is the overlap out-of-the-plane dimension, g_0 is the initial gap in the x-direction, and is the displacement produced by the electrostatic forces. The initial-condition capacitance can be found by taking $x = 0$ in Eqs. (2-34), namely:

$$C(0) = \frac{\varepsilon A}{g_0} = \frac{\varepsilon . l_y . l_z}{g_0} \tag{2.35}$$

As Eqs. (2-34) and Eqs. (2-35) suggest, the variation in capacitance is only produced through changing of the gap between the two plates because the overlapped area $A = l_y . l_z$ is constant for a transverse electrostatic transducer. When a voltage V is supplied externally, the electrostatic energy is:

$$U_e = \frac{1}{2} C(x) . V^2 \tag{2.36}$$

The corresponding attraction force between the fixed and the mobile plates is defined as the partial derivative of the electrostatic energy in terms of displacement,

and is calculated by using Eqs. (2-35) and (2-36) as:

$$F = \frac{\partial U_e}{\partial x} = \frac{\varepsilon.l_y.l_z.V^2}{2\left(g_0 - x\right)^2} \tag{2.37}$$

The initial force (when the two plates are apart) is:

$$F_0 = \frac{\varepsilon.l_y.l_z.V^2}{2g_0^2} \tag{2.38}$$

(b). In-Plane longitudinal (comb-finger) transduction

The other possibility of in-plane actuation is illustrated in Fig. 2.2(b), which shows two adjacent plate digits, one fixed and the other one mobile, the latter one moving parallel to the former one. By charging the two plates with equal and opposite charges, +q and -q, the electric field will generate attractive forces between the two plates, with the net result that the mobile plate will move to the right in the figure.

The overlap area will vary this time, since the engaging distance over the direction of motion changes. The capacitance is:

$$C(y) = \frac{\varepsilon\left(l_0 + y\right).l_z}{g} \tag{2.39}$$

where l_z is the plate dimension (plate width) perpendicular to the plane of the drawing; it is the length along which they overlap.

The energy stored by the capacitor is given by

$$U_e = \frac{1}{2}C(y).V^2 = \frac{q^2.g}{\varepsilon\left(l_0 + y\right).l_z} \tag{2.40}$$

It clearly shows that the energy varies inversely with the region of overlap. We may use the energy stored by the capacitor (Eqs. (2-40)) to determine the constitutive relation of the 2-part capacitance.

We identify $\frac{\partial U_e}{\partial q}$ as the voltage, which is given by

$$V = e = \frac{\partial U_e}{\partial q} = \frac{q.g}{\varepsilon\left(l_0 + y\right).l_z} \tag{2.41}$$

We identify $\frac{\partial U_e}{\partial y}$ as the force that generates the motion to the right. It can be calculated by means of the definition given in Eqs. (2-37) and its expression is:

$$F = \frac{\partial U_e}{\partial y} = -\frac{q^2.g}{2\varepsilon \left(l_0 + y\right)^2 .l_z} \tag{2.42}$$

Note that since y is varying in time, these constitutive relations are nonlinear. Note also that the lateral force decreases as the overlap between the plates increases. This negative sign in (Eqs. (2-40)) indicates that the lateral force is a restoring force such as we would find in a spring.

2.4 Materials and methods for experimental study

In this section, a list of materials used to conduct experiments is presented. The procedure of data collection and the method of analysing data are also presented. Some electronic components, and the voltage multiplier circuit used during the experiment are elaborated.

2.4.1 Materials used

The electromagnetic transducer proposed, as they are based on electromagnetic induction force, use permanent magnet acting on a movable coil house. For experiments, the electromagnetic transducer is built using recycled components and some materials for collecting data. A Rotating fan was used to provide the wind flow. The experimental procedure consists of the measurement of the vibration amplitude of flexible tree beam, or the rotation of a pendulum arm. Two main experimental setups are use in this thesis. The first consists of the translation vibration of the flexible beam with the electromagnetic transducer at its tip. The second is the pendulum electromagnetic transducer see Fig.2.3

For this achievement, the materials used are presented as follows.

- A rotating fan : to provide air flow in the lab;
- A flexible beam : to react to the external wind excitation;
- A permanent magnet and coil: to make a transducer;

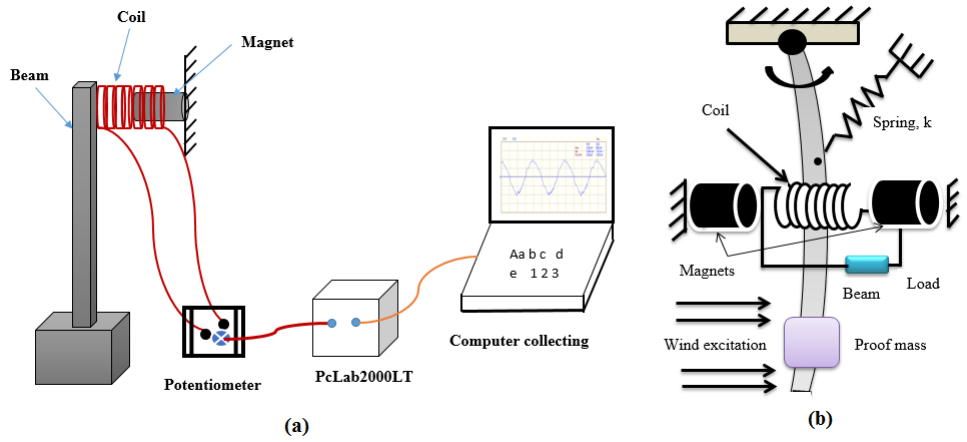

Figure 2.3: *Schematic of the both experimental procedure: (a) beam translation, (b) rotate pendulum.*

- An accelerometer (Go!Motion): to collect the position, velocity and acceleration data of moving objects;
- A PCLab 2000LT oscilloscope: to visualize the induced voltage;
- A computer: to collect experimental data;
- Connector cables and potentiometer: used as load charge.

2.4.2 Data collection and analysis

The acceleration, velocity and position of the beam motion are measured by using a Vernier Go! Motion accelerometer (see Fig. 2.4(a)). It is a universal serial bus (USB) motion detector that includes free Logger-Lite software. Go!Motion is used to collect the acceleration, velocity and position data of moving objects. It is connected directly to a computer USB port making it fast and easy to set up experiments and start collecting a wide range of real-time motion data. It can track objects between the distance ranges between 15 cm and 6 m.

The variation of the induced output voltage measured and visualized on the PcLab2000LT oscilloscope (see Fig. 2.4(b)). For the PCSGU250 unit, a complete USB-powered lab-in-a-box. Feature-packed PcLab2000LT software for two channel oscilloscope, spectrum analyser, recorder of the induced voltage coming from the transducer mechanism.

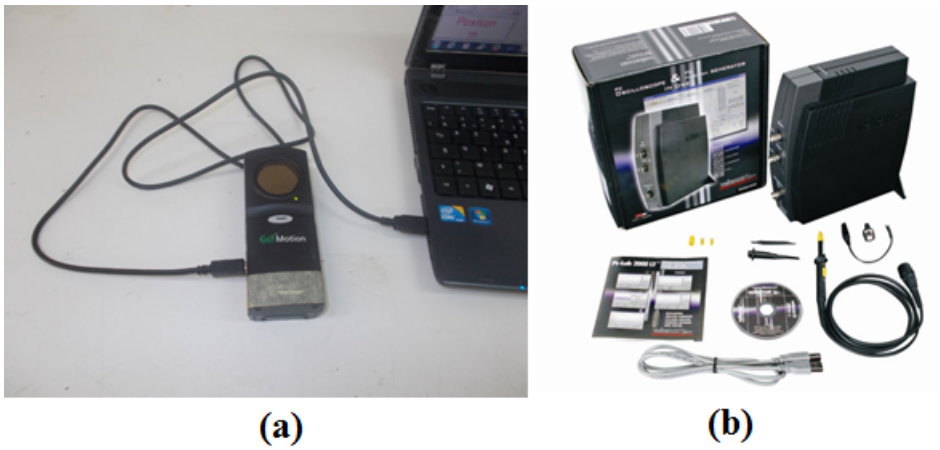

(a) (b)

Figure 2.4: *A view of a Vernier Go!Motion in (a), and the PcLab2000LT software in (b)*

2.4.3 Electronic components

We use electronic components such as resistors, capacitors, Schottky diode and light emitting diodes (LED), voltage multiplier. Indeed, combinations of resistors, capacitors, Schottky diode, and voltage multiplier lead to rectifier and boost the low harvester AC voltage.

2.4.4 Voltage multiplier circuit

Voltage multipliers are simple circuits made from diodes and capacitors that can potentially produce an output voltage many times greater than of the applied input voltage and by cascading together individual half or full stage multipliers in series to apply the desired DC voltage to a given load without the need for a step-up transformer. They convert AC-to-DC voltages for use in many electrical and electronic circuit applications such as in microwave ovens, strong electric field coils for cathode-ray tubes, electrostatic and high voltage test equipment, etc, where it is necessary to have a very high DC voltage generated from a relatively low AC supply.

Voltage multiplier circuits are classified as voltage Doubler's, Tripler's, or Quadrupler's, etc, depending on the ratio of the output voltage to the input voltage. In theory any desired amount of voltage multiplication can be obtained and a cascade of "N" doublers, would produce an output voltage of 2N.Vp volts.

For example a voltage doubler is a voltage multiplier circuit which has a voltage

multiplication factor of two. The circuit consists of only two diodes, two capacitors and an oscillating AC input voltage (a PWM waveform could also be used). This simple diode-capacitor pump circuit gives a DC output voltage equal to the peak-to-peak value of the sinusoidal input. In other words, double the peak voltage value because the diodes and the capacitors work together to effectively double the voltage.

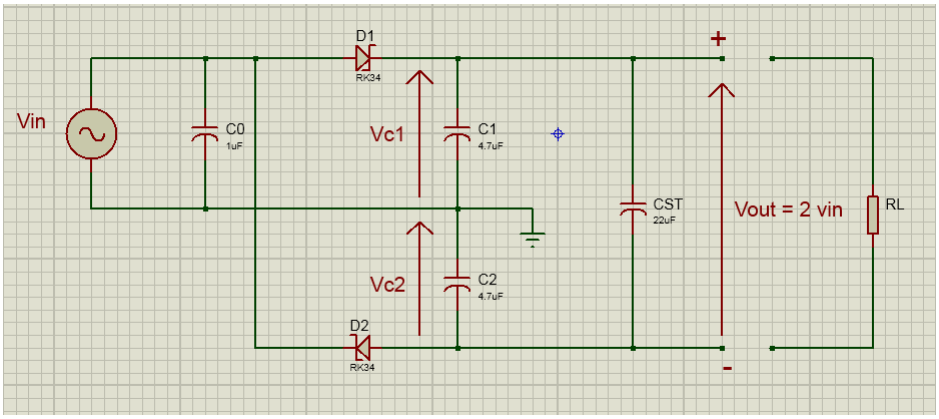

Figure 2.5: *Schematic of DC Voltage doubler circuit.*

So how does it work? The circuit shows a half wave voltage doubler. During the negative half cycle of the sinusoidal input waveform, diode D1 is forward biased and conducts charging up the pump capacitor, C1 to the peak value of the input voltage, (Vp). Because there is no path for capacitor C1 to discharge into, it remains fully charged and acts as a storage device in series with the voltage supply. At the same time, diode D2 conducts via D1 charging up capacitor, C2. During the positive half cycle, diode D1 is reverse biased blocking the discharge of C1 while diode D2 is forward biased charging up capacitor C2. But because there is a voltage across capacitor C1 already equal to the peak input voltage, capacitor C2 charges to twice the peak voltage value of the input signal.

As capacitor C2 only charges up during one half cycle of the input waveform, the resulting output voltage discharged into the load has a ripple frequency equal to the supply frequency, hence the name half wave voltage Doubler. The disadvantage of this is that it can be difficult to smooth out this large ripple frequency in much the same way as for a half wave rectifier circuit. Also, capacitor C2

must have a DC voltage rating at least twice the value of the peak input voltage. The advantage of "Voltage multiplier Circuits" is that it allows higher voltages to be created from a low voltage power source without a need for an expensive high voltage transformer as the voltage Doubler circuit makes it possible to use a transformer with a lower step up ratio than would be need if an ordinary full wave supply were used. However, while voltage multipliers can boost the voltage, they can only supply low currents to a high-resistance (+1000 Ω) load because the generated output voltage quickly drops-off as load current increases.
However, the diodes and capacitors used in all multiplication circuits need to have a minimum reverse breakdown voltage rating of at least twice the peak voltage across them as multi-stage voltage multiplication circuits can produce very high voltages, so take care. Also, voltage multipliers usually supply low currents to a high-resistance loads as the output voltage quickly drops away as the load current increases. In other words, V (positive peak) + V(negative peak) as on the negative half-cycle, diode D1 charges C1 to Vp and on the positive half-cycle D2 adds the AC peak voltage to Vp on C1 and transfers it all to C2. The voltage across capacitor, C2 discharges through the load ready for the next half cycle. Then the voltage across capacitor, C2 can be calculated as: Vout = 2Vp, (minus of course the voltage drops across the diodes used) where Vp is the peak value of the input voltage. Note that this double output voltage is not instantaneous but increases slowly on each input cycle, eventually settling to 2Vp.

2.5 Conclusion

This chapter has dealt which the presentation of analytical, numerical and experimental methods used to study the dynamical behaviours of the vibrational energy harvester transducers considered in this thesis.
These methods will be used in chapter 3 and chapter 4 to:
− model and describe of the propose vibration energy harvesting systems;
− obtain the analytical solutions of the vibration amplitude of the system, describing the mathematical models of our devices;
− discuss general design considerations, including all the factors affecting the de-

sign of the harvester and the design procedures that can be followed to design a suitable vibration energy harvester for a specific application;

− report on the simulations and experiments conducted for this study, before discussing the results to verify validity of the proposed harvester.

Chapter Three

Results on magnetic conversion of tree/beam vibration into electrical energy

3.1 Introduction

This chapter deals with the presentation of results and discussion and their technological application in real life. Therefore the chapter is organized as follows. The second section is devoted to energy harvesters using vibration of trees. In section three, we introduce and study the dynamics of energy harvesters using electromechanical pendulum. The fourth section focuses on amplification circuit design. The last section concludes the chapter.

3.2 Energy harvester using translation vibration of tree

In this section, we analysed the harvesting of energy from wind-induced beam/tree vibration using a magnetic transduction mechanism. The output voltage and power response of the system are analysed in terms of load resistance in a prototype built in the laboratory assuming an air flow with velocities varying periodically from 1.95 m/s to 4.71 m/s. A mathematical model is developed accompanied by numerical simulation and a fairly good agreement is obtained between the experimental results and theoretical ones. A test on a real tree model is conducted, the goal being to find the amount of energy that can be obtained using an example of tree vibration.

3.2.1 Experimental setup

The physical model is constituted of a clamped-free beam made of wood with a transducer at its free end. The details on the transduction mechanism are ex-

plained in Section 2.2. The beam is subjected to the periodic action of a transversal wind flow with velocity varying from 1.95 m/s to 4.71 m/s. The air flow is generated by a rotating small fan acting as a wind tunnel. Fig. 3.1 presents the prototype with all its components and measurement apparatus.

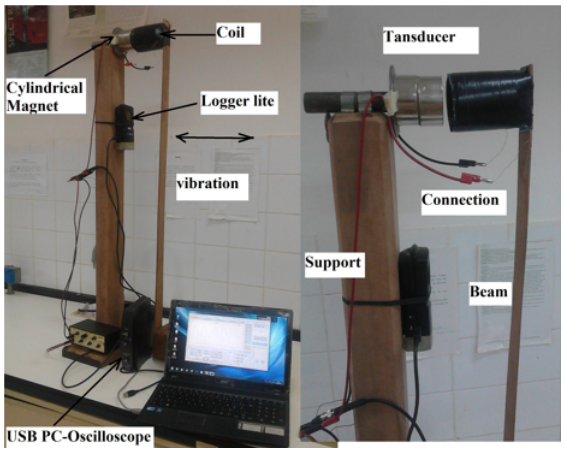

Figure 3.1: *Experimental setup of translation beam.*

One considers a rectangular cantilever beam whose thickness, width and height are respectively $e = 5.10^{-3}\ m$, $lar = 4.5 \times 10^{-2}\ m$ and $l_p = 1.1\ m$. The wood used is a Cameroonian species locally known as Moabi and scientifically known as *Baillonella toxisperma*. The density, calculated from the measurement of the mass of the beam ($m_p = 200\ g$) is $\rho = \frac{m_p}{l_p.lar.e} = 808.8\ kg/m^3$. The mean Young's modulus of the Moabi wood is E=9.35 GPa [85]. The beam cross section is $S = e \times lar = 225.10^{-6}\ m^2$. Using the logarithmic decrement method (measuring the beam free vibration amplitude for several damped oscillations), the viscous damping coefficient has been found to be approximately equal to $\varsigma = 0.03\ kg/s$. The magnetic field induction is $B = 1\ T$, with a coil mass of $m_b = 300\ g$. The coil is made of several turns of copper wire of radius, resistivity and cross section respectively equal to $r_{cu} = 175.10^{-6}\ m$, $\rho_{cu} = 1.8{\times}10^{-8}\ \Omega.m$ and $S_{cu} = \pi \times r_{cu}^2 = 9.616 \times 10^{-8}\ m^2$. The height, radius and section of the coil are respectively $h_b = 7.5{\times}10^{-2}\ m$, $r_b = 3.5{\times}10^{-2}\ m$ and $S_b = \pi{\times}r_b^2 = 3.846{\times}10^{-3}\ m^2$. Knowing the wire diameter $D_{cu} = 350 \times 10^{-6}\ m$, the number of wire turns $N = 330$ and the total length of the wire is $l = 2\pi r_b N = 72.50\ m$. The resistance and the self-inductance of the coil are given by $R_{cu} = \frac{\rho_{cu}.l}{S_{cu}} = 18.5\ \Omega$ and

$L_H = \mu_0 N^2 S_b / h_b = 7.015\ mH$, where $\mu_0 = 4\pi \times 10^{-7}$ is the air permeability. The air density is $\rho_a = 1.25\ kg/m^3$

Tables 3.1 and 3.2 recapitulate the values of the parameters of the mechanical and electrical parts as well as the value of the intensity of the magnetic field.

The calculation of the beam second moment and quadratic moment has used the following expressions: $I_{ZZ} = \frac{1}{3}e^3.lar$ and $I = \frac{1}{12}e^3.lar$.

Table 3.1: Electromagnetic system: characteristics and model parameters.

Characteristic	**Value**	**Parameter**	**Value**
Coil resistivity ρ_{cu}	$1.8\ \times 10^{-8}\ \Omega.m$	Self-inductance L_H	$7.015\ mH$
Coil resistance R_{cu}	$18.5\ \Omega$	Air permeability μ_0	$4\pi \times 10^{-7}$
Wire radius r_{cu}	$175 \times 10^{-6}\ m$	Magnetic field B	$1.0\ T$
Coil height h_b	$7.5 \times 10^{-2} m$	wire length l	$72.5\ m$
Wire section s_{cu}	$9.616 \times 10^{-8}\ m^2$	Wire turns N	330
Coil mass m_b	$300\ g$	Coil diameter D_b	$0.07\ m$

Table 3.2: Parameters of the clamped-free beam.

Characteristic	**Value**	**Parameter**	**Value**
Young's modulus E	$9.35\ GPa$	Beam cross section S	$225 \times 10^{-6}\ m^2$
Beam mass m_b	$200\ g$	Beam density ρ	$808.8\ kg/m^3$
Beam height l_p	$1.1\ m$	Air density ρ_a	$1.205\ kg/m^3$
Beam thickness e	$5.0 \times 10^{-3} m$	Exposed area A_E	$0.0495\ m^2$
Beam width lar	$4.5 \times 10^{-4} m$	Flow mean speed U_0	$33.3\ m/s$
Second moment I_{ZZ}	$1.012\ \times 10^{-10}\ m^4$	Flow Amplitude u_1	$1.3\ m/s$
Quadratic moment I	$18.75\ \times 10^{-10}\ m^4$	—	—

3.2.2 Description of the system

The transducer consists of a cylindrical support on which the electrical wire is enrolled. One end of the cylindrical support is rigidly attached to the flexible beam, and the other end can move, entering in the magnetic field of a cylindrical magnet. The magnet is attached to an artificial fixed structure. The coil motion into the magnetic field creates the variation of the magnetic flux. Thus an induced electromotive voltage $e(t)$ is created across the coil. Its mathematical expression

is given by the *Lenz-Faraday's* law

$$e(t) = -\vec{l}(\vec{B}\Lambda\vec{v}) \tag{3.1}$$

where $v = \frac{\partial y}{\partial t}$ is the coil/beam velocity, l is the length of the electric wire, and B the intensity of the magnetic field.

The output of the electrical part of the circuit is connected to a PC oscilloscope using probes. The portable oscilloscope is directly linked to a portable computer that can display the time history of the voltage at the open circuit and across a variable load resistance.

3.2.3 Experimental results and discussions

The accelerometer was used to measure the cantilever beam acceleration, velocity and position. The velocity was determined directly by using the integration function of the accelerometer which has options for acceleration, velocity and position (the integration circuit transforming the acceleration to velocity and velocity to position is directly incorporated in this accelerometer). A portable oscilloscope was used to collect data file and to visualize the time history of the output voltage of the electrical part. Recorded data were plotted using Matlab software. Fig. 3.2 presents some representatives of the time history of the beam displacement and velocity. From this Fig. 3.2, the periodicity of the time variation of the velocity is not clearly visible because of the sampling precision of the accelerometer and subsequently the error generated by the integration process. However, as it will be found in Fig. 3.3, a sort of almost periodic behaviour exists.

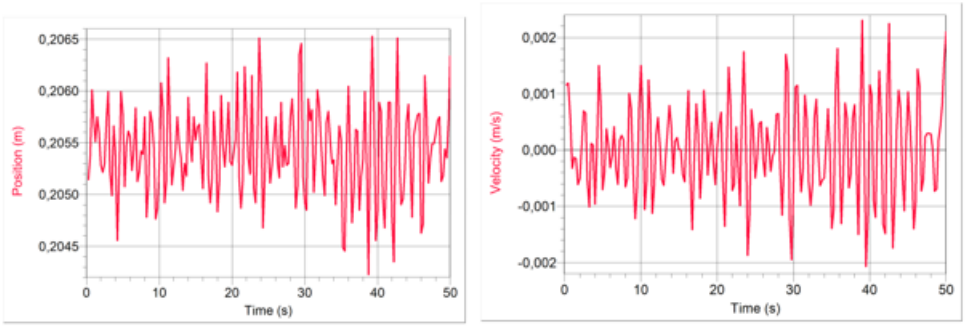

Figure 3.2: *Displacement and velocity of the beam as function of a time.*

The voltage time history across the electrical circuit is shown in Fig. 3.3 (case of open circuit without connecting the load resistance). It shows a sort of almost periodic function and from the data automatically included in the graph of Fig. 3.3, one notices that the voltage response across the electrical part varies from $-0.353\ V$ to $0.388\ V$. This gives a mean amplitude of about $0.3705\ V$ and mean frequency of about $1.55\ Hz$.

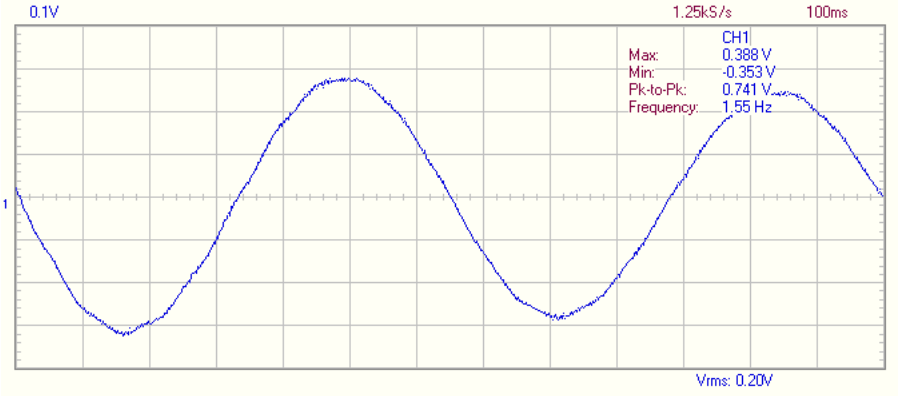

Figure 3.3: *Variation of the induced output voltage (Visualization on the PcLab2000LT).*

The scales along the axis of Fig. 3.3 are respectively 100 ms/div on the horizontal axis and 0.1 V/div on the vertical axis.
When the harvester is connected to a variable load resistance, the output voltage, current, and power as function of the load resistance are shown in Fig. 3.4(a), 3.4(b), 3.4(c) respectively. Let us mention that the only data coming directly from the experiment is the maximal value or amplitude of the voltage (Fig. 3.4(a)). The current amplitude is obtained as the ratio between the voltage and the resistive load value and the power is obtained from the formula $P = R_{load} i^2(t)$ where $i = \frac{V_{out}}{R_{int}+R_{load}}$; $P = \frac{R_{load}}{(R_{int}+R_{load})^2} V_{out}^2$
where R_{int} is the internal coil resistance corresponding to R_{cu}, R_{load} is a variable resistive load. One notices that the current decreases as the load increases while the voltage and power increase and attain their maximum for specific values of the resistance.

As the load resistance increases, the output voltage increases and attains a saturation Fig. 3.4(a), while the current through the circuit decreases Fig. 3.4(b).

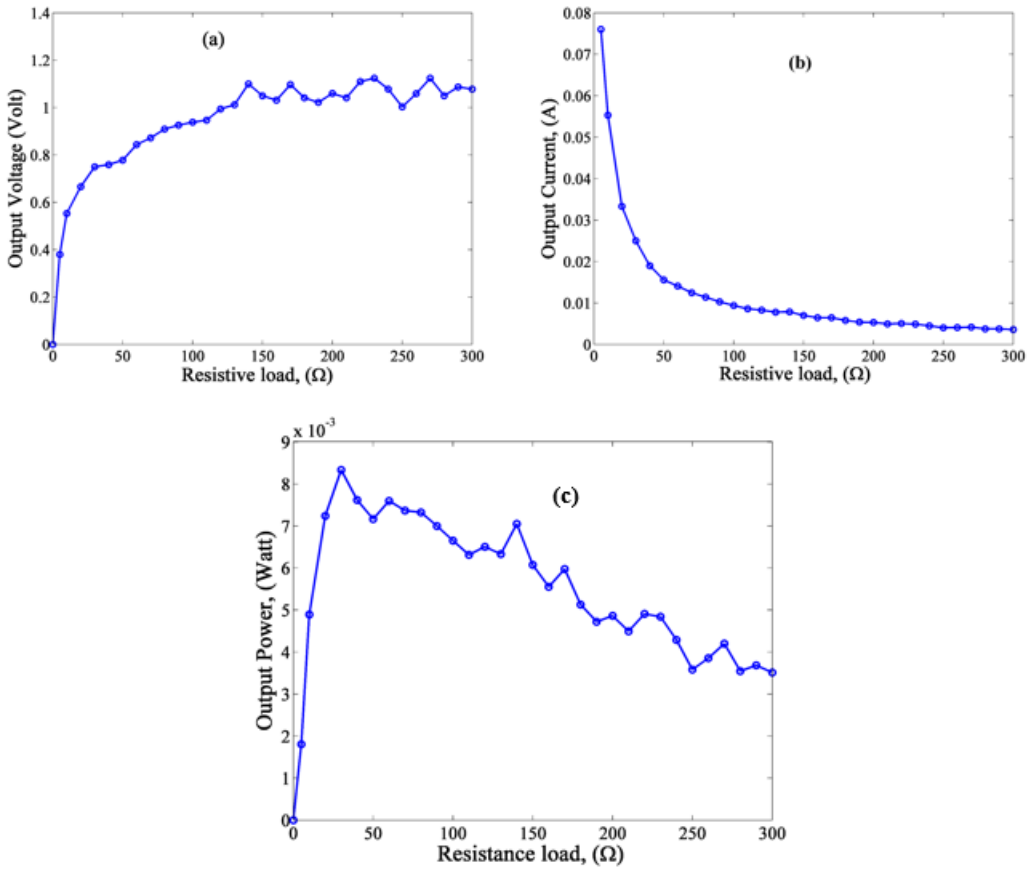

Figure 3.4: *(a) voltage output, (b) Current, and (c) output power as a function of load resistance.*

For Fig. 3.4(c), as the load resistance increases, the harvested power increases until it reaches a maximum value at $R_{load} = 30\ \Omega$. A further increase of the load resistance results in a decrease in the harvesting power which approaches zero. The maximum power is delivered to the electrical load when its optimal resistance (R_{load}) is equal to the sum of coil internal resistance (20 Ω measured value) and the electrical analogue of the mechanical damping coefficient. It is seen that the device can produce power of the order of 8.5 mW.

3.2.4 Mathematical and numerical results

In this part, the theory has been considered for comparison with the experimental studies. The equations of the model (Fig. 3.1) are given by

$$\begin{aligned}
&\left(\tfrac{m_b}{l_p}f(Z)+\rho S\right)Y_{tt}+\varsigma Y_t+EIY_{ZZZZ}+\left(\tfrac{m_b}{l_p}f(Z)+\rho S\right)gY_Z\\
&+\tfrac{ES}{2l_p}Y_{ZZ}\int_0^{l_p}Y_Z^2dZ=-BI_c(l/l_0)f(Z)+F(t)\\
&L_H\dot{I}_C+R_{int}I_C=u_e(t)+BlY_tf(Z)
\end{aligned}\tag{3.2}$$

with the following meanings:
$Y_t\equiv\frac{\partial y}{\partial t}, Y_z\equiv\frac{\partial y}{\partial z}, Y_{tt}\equiv\frac{\partial^2 y}{\partial t^2}, Y_{zz}\equiv\frac{\partial^2 y}{\partial z^2}, Y_{zzzz}\equiv\frac{\partial^4 y}{\partial z^4}$
where $Y(Z,t)$ is the transversal beam deflection, function of time t and coordinate Z along the beam length, E is the Young modulus, S is the beam cross section, ρ is the beam mass density, l_p is the beam length, ς is the damping coefficient, L_H is the self-inductance of the coil, R_{coil} is the coil internal resistance, I_c is the current in the electrical circuit, B is the magnetic intensity, l is the total length of the winding wire and l_0 is a reference length. l_0 is introduced here to indicate that the Laplace force is taken as a force per length. The first equation in (1) can be obtained from classical books [78] [86].
$F(t)$ is the aerodynamic force per length due to wind pressure on the beam (it is defined here after).

$$f(Z)=H(Z)+H(Z-Z_1)-H(Z-L)\tag{3.3}$$

is a spatial function used to specify that the transducer patch is localized in the region $Z_1\leq Z\leq L$, where $H(.)$ denotes the Heaviside step function. $u_e(t)$ is the voltage across the coil (load voltage if any). If the coil is not connected to an external circuit, then $I_c=0$, and $u_e(t)=BlY_tf(Z)$ which is the induced voltage. If the coil is connected to a variable resistance R_{load}, then $I_c\neq 0$, and $u_e(t)=R_{load}.I_c$.
For the prototype beam in Fig. 3.1, the displacement, flexural moment, and twist moment vanish at the beam ends, and the associated clamped-free boundary conditions are given as $Y(0,t)=0,\quad Y_z(0,t)=0,\quad Y_{zz}(L,t)=0,\quad Y_{zzz}(L,t)=0$

The aerodynamic loading force on the cantilever per unit length provoking vibration is given by:

$$F(t) = \frac{1}{2}\rho_a \tilde{A}_E C_D (U - Y_t)\,|U - Y_t| \tag{3.4}$$

with $\tilde{A}_E = A_E/l_p$ where ρ_a is the air mass density. A_E is the area per unit height of the beam/tree exposed to the wind at height Z above the ground. C_D is the drag coefficient, U is the actual wind velocity which can be decomposed as $U(t) = U_0 + U_f(t)$, where U_0 is the constant (average) part, representing the steady component, and $U_f(t)$ is the fluctuation component. $|U(t) - Y_t|$ is the relative velocity of the wind to the tree

We define $\in = \begin{cases} 1, & if \quad U(t) \succ \mathrm{Y_t} \\ -1, & if \quad U(t) \prec Y_t \end{cases}$

and $\alpha' = \frac{1}{2}\rho_a \tilde{A}_E C_D$. We assume in this study that $U(t) \succ Y_t$, and $U_0 >> U_f(t)$. Eqs.(3.2) takes the following form

$$\begin{aligned} &\left(\tfrac{m_b}{l_p} f(Z) + \rho S\right) Y_{tt} + \varsigma Y_t + EIY_{ZZZZ} + \left(\tfrac{m_b}{l_p} f(Z) + \rho S\right) g Y_Z \\ &+ \tfrac{ES}{2l_p} Y_{ZZ} \int_0^{l_p} Y_Z^2 dZ = -BI_c(l/l_0) f(Z) + \alpha' \in (U(t) - Y_t)^2 \\ &L_H \dot{I}_C + R_{int} I_C = u_e(t) + Bl Y_t f(Z) \end{aligned} \tag{3.5}$$

Let us consider the following rescaling variables: $y = \frac{Y}{l_0}, z = \frac{Z}{l_0}, \quad i = \frac{I_c}{I_0}, \quad \tau = \omega_0 t$, where $l_0, \quad I_0, \quad \omega_0$ are respectively the length reference, the current reference, and the frequency reference. The dimensionless form of Eqs. (3-5) is then obtained and given by

$$\begin{aligned} &(1 + Mf(z))\, y_{\tau\tau} + \lambda y_\tau + y_{zzzz} + (1 + Mf(z))\, \delta y_z \\ &+ N_1 y_{zz} 0 \int_0^{l_p/l_0} y_z^2 dz = -\alpha B i f(z) + \gamma(u - \varepsilon y_\tau)^2 \\ &i_\tau + \mu(R_{int} + R_{load}) i = \beta B y_\tau f(z) \end{aligned} \tag{3.6}$$

where the index stands for the derivative and with the following dimensionless parameters:

$$\begin{gathered} M = \tfrac{m_b}{\rho S l_p}, \quad \lambda = \tfrac{\varsigma}{\rho S \omega_0}, \quad \omega_0 = \tfrac{1}{l_0^2}\sqrt{\tfrac{EI}{\rho S}}, \\ \delta = \tfrac{g}{l_0 \omega_0^2}, \quad N_1 = \tfrac{E}{2 l_0 \omega_0^2 \rho l_p} = \tfrac{S.l_0^3}{2 l_p I}, \quad \alpha = \tfrac{l I_0}{\rho S l_0 \omega_0^2}, \end{gathered}$$

$$\gamma = \frac{\alpha' \in}{\rho S l_0 \omega_0^2}, \quad \mu = \frac{1}{\omega_0 L_H}, \quad \beta = \frac{l.l_0}{L_H I_0}, \quad \varepsilon = \omega_0 l_0.$$

In the remaining of the work, we assume that $l_0 = l_p$.

Instead of the partial differential Eqs. (3-6), a simpler and mathematically tractable model is preferred. Indeed, it has been shown that the solution of Eqs. (3-6) can be obtained through the Galerkin decomposition method as in [78].

$$y(z,\tau) = \sum_{n=1}^{N} q_n(\tau).\phi_n(z) \tag{3.7}$$

where $q_n(\tau)$ are the amplitudes of vibration and $\phi_n(z)$ are modal functions, solutions of the free beam linear equation with associated boundary conditions. According to this approach, the mode function compatible with the clamped-free conditions of the beam free oscillation is

$$\phi_n(z) = -\frac{\sin(k_n) + \sinh(k_n)}{\cos(k_n) + \cosh(k_n)} \left[\cos(k_n z) - \cosh(k_n z)\right] + \left(\sin(k_n z) - \sinh(k_n z)\right) \tag{3.8}$$

The Galerkin decomposition method can be truncated to the fundamental mode of vibration under some particular conditions, we consider only one mode with $q_n = q$ [16], [78]. Taking into account that $\phi_n(z)$ satisfies the orthogonal conditions

$$\int_0^1 \phi_n(z).\phi_m(z)dz = \delta_{nm}$$

The modelling Eqs. (3-6) is transformed into the following equations:

$$\begin{aligned} &(1 + Ma_1)\, q_{\tau\tau} + \lambda q\tau + \left[k^4 + (a_2 + Ma_3)\right] \delta q \\ &\qquad + N_1 a_4 q^3 = -B\alpha a_5 i + \gamma(u^2 - 2\varepsilon u\dot{q} + a_6 \varepsilon^2 q_\tau^2) \\ &i_\tau + \mu(R_{int} + R_{load}) i = \beta B a_7 q_\tau \end{aligned} \tag{3.9}$$

The partial differential equation has been reduced to a second order ordinary differential equation for the modal amplitude of the beam deflection. The new

coefficients are defined as follows:

$$
\begin{aligned}
a_0 &= \int_0^1 \phi(z)dz = 1.0665, \quad a_1 = \int_0^1 \phi^2(z)f(z)dz = 1.3684 \times 10^{-4}, \\
a_2 &= \int_0^1 \phi^{'}(z)\phi(z)dz = 3.7107, \quad a_3 = \int_0^1 \phi^{'}(z)\phi(z)f(z)dz = 5.4094 \times 10^{-3}, \\
b_0 &= \int_0^1 \phi^{'2}(z)dz = 8.6233, \; b_1 = \int_0^1 \phi^{''}(z)\phi(z)dz = 1.5925, \; a_6 = \int_0^1 \phi^3(z)dz, \\
a_4 &= b_0.b_1 = 13.7327, \quad a_5 = \int_0^1 \phi(z)f(z)dz = 0.0116979, \quad a_7 = \frac{a_1}{a_0}.
\end{aligned}
\tag{3.10}
$$

For the purpose of numerical simulation, the wind speed flow component is assumed to be a single-frequency excitation in the form $u(\tau) = u_0 + u_1 \cos(\Omega\tau)$ of constant mean average u_0, amplitude u_1, and dimensionless frequency $\Omega_r = \frac{\omega}{\omega_0}$. This is compatible with the periodic air flow used in this work. The wind acts at $0.95 \leq z \leq 1.0$.

Eqs. (3-9) are solved numerically using the fourth order Runge-Kutta algo-

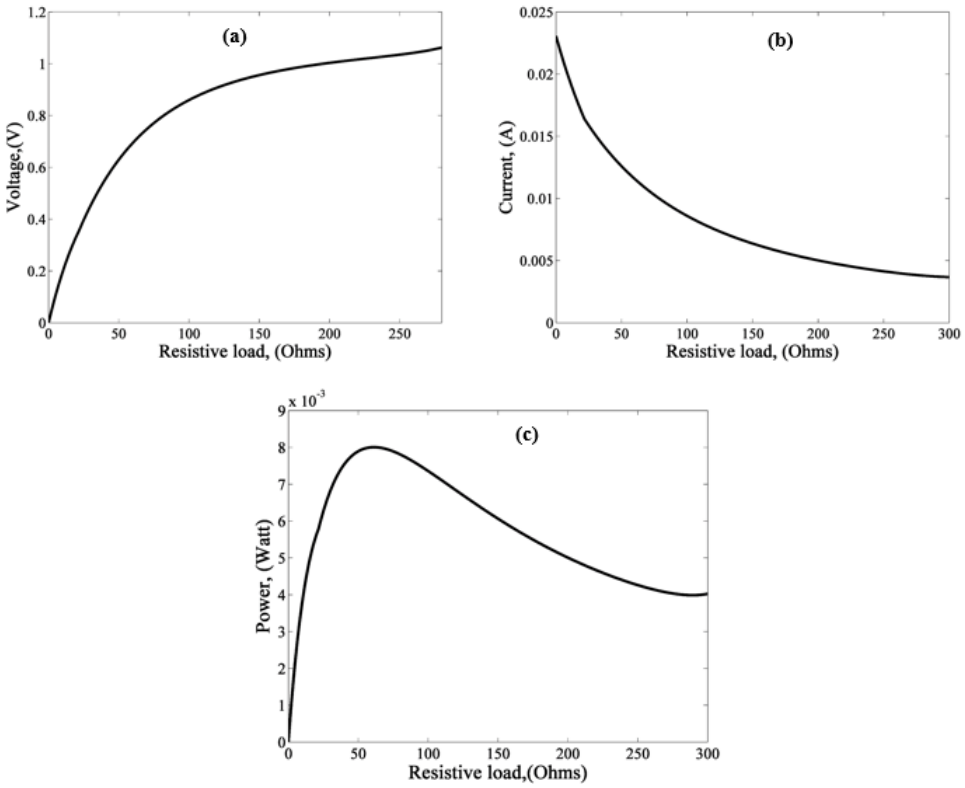

Figure 3.5: *Maximum generated energy at the resonance: (a) current vs. resistive load, (b) voltage vs. resistive load, and (c) power as a function of load resistance*

rithm. The results obtained are then used to compute the power generated by the device. Fig. 3.5 shows the variation of the current, voltage and power obtained from the numerical simulation as the resistive load increases. One finds, as for the experimental investigation, that the current decreases as the resistive load increases while the voltage increases. The power at its side first increases till a maximal value, from there it decreases as the resistance is increased further. As it appears in Fig. 3.5(c), the maximal value of the power is close to 8 mW delivered at the optimum eletrical load of $R_{load} = 60\ \Omega$.

3.2.5 Comparison between experimental and theoretical approach

The simulated and measured magnitudes of the current and power as function of the resistance load are both analysed and compared. The result of that analysis is presented in Fig.3.6.

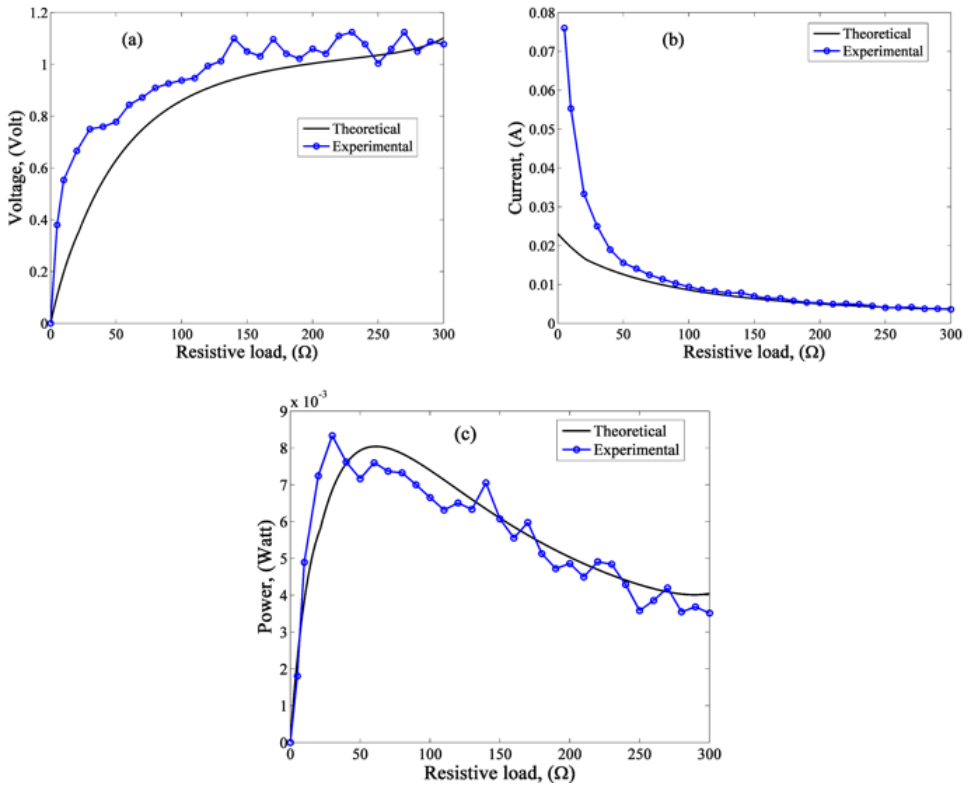

Figure 3.6: *Comparisons of the experimental and simulation for the generated (a) current versus the resistive load, and (b) power versus the resistive load.*

Experimentally, the maximum power is delivered at $R_{load} = 30\ \Omega$ whereas the same maximum is obtained at $R_{load} = 60\ \Omega$ theoretically. A fairly good qualitative agreement is observed between both results. The quantitative difference can be explained by the fact that the theory uses approximation and is limited to the one mode approximation. Moreover, the estimation of the values of physical quantities of the system cannot be considered to be quite exact here.

3.2.6 Stochastic wind flow in vibrational energy harvester

While looking for the theoretical results close to what can be really found in the field, we consider the case of wind with a stochastic (turbulent) component. It is assumed that the turbulent component of the wind flow is a bounded stationary Gaussian white noise: e.g.,

$$u\left(t\right) = u_0 + \xi_k\left(t\right) \tag{3.11}$$

where $\xi_k\left(t\right)$, the bounded noise excitation , is an harmonic function with constant amplitude, random frequency and phase defined as (Lin et *al.*, 1995; San Miguel et *al.*, 2000). [82], [83].

$\langle \xi_k\ (t)\rangle = 0, \quad \xi_k\ (t) = \sigma\,.\,\cos\left(\Omega_r\,.\,t + \psi\right), \quad \psi = \delta\,.\,B\left(t\right)$

and $\quad C_{\xi_k}\left(\tau\right) = \frac{\sigma^2}{2}\,.\,e^{\left(-\frac{\delta^2|\tau|}{2}\right)}\,.\,\cos\left(\Omega_r\,.\,\tau\right)$

The terms $C_{\xi_k}\left(\tau\right)$ is the covariance function of the stochastic excitation which measures the link between the values that the signal takes at different times t and $(t + \delta t)$. σ and δ are positive constants and $C_{\xi_k}\left(\tau\right)$ is the covariance function of $\xi_k\ (t)$. $B(t)$ is a standard Wiener function defined as

$$B\left(t\right) = 2\delta\sqrt{\frac{\Omega_r}{N}}\sum_{k=1}^{N}\frac{1}{2k-1}\sin\left(\frac{(2k-1)}{N}\Omega_r t + \Gamma\right) \tag{3.12}$$

The expression of the stochastic wind is thus given as follows

$$u(t) = u_0 + \sigma\cos\left[\Omega_r t + 2\delta\sqrt{\frac{\Omega_r}{N}}\sum_{k=1}^{N}\frac{1}{2k-1}\sin\left(\frac{(2k-1)}{N}\Omega_r t + \Gamma\right)\right] \tag{3.13}$$

Γ is a random variable uniformly distributed in $[0\,,\,2\pi]$. The wind time history is presented in Fig. 3.7 showing fluctuations around the sinusoidal shape (see the zoom for $t \in [0, 1]$ in Fig. 3.7(b), 3.7(d). In this stochastic case, the numerical simulation is carried out using the Heun algorithm method [83] (San Miguel et *al.*, 2000) and not the Runge-Kutta algorithm. For this case, the standard deviation of wind speed, q-displacement, and the voltage were obtained for a range of the constant amplitude σ and noise levels.

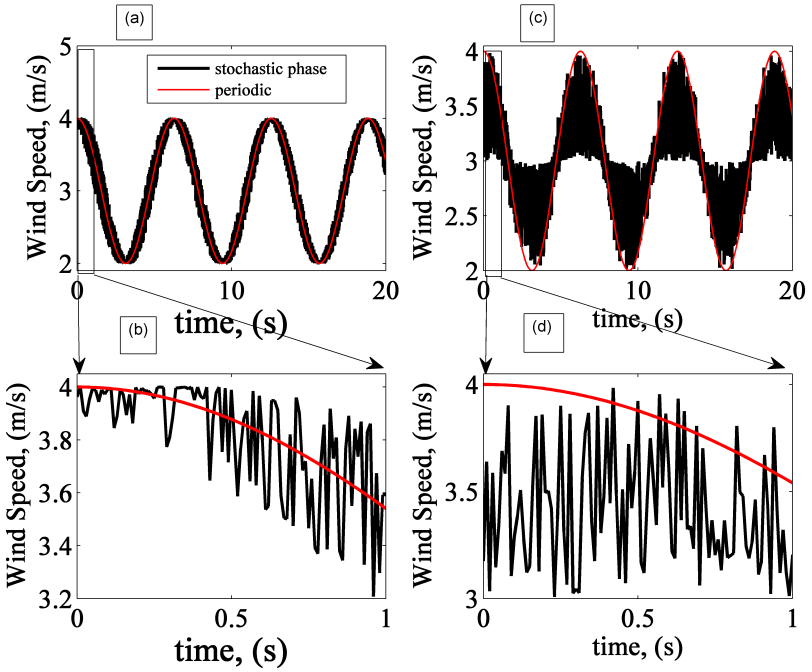

Figure 3.7: *Wind speed versus time [(a) and (b) a zoom] in case of wind with random phase and [(c) and (d) a zoom] in case of wind with random phase random amplitude for* $\Omega_1 = 1$ *and the same parameter of the system.*

Fig. 3.8 presents the variation of the power versus the resistive load when the wind fluctuation component has a random phase.

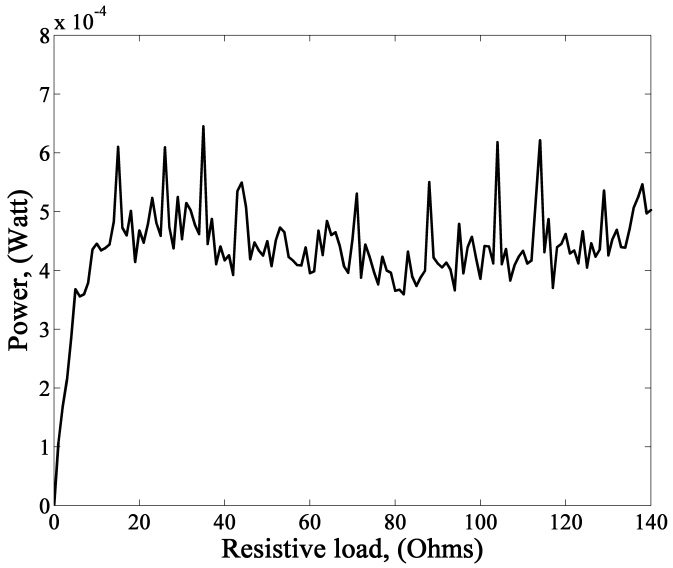

Figure 3.8: *Power as function of resistive load for* $u_0 = 3.24\ m/s, \quad \sigma = 1.5, \quad \delta = 1.6$ *and other parameters are given in the Tables 3.1 and 3.2 in case of wind with random phase.*

On Fig. 3.8 is plotted the Power as function of resistive load for $u_0 = 3.24\ m/s, \quad \sigma = 1.5, \quad \delta = 1.6$ and other parameters are given in the Tables 3.1 and 3.2 in case of wind with random phase. One can finds that the power initially increases with the load resistance, and then fluctuates around an almost constant value.

3.2.7 Field investigation

In order to complement our theoretical and laboratory investigation, we have carried out some tests in the field on a real tree. This field investigation is not to obtain the results of the laboratory set-up. But, it shows how the investigation of a laboratory model can be extended to the conversion of trees vibration into electrical energy. The experimental system appears in the photograph of Fig. 3.9. According to weather forecast 03th March 2015 at 17 P.M at Yaoundé, Cameroon, the wind speed average on this day is estimated at 1.39 m/s with a flurry of 2.5 m/s and with a pressure of 1006 mb. A small tree inside the University Campus was used for experiment. The harvesting device was attached to the tree which is connected to the transducer.

Figure 3.9: *Photograph of the set-up for the field experiment and measurement components.*

The measurement procedure is similar to what was done in the laboratory. Although this picture is really what was studied in the laboratory, one should note that the tree on which is fixed the rod having the coil at its base (entering in magnetic field) is a sort of flexible beam. This experimental text system was the same from the laboratory text. The small beam in laboratory was attached to a small eucalyptus tree (Fig. 3.9). In this field investigation, it is not possible to plot the variation of power versus the resistance load since we cannot repeat the measurement with the same natural wind. We thus decide to plot the variation of the current, voltage and power versus time for one test. The plots appear in Fig. 3.10 showing maximal values of about 24 mA, 1200 mV, and 28.8 mW for current, voltage and power respectively for a resistive load $R_{load} = 50\ \Omega$ placed in the electromagnetic device.

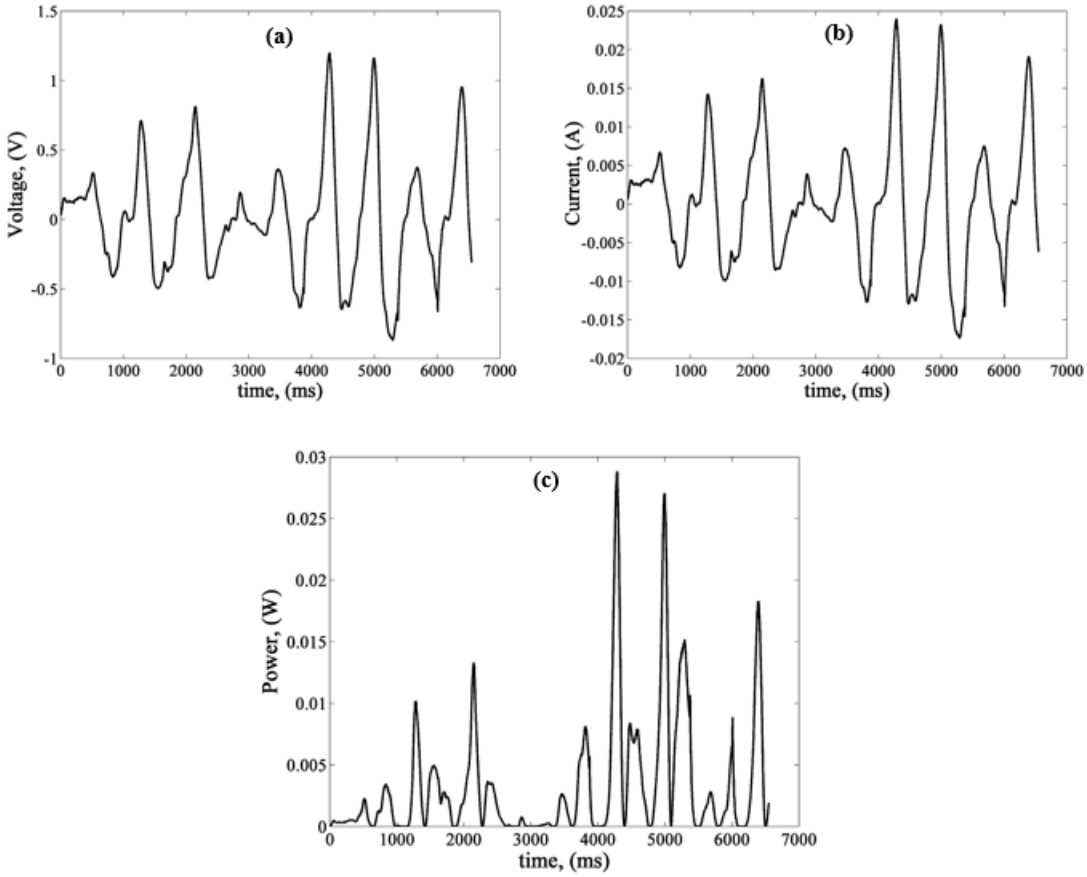

Figure 3.10: *Inducted voltage (a), Current (b), and power (c) versus time.*

3.3 Energy harvester using electromechanical pendulum

In the present section, we study experimentally and then theoretically the electric power generated by a pendulum energy harvester excited by airflow with velocity varying periodically about a mean value. The effects of the rod length and that of a spring attached to the pendulum, as well as that of a resistive load are analysed.

3.3.1 Experimental setup and description

Fig. 3.11 presents the electromechanical system made up of a pendulum with length L, on which is fixed at its center a coil. This coil is fixed on the pendulum arm such that its axis is perpendicular to the length of the pendulum. Permanent magnets with different poles are fixed on both sides of the coil. Since the coil is

placed between the polarized permanent magnets, the motion of the pendulum, consequently the movement of the coil inside the magnetic field, generates an electromotive force in the electric circuit according to emphFaraday's law. At the end of the pendulum is fixed a rectangular plate which increases the sensitivity of the pendulum to airflow excitation.

A spring with constant k is fixed at the center of the pendulum (and the other end of the spring if attached on a rigid support, the spring being kept horizontally). Since the pendulum is characterized with mass m and its length L. We use the scales to measure the weight of the pendulum arm which value is proportional to its length. For the measurement length of 1 m, the corresponding weight was 100 g. The average linear mass density $\bar{\lambda}_m$ is thus $\bar{\lambda}_m = \frac{m}{L} = 0.1\ kg/m$. If we vary the rod length, we can write: $m = m(L)$. The stiffness constant of the spring has also been measured using the usual method of extension proportional to the weight fixed at free end of the spring. The experimental setup is presented in Fig. 3.11.

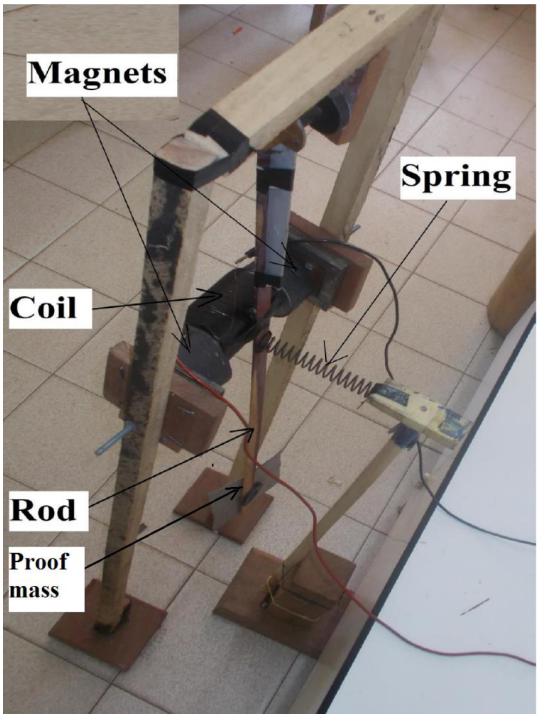

Figure 3.11: *Experimental setup of a Pendulum EHs.*

The wind drag coefficient C_d, is a dimensionless number, which depends upon

the shape of the solid and upon the Reynolds number for the fluid flow. The average drag coefficient C_d over the laminar and turbulent portion of the plate is taken as $C_d = 0.2$ (see Ref. [87]). Using the logarithmic decrement experimental measure, the damping coefficient is found to be about 0.03 N/s. The exposed area of rod/prof mass A_E was determined by using the mathematical formula $A_E = a \times b + L \times lar$. The periodic airflow velocity has an amplitude $u_{max} = 0.6\ m/s$ and its frequency can be obtained from the experimental curves (see below). The iron core relative permeability is 1200 as in Ref. [88]. The mechanical rotation energy of the motion is converted to electrical energy by electromagnetic coupling. The output voltage is measured by using a PC Lab 2000 LT portable oscilloscope connected to electrical part.

The parameters values used in the experimental study are given in Table 3.3 for the parameters of the electrical and magnetic part and Table 3.4 for the parameters of the mechanical part.

Table 3.3: Parameters of the electrical and magnetic components of the energy harvester.

Characteristic	**Value**	**Parameter**	**Value**
Coil resistivity ρ_{cu}	$1.8\ \times 10^{-8}\ \Omega.m$	Iron permeability	1200
Coil section s_{cu}	$9.065\ \times 10^{-8}\ m^2$	Air permeability μ_0	$4\pi \times 10^{-7}$
Coil radius r_{cu}	$175 \times 10^{-6}\ m$	Magnetic field B	600.0 mT
Coil height h_b	$10.0cm$	wire length l_w	78.5 m
Coil resistance R_{cu}	$14.69 \times 10^{-8}\ m^2$	Wire turns N	500
Coil mass m_b	86 g	Coil diameter D_b	0.0501 m

Table 3.4: Values of the parameters of the mechanical part.

Characteristic	**Value**	**Parameter**	**Value**
Rectangular (a, b)		Pendulum linear densityλ_m	0.1 kg/m
proof mass M	20.0 g	Air density ρ_a	1.205 kg/m^3
Height a	$20 \times 10^{-2}\ m$	Rod mass $m(L)$	$\lambda_m.L$
Rod width lar	$4.5 \times 10^{-2}\ m$	Exposed are A_E	$7.5 \times 10^{-2}\ m^2$
Width a	$15.0 \times 10^{-2}\ m$	Drag coefficient C_D	0.5
Pendulum damping λ	0.03 N/s	—	—

3.3.2 Experimental procedure of device and results

The following materials were used to construct the pendulum harvesting device:
∗ (02) permanent magnets of $0.6T$ intensity,
∗ (01) coil of 10 cm height, made of 78.5 m of electric wire length,
∗ (05) different pendulum arm length of 0.5; 0.75; 1.0; 1.25; 1.50 $meter$,
∗ (04) different springs of constant 60; 75; 90; 120 N/m,
∗ A potentiometer varying from 0.0 Ohm to 1 $Mega\ Ohm$,
∗ Iron core, fixed on the magnet support,
∗ A small rectangular light plate of $a \times b$ area (to increase the aerodynamic force),
∗ A wind tunnel based on a fan generating the periodic air flow,
∗ A set of PcLab 2000LT portable oscilloscope connected to the electric part was used to measure, analyse the data and transfer to a personal computer.
As results, Fig. 29 shows a time trace of an inductive voltage in the absence of constant spring. The voltage amplitude is about 398.5 mV and a period of 20 ms is found corresponding to a frequency of 50 Hz. The curve shows a sort of signal with two harmonics.

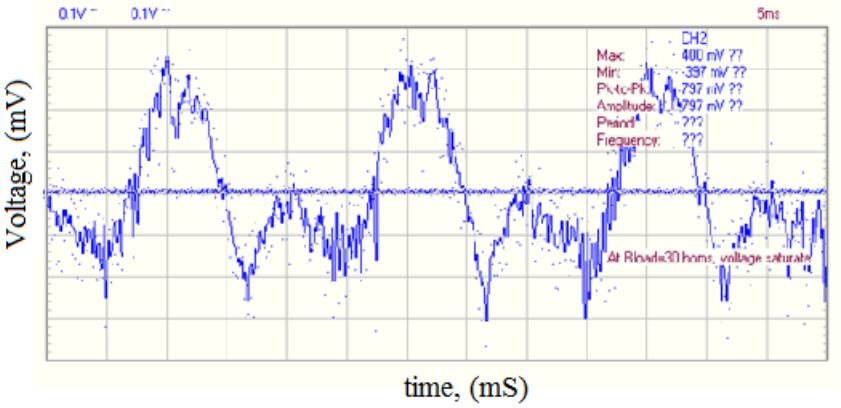

Figure 3.12: *A representative of voltage visualization on Pc oscilloscope. The load resistance is* $R_{load} = 40\ \omega$ *and there is no spring.*

Fig. 3.13 presents the maximal values of the current and power delivered to the load in the absence of spring versus the load resistance. The maximal current, and the maximal output are respectively 0.07 A and 0.06 W for a specific resistance load around $R_{load} = 20\ \Omega$.

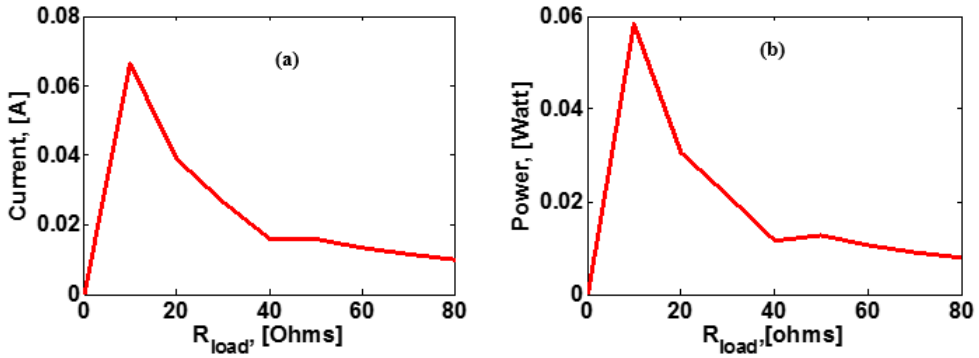

Figure 3.13: *Maximal values of the electrical current (a) and that of the power (b) as a function of the value of the resistance in the absence of spring.*

In the presence of the spring, Fig. 3.14 shows the variations of the peak current and power versus the load. It clearly shows an important increase of the current and power outputs. Indeed the peak values for current and power are respectively $I = 0.09\ A$ and $P = 0.3\ W$ (to compare to $0.07\ A$ and $0.06\ W$ in the absence of spring).

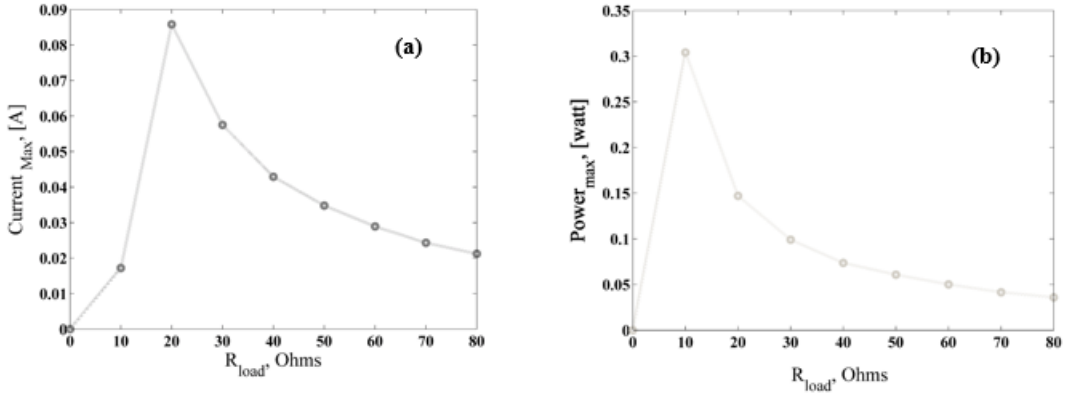

Figure 3.14: *Maximal values of current (a) and power (b) as a function of resistance load in the present of the spring for* $k = 75.0\ N/m$.

To analyse the effects of the spring constant, we have used a set of 4 springs with the following values of their constant 60, 75, 90, 120 N/m. Each spring has been fixed horizontally at the center of the pendulum and the maximal power measured. The results appear in Fig. 3.15 where one finds that an optimal choice of the spring can enhance the value of the harvested power. These experimental

results confirm the theoretical results presented in reference [19] assuming that the excitation is a sinusoidal function.

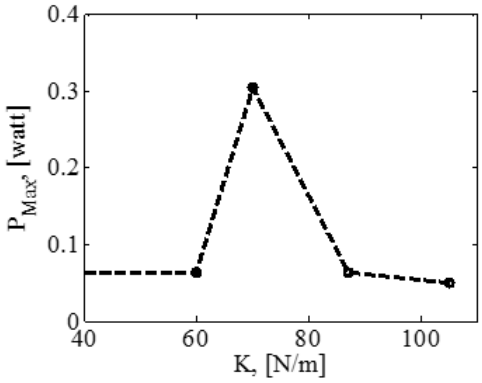

Figure 3.15: *Maximal power as function of spring constant.*

Another parameter of importance for the harvester is the pendulum length. It has been varied taking the following values: 0.5 m, 0.75 m, 1.0 m, 1.25 m and 1.50 m. The variation of the maximal values of the current and power are depicted in Fig. 3.16 showing that an optimal value for the length is $L = 1\ m$. At this maximal value, the electrical power is maximum and also depends on electrical load which is $R_{load} = 20\ \Omega$.

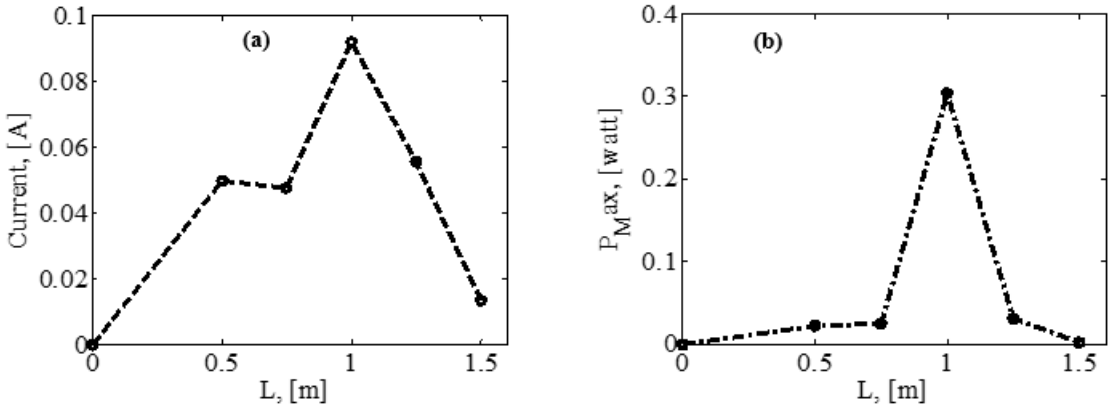

Figure 3.16: *Maximal values of the electrical current (a) and power (b) as a function of the pendulum length in the presence of spring of constant* $k = 75.0\ N/m$ *and a resistance load* $R_{load} = 20\ \Omega$.

3.3.3 Mathematical and numerical results

Fig. 3.17 gives a schematic representation of the electromagnetic pendulum harvester. Using the Newton second law of dynamics for rotational motion, the angular displacement of the pendulum is described by the following equation.

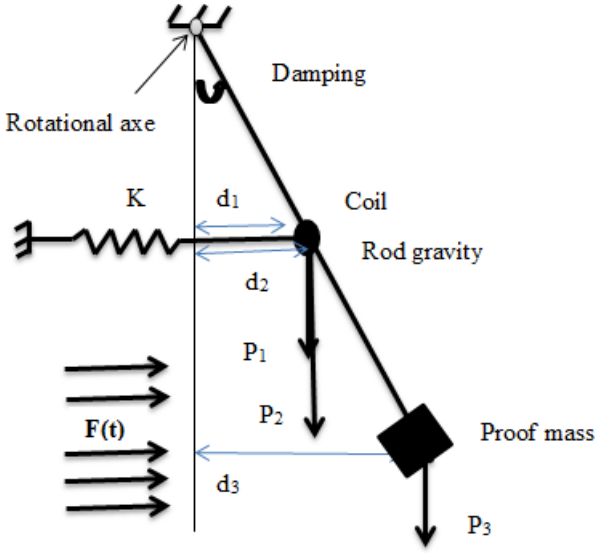

Figure 3.17: *Schematic representation of the pendulum with differences forces.*

$$J_\Delta \ddot{\varphi} + \frac{\lambda L}{2}\dot{\varphi} + (m + m_b + 2M)\frac{Lg}{2}\sin(\varphi) + \frac{L^2}{4}k.\varphi = 0 \tag{3.14}$$

where

$J_\Delta = J_{cyl-coil} + J_{rect-rod} + J_{rect-plate}$

is the total inertia relative to the rotational axis with

$J_{cyl-coil} = \frac{1}{2}m_b r_b^2 + \frac{1}{12}m_b l_b^2 + m_b\left(\frac{L}{2}\right)^2$, the inertia of cylindrical coil;

$J_{rect-rod} = \frac{1}{12}mL^2 + m\left(\frac{L}{2}\right)^2$, is the inertia of rectangular rod;

$J_{rect-plate} = \frac{4}{3}M\left(a^2 + b^2\right) + M\left(L - \frac{a}{2}\right)^2$, is the inertia of rectangular plate.

a and b are respectively the length and the width of rectangular proof plate.

We assume that the external aerodynamic excitation uniformly loading along the pendulum length and rectangular proof plate is given as:

$$F(t) = \frac{1}{2}\rho_a A_E C_D u_r^2 \tag{3.15}$$

where ρ_a is the air density, A_E is the area of the pendulum arm/proof mass (m) exposed to airflow, C_D is a dimensionless drag coefficient and u_r is the relative velocity of the airflow to the beam. It is given by:

$$u_r = u(t) - \frac{L.d\varphi}{dt} \tag{3.16}$$

$u(t)$ is the airflow speed. $L\frac{d\varphi}{dt}$ is the rod velocity. By substituting Eqs. (3-16) into Eqs. (3-15), one obtains the full expression of loading force; and the moment about the rotation axis of that loading force is given by:

$$F(t) = \frac{1}{2}\rho_a A_E C_D \left(u(t) - L\dot{\varphi}\right)^2, \tag{3.17a}$$

$$M(F(t)) = \frac{1}{2}\rho_a A_E C_D L \left(u(t) - L\dot{\varphi}\right)^2. \tag{3.17b}$$

Taking the moment of the *Laplace's* force, the equation of the mechanical part is:

$$J_\Delta\ddot{\varphi}+\frac{\lambda L}{2}\dot{\varphi}+(m+m_b+2M)\frac{Lg}{2}\sin(\varphi)+\frac{L^2}{4}k.\varphi = -\frac{L}{2}Bil_w+\frac{1}{2}\rho_a A_E C_D.L\left(u(t)-L\dot{\varphi}\right)^2 \tag{3.18}$$

where $l_w = \pi D_b N$ is the length of the copper wire.
Applying *Kirchhoff's* laws to the electric part, the equation for the electrical circuit is obtained as:

$$L_H\frac{di}{dt} + \left(R_{int}+R_{load}\right)i = Bl_w\frac{Ld\varphi}{dt} \tag{3.19}$$

where $e(t) = Bl_w\frac{Ld\varphi}{dt}$ is the (opposite) induced electromotive force obtained from *Lenz-Faraday's* Law. $L_H = \frac{\mu_0\mu_r N^2 S_b}{l_b}$ is the inductance of the coil taking into account its geometry. $R_{int} = \rho c_u\frac{l_w}{S_c}$ is the coil resistance.
Thus the pendulum energy harvester system is described by the following set of two ordinary differential equations.

$$\begin{aligned} J_\Delta\ddot{\varphi} + \tfrac{\lambda l}{2}\dot{\varphi} + (m+m_b+2M)\tfrac{lg}{2}\sin(\varphi) + \tfrac{l^2}{4}k\varphi = -\tfrac{1}{2}lBil_w \\ +\tfrac{1}{2}\rho_a A_E C_D l\left(u(t)-l\dot{\varphi}\right)^2\cos(\varphi) \end{aligned}, \tag{3.20a}$$

$$L_H\frac{di}{dt} + \left(R_{int}+R_{load}\right)i = Bl_w\frac{l.d\varphi}{dt}. \tag{3.20b}$$

Introducing the dimensionless time $\tau = \omega_1.t$, where $\omega_1 = \sqrt{\frac{1}{J_\Delta}\left[\frac{(m+m_b+2M)gl}{2} + \frac{l^2k}{4}\right]}$ is the natural frequency of the pendulum, and the dimensionless quantities,$v = \frac{i}{I_0}$, $V(\tau) = \frac{u(t)}{L.\omega_1}$ and $\varphi \equiv \varphi_1$, where $I_0 = 1\ A$, and $V(\tau)$ are the convenient normalized current and wind speed. One can write

$\varphi \equiv \varphi_1, \quad \dot{\varphi} \equiv \omega_1\dot{\varphi}_1, \quad \ddot{\varphi} \equiv \omega_1^2\ddot{\varphi}_1$

where the dot represents differentiation with respect to τ. These transformations lead to the following dimensionless equations.

$$\begin{aligned} &\ddot{\varphi}_1 + \alpha_1\dot{\varphi}_1 + \varphi_1 = -\gamma_m v + \delta\left(V(\tau)^2 - 2V(\tau)\dot{\varphi}_1 + \dot{\varphi}_1^2\right)\cos(\varphi_1) \\ &\dot{v} + \alpha_2 v = \gamma_e\dot{\varphi}_1 \\ &V^2(\tau) = u_{max}^2\cos^2(\Omega\tau) = \tfrac{1}{2}u_{max}^2\left(1+\cos(2\Omega\tau)\right) \end{aligned} \tag{3.21}$$

where $\Omega = \frac{\omega}{\omega_1}$ is the dimensionless natural frequency of the linear oscillator which is reduced to 1 (in the first of Eqs. (3-21). The dimensionless parameters have the following expressions:

$$\begin{aligned} &\alpha_1 = \tfrac{\lambda L}{2J_\Delta\omega_1}, \quad \gamma_m = \tfrac{Ll_wI_0}{2J_\Delta\omega_1^2}, \quad \delta = \tfrac{L^3\rho_a A_E C_d}{2J_\Delta}, \\ &\alpha_2 = \tfrac{(R_{int}+R_{load})I_0}{L_H\omega_1}, \quad \gamma_e = \tfrac{Bl_wL}{L_HI_0}. \end{aligned} \tag{3.22}$$

To carry out analytical procedure, we assume that the device is subjected to small amplitude of periodic airflow excitation. In this case, the angular displacement is small and one can approximate $\cos(\varphi) = 1$, and $\sin(\varphi) = \varphi$ into Eqs. (3-21) and obtain

$$\begin{aligned} &\ddot{\varphi}_1 + \alpha_1\dot{\varphi}_1 + \varphi_1 = -\gamma_m v + \delta\left(V(\tau)^2 - 2.V(\tau)\dot{\varphi}_1 + \dot{\varphi}_1^2\right) \\ &\dot{v} + \alpha_2 v = \gamma_e\dot{\varphi}_1 \\ &V^2(\tau) = u_{max}^2\cos^2(\Omega\tau) = \tfrac{1}{2}u_{max}^2\left(1+\cos(2\Omega\tau)\right) \end{aligned} \tag{3.23}$$

The steady-state response of the system was determined by applying the harmonic balance method by setting

$$\begin{aligned} &\varphi(\tau) = \varphi_{max}\cos\left(2\Omega\tau+\phi\right) = a_1\cos(2\Omega\tau) + a_2\sin(2\Omega\tau) \\ &v(\tau) = I_{max}\cos\left(2\Omega\tau+\psi\right) = b_1\cos(2\Omega\tau) + b_2\sin(2\Omega\tau) \end{aligned} \tag{3.24}$$

where $\varphi_{max} = \sqrt{a_1^2 + a_2^2}$, $I_{max} = \sqrt{b_1^2 + b_2^2}$ are the response amplitudes of the pendulum and of the electrical current. $\phi = a\tan\left(\frac{a_2}{a_1}\right)$ is the phase response relative to the input excitation. $\psi = a\tan\left(\frac{b_2}{b_1}\right)$ represents the response phase of the electrical current.

After substituting Eqs. (3-24) into Eqs. (3-23) and collecting the coefficients of $\cos(2\Omega\tau)$ and $\sin(2\Omega\tau)$, one obtains the following equations :

$$-4\Omega^2 a_1 + a_1 + 2\alpha_1\Omega a_2 = -\gamma_m b_1 + \frac{1}{2}\delta u_{\max}^2, \tag{3.25a}$$

$$-4\Omega^2 a_2 + a_2 + 2\alpha_1\Omega a_1 = -\gamma_m b_2, \tag{3.25b}$$

$$\alpha_2 b_1 + 2\Omega b_2 - 2\gamma_e\Omega a_2 = 0, \tag{3.25c}$$

$$\alpha_2 b_2 - 2\Omega b_1 + 2\gamma_e\Omega a_1 = 0. \tag{3.25d}$$

Eqs. 3-25(c) and Eqs. 3-25(d) were combined to obtain as a function of in Eqs. 3-26(a) and Eqs. 3-26(b).

$$b_1 = \frac{2\gamma_e\Omega\left(\alpha_2 a_1 + 2\Omega a_1\right)}{\alpha_2^2 + 4\Omega^2}, \tag{3.26a}$$

$$b_2 = \frac{2\gamma_e\Omega\left(2\Omega a_2 - \alpha_2 a_1\right)}{\alpha_2^2 + 4\Omega^2} \tag{3.26b}$$

Inserting Eqs.3-26(a) and Eqs.3-26(b) into Eqs.3-25(a) and Eqs. 3-25(b), after some algebraic manipulation, it follows a set of system satisfied by a_1 and a_2:

$$\begin{array}{l} \left(1 - 4\Omega^2 + \frac{4\gamma_m\gamma_e\Omega^2}{\alpha_2^2+4\Omega^2}\right) a_1 + \left(2\alpha_1\Omega + \frac{2\gamma_m\gamma_e\Omega\alpha_2}{\alpha_2^2+4\Omega^2}\right) a_2 = \frac{1}{2}\delta u_{\max}^2 \\ -\left(2\alpha_1\Omega + \frac{2\gamma_m\gamma_e\Omega\alpha_2}{\alpha_2^2+4\Omega^2}\right) a_1 + \left(1 - 4\Omega^2 + \frac{4\gamma_m\gamma_e\Omega^2}{\alpha_2^2+4\Omega^2}\right) a_2 = 0 \end{array} \tag{3.27}$$

After squaring and summing these equations, the amplitude of the rotation angle was obtained as

$$\varphi_{max} = \frac{\delta u_{max}^2}{2\sqrt{P^2 + Q^2}} \tag{3.28}$$

where

$P = 1 - 4\Omega^2 + \frac{4\gamma_m\gamma_e\Omega^2}{\alpha_2^2+4\Omega^2}$ and $Q = 2\alpha_1\Omega + \frac{2\gamma_m\gamma_e\Omega\alpha_2}{\alpha_2^2+4\Omega^2}$

The response amplitude of the electrical circuit was obtained by squaring and

adding Eqs. 3-26(a) and Eqs. 3-26(b) to have

$$I_{max} = \frac{\gamma_e \Omega \delta u_{max}^2}{\sqrt{\left(\alpha_2^2 + 4\Omega^2\right)\left(P^2 + Q^2\right)}} \tag{3.29}$$

Eqs. (3-27) were also used to determine the phase response of the rotating pendulum.

$$\phi = a\tan\left(\frac{2\Omega\left(\alpha_1\alpha_2^2 + 4\alpha_1\Omega^2 + \gamma_m\gamma_e\alpha_2\right)}{4\alpha_2^2\Omega^2 + 16\Omega^4 - \alpha_2^2 - 4\Omega^2 - 4\gamma_m\gamma_e\Omega^2}\right) \tag{3.30}$$

The corresponding phase response of the electrical signal was determined by using Eqs. 3-26(a) to Eqs. (3-27).

$$\psi = a\tan\left(\frac{2\Omega\tan(\phi) - \alpha_1}{2\Omega + \alpha_2\tan(\phi)}\right) \tag{3.31}$$

The instantaneous power transferred to the electrical load is then:

$$P_{inst} = R_{int}.\frac{\left(\gamma_e\Omega\delta u_{\max}^2\right)^2}{\left(\alpha_2^2 + 4\Omega^2\right)\left(P^2 + Q^2\right)}\cos^2(\Omega\tau + \phi) \tag{3.32}$$

The energy harvested per cycle is defined by

$$E_{cycle} = \int_0^{\tau = {}^{2\pi}/_{\Omega}} P_{inst}dt$$

where $\tau = {}^{2\pi}/_{\Omega}$ is the period of the cycle. Although an instantaneous value is sometimes of interest, the average power is often a more meaningful quantity. Now, define the average power as $P_{av} = {}^{E_{cycle}}/_{\tau}$, one obtains

$$P_{av} = R_{int}.\frac{\left(\gamma_e\Omega\delta u_{max}^2\right)^2}{2\left(\alpha_2^2 + 4\Omega^2\right)\left(P^2 + Q^2\right)} \tag{3.33}$$

The mathematical expressions of Eqs. (3-28) to Eqs. (3-33) were used to study the response behaviour for several parameters combinations. They were associated to those obtained from the direct numerical simulation of the differential equations using the classical fourth order Runge-Kutta algorithm.

3.3.3.1 The effects of the excitation frequency

The results obtained from the theoretical investigations appear in Figs. 3.18 to 3.21. Focusing on the case of Fig. 3.18, the predictions show prototypical behaviour for the response amplitudes.

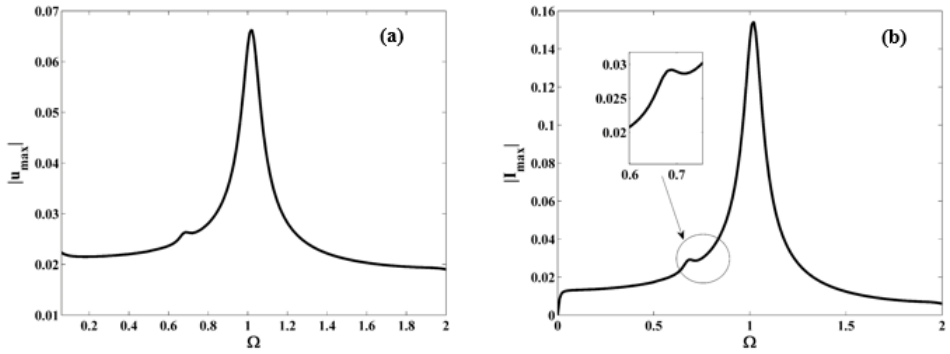

Figure 3.18: *Amplitude responses for the pendulum (a) and electric circuit (b) for* $k = 75\ N/m$, $L = 1\ m$ *and* $R_{load} = 20\ Ohm$.

The resonance occurs at $\Omega = 1$. A second resonance is visible at a frequency equal to $2/3$. In Fig. 3.19, the variation of the amplitude of the voltage and power induced in the electrical circuit are plotted as functions of dimensionless excitation frequency. There is a fairly good agreement between the analytical method and the numerical simulation.

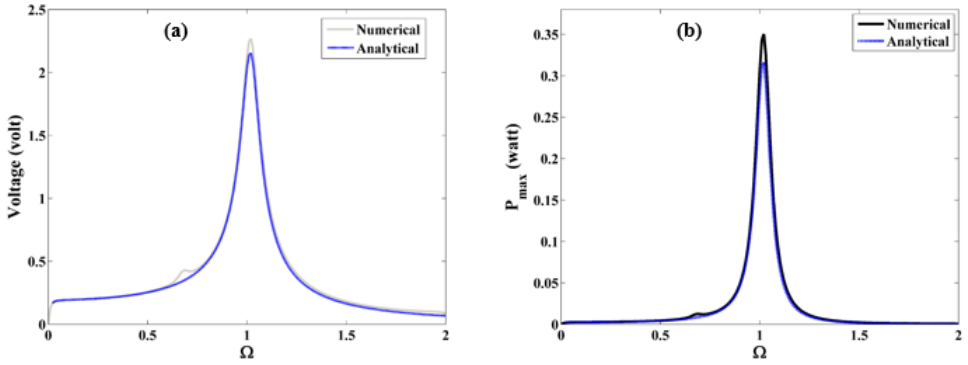

Figure 3.19: *Output voltage (a) and power (b) versus the dimensionless frequency. A continuous line (-) represents analytical prediction and the discontinuous line (...) denotes the result from simulation for* $k = 75\ N/m$, $L = 1\ m$ *and* $R_{load} = 20\ \Omega$.

3.3.3.2 The effects of resistive load

Considering now the variation of the resistive load, Fig. 3.20 shows how it affects the power delivered to the load. This is the usual resistive load-power characteristics showing the optimal functioning load corresponding to the high value of the power.

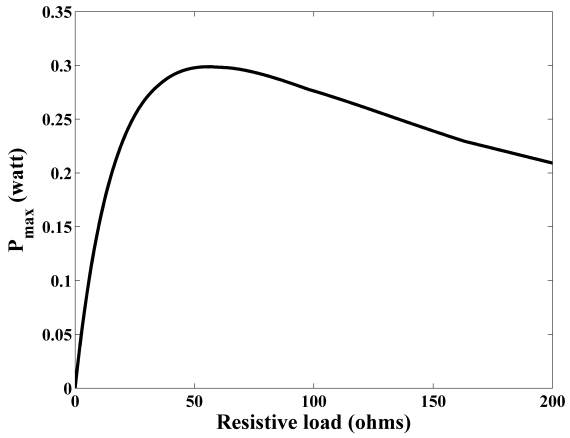

Figure 3.20: *Output power in the electric circuit versus resistive load for parameters given in Tables 3.1 and 3.2 and for* $k = 75\ N/m$.

3.3.3.3 The effects of sprint constant and rod length

As concerns the effects of pendulum length and spring coefficient, we have plotted in Fig. 3.21 the variation of power in terms of those two parameters. As it was observed in the experimental part, there are ranges of length and spring coefficient where the power increases. The increase leads to the highest values of the power (at $L = 1.0\ m$ in Fig. 3.21(a) and $k = 80\ N/m$ in Fig. 3.21(b)) followed by a decrease as those two parameters continue to increase.

3.3.4 Comparison between the experimental and theoretical results

This subsection compares the results from the experiment to those obtained from the experimental investigation considering the electric output power. Fig. 3.22 to Fig. 3.24 contain the comparative figures.

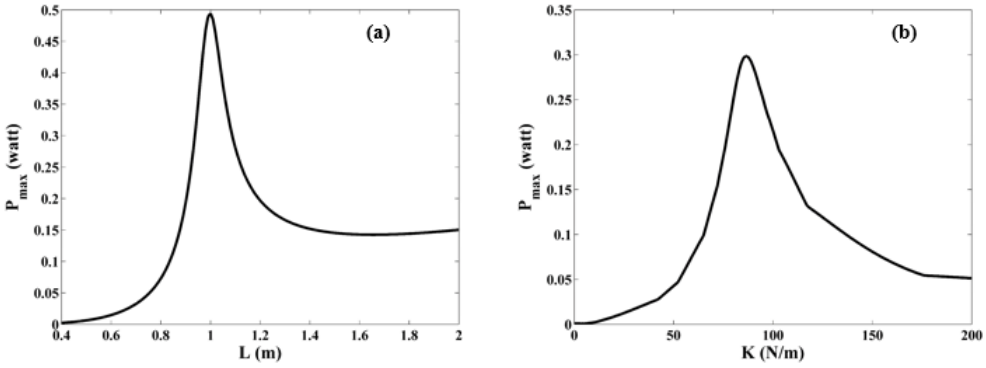

Figure 3.21: *Electrical output power as function of pendulum length (a) with* $k = 80\ N/m$ *and as function of spring constant (b) with* $L = 10\ m$.

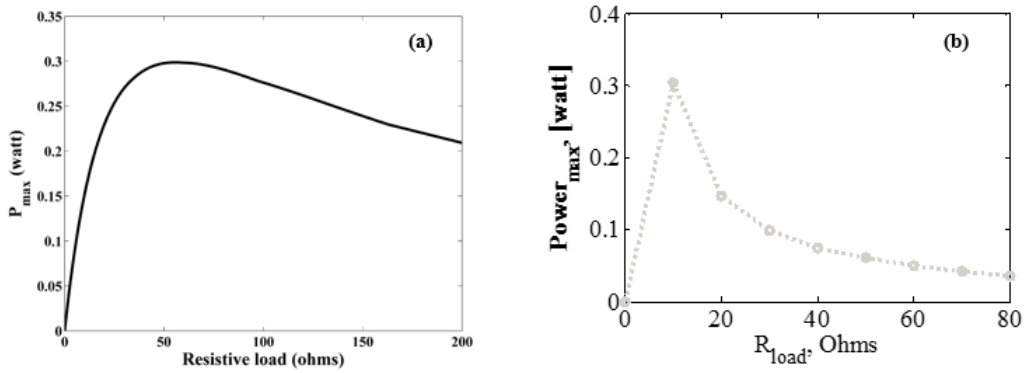

Figure 3.22: *Output power versus resistance load from the theoretical investigation case (a), and from experiment (b) for* $k = 75\ N/m$.

One finds the same qualitative behavior in the theoretical results as for the experimental record. A good qualitative agreement between theory and experiment in terms of peak power for several parameters has been obtained. More specifically, in Fig. 3.23, the peak response occurs where the length pendulum $L = 1.0\ m$ in both cases of study, although the maximum power are not quantitatively the same. This can be explained by several limits from the mathematical modeling that cannot perfectly taken into account from the experimental setup (same for other figures).

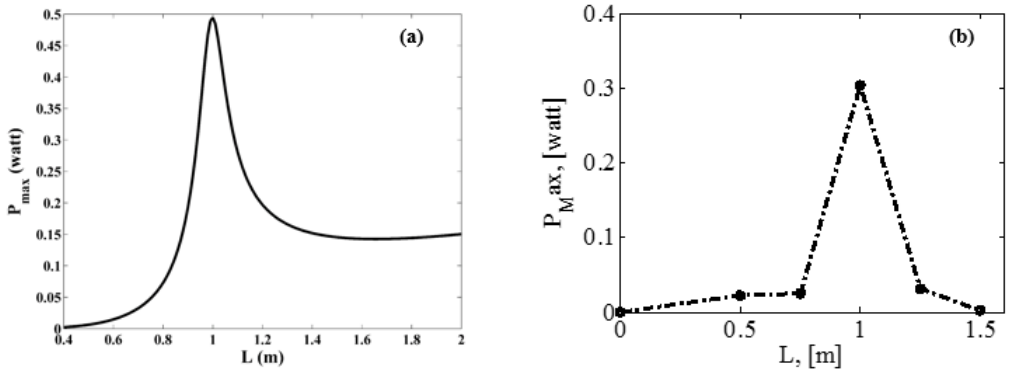

Figure 3.23: *Output power versus pendulum length from the theory case (a) and from the experiment (b) in the absence of spring and for* $R_{load} = 20\ Ohm$.

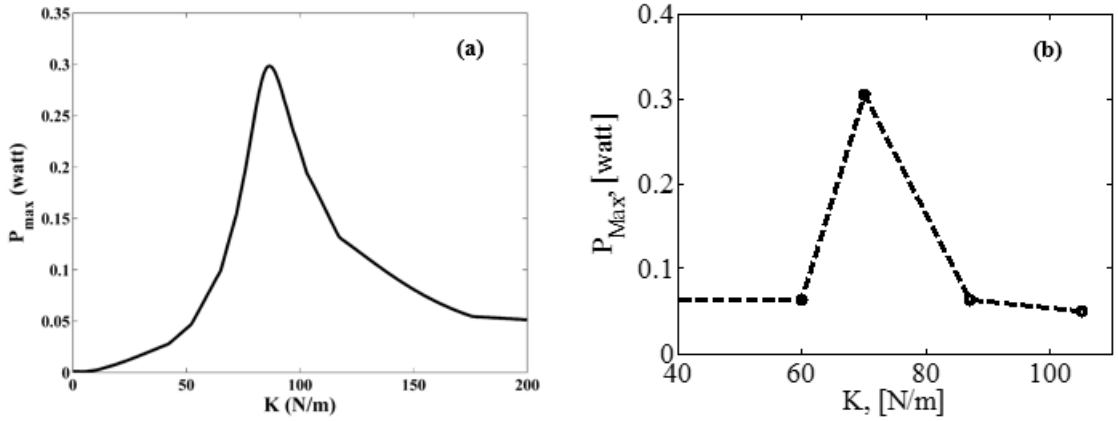

Figure 3.24: *Output power versus spring constant from the theoretical investigation (a) and from the experiment (b) for* $L = 1.0\ m$ *and* $R_{load} = 20\ Ohm$.

3.4 Circuit design, prototype testing and results

To address both major challenges involve in introduction i.e. how to efficiently convert low voltage AC waveform to DC signal, and how to boost the low voltage to a sufficiently high level to charge a battery, the power conversion requirement for the case of beam vibration driven electromagnetic induction was examined. The proposed transducer model consists of a moving cylindrical coil, rare earth permanent magnet, and an electrical coil is attached at the end of flexible beam in cantilever configuration. The magnet is attached to a fixed support system. The flexible beam will be excited by a periodic air pressure due to a rotative fan in the laboratory. The basic working principles of the passive schottky diode and voltage

multiplier are introduced. The design considerations of the proposed circuits are described.

The four stages doubler circuit voltage is a circuit voltage multiplier circuit which has a voltage multiplication factor of eight (08). Eight (08) Schottky diodes (D1, D2 ... D8) with low forward voltage drop of $\prec 0.2\ Volt$ and low current levels ($\prec 10\ mA$) are used in the proposed converter (see Fig. 3.25). Consider the input voltage waveform of the converter as an alternative voltage, the proposed converter operates mainly in two modes during one cycle of the input AC voltage. For each stage, voltage across capacitors are defined as:

$$\begin{aligned} V_{C_1} = V_P;\quad V_{C_3} = 3V_P;\quad V_{C_5} = 5V_P;\quad V_{C_7} = 7V_P \\ V_{C_2} = 2V_P;\quad V_{C_4} = 4V_P;\quad V_{C_6} = 6V_P;\quad V_{C_8} = 8V_P \end{aligned} \tag{3.34}$$

Then the output voltage at the end of the circuit can be determined as:

$$V_{out} = 2 \times 4 \times V_P = 8V_P \tag{3.35}$$

minus of course the voltage drops across the diodes used. V_P is the peak value of the input voltage.

During the experimental demonstration, we observe that this multiplied output voltage was not instantaneous but increases slowly on each input cycle.

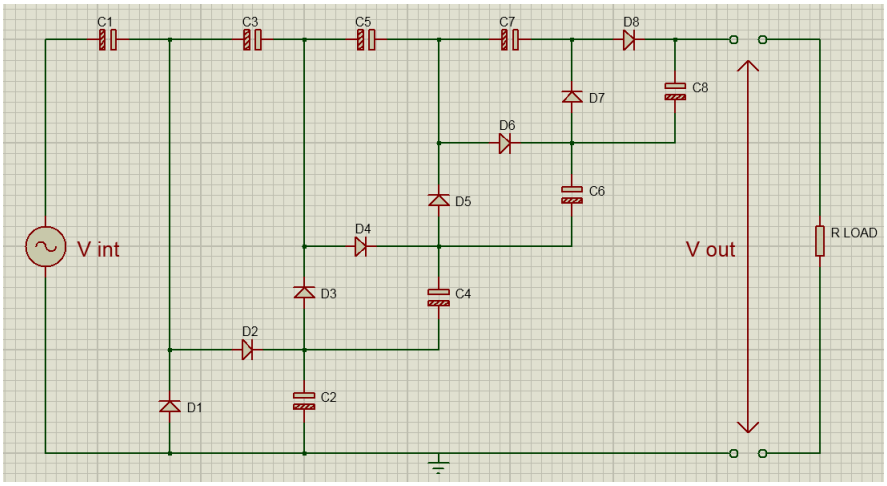

Figure 3.25: *Designed of schematic circuit diagram of a conventional voltage multiplier with an ideal voltage gain of eight.*

3.4.1 Simulation results in Pspice

Pspise software has been used to simulate and verify the multiplier circuit. This voltage multiplier will achieve a voltage gain of 8 for large input voltages. Indeed, the gain of this circuit increases with the amplitude of the input voltage, with the frequency of the input signal and the capacities of the capacitors used. But the maximum gain is 8. If the amplitude of the input voltage is 0.25 V, one can obtain the result below and by zooming on the output voltage, one can obtain the graph below as follows:

The RMS value of the output voltage is approximately 1.278 V. And so the gain

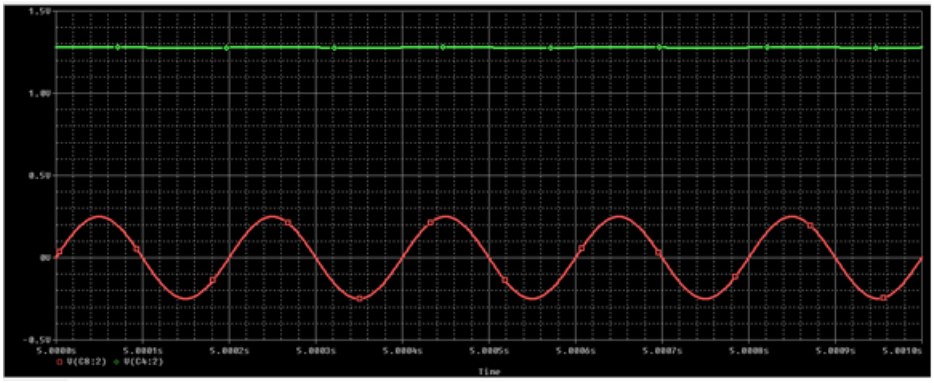

Figure 3.26: *DC bus output voltage (in green) and AC input voltage (in red) for* 0.25 V *input.*

of this circuit is $\frac{1.278}{0.25} = 5.112$.

On the other hand, if the amplitude of the input voltage is 1.0 V, the RMS value of the output voltage is 6.927 V as shown in the following two figures. Let a gain of $\frac{6.927}{1.0} = 6.927$

Finally, if the amplitude of the input voltage is 10.0 V, the effective value of the output voltage is 78.05 V as shown in the following two figures. A gain of $\frac{78.05}{10.0} = 7.805$

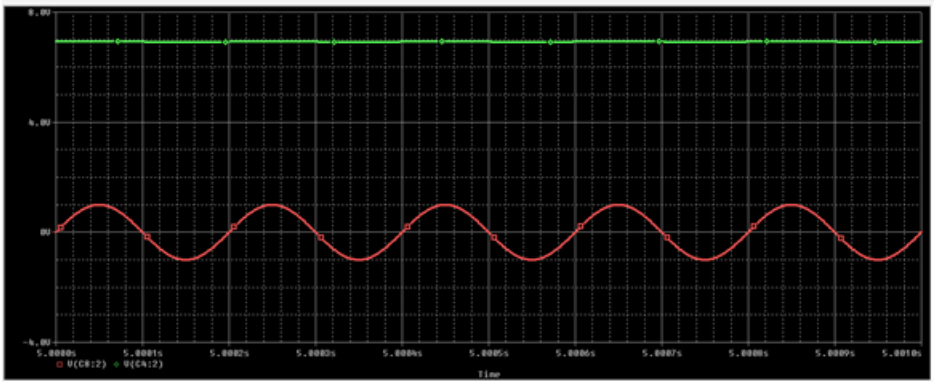

Figure 3.27: *DC bus output voltage (in green) and AC input voltage (in red) for* 1.0 V *input.*

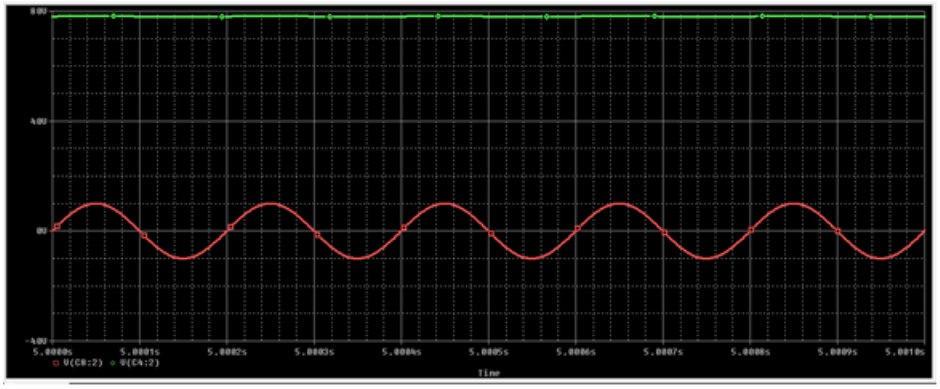

Figure 3.28: *DC bus output voltage (in green) and AC input voltage (in red) for* 10.0 V.

3.4.2 Testing of the circuit on a macro energy harvesting technology

A prototype based of voltage multiplier of Fig. 3.25 was built and tested using discrete components to verify the operation and performance of the proposed converter. The prototype realized appears in Fig. 3.29. Commercially available components are used to realize the prototype. The list of components is presented in Table 3.5.

Table 3.5: Converter circuit components selection.

Circuit components	**Name**	**Value and unit**	**Number**
Capacitors	C_i	470 μF, 16 V	$i = 1, 2, ..., 8$
Schottky diode 1N5817	D_i	200 V, 1 A	$i = 1, 2, ..., 8$
Schottky diode forward voltage	V_f	0.02 V	8
Load Resistance	R_{load}	$Variable$	1
Coil Resistance	R_{int}	20 Ω	1

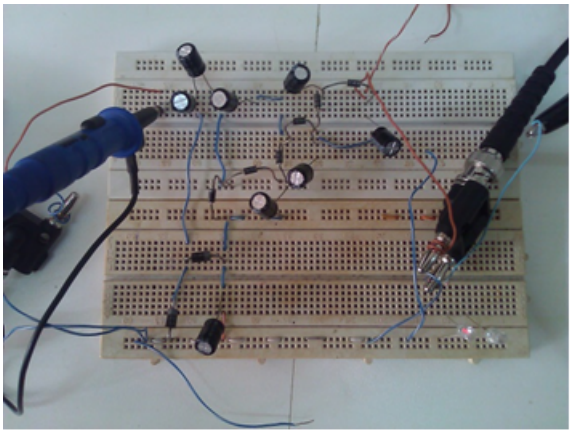

Figure 3.29: *The experimental circuit board lighting up a LED of the designed circuit of proposed converter. See the Table 3.5 for component values.*

This prototype was tested in two different ways: The circuit was first tested standalone with a PC PC-Lab 200LT function generator as the source generating sinusoidal input voltage at constant amplitude and constant frequency. Next, the circuit was tested in a proposed complete energy harvesting system with an electrodynamic (magnetic induction) vibrational energy harvester as the source with varied voltage amplitude and varied frequencies exciting by the rotate fan.
A PC-Lab 200LT which is a sort of PC function generator, producing 0.253 V peak sinusoidal output voltage, with $1 - 5.0$ Hz frequency is considered in this part for verification of the proposed converter topology. Fig. 3.30 presents a representative of conversion. An adjustable resistance box was connected to the output of the circuit, providing different load resistances. The input voltage and the positive/negative output voltages were measured with the second function of the same PC-Lab 2000LT as a function of PC oscilloscope.
Frist, the signal frequency was set to 2.25 Hz, and the output terminal was open circuit. With the amplitude gradually increasing from zero, the output voltage was monitored to check the circuit functionality. It was found that when the Energy harvester system (EHS) circuit functioning, the source voltage amplitude was not a constant sinusoidal input waveform any more (see Fig. 3.33 and Fig. 3.34), the source voltage amplitude, and frequency were gradually decreased in terms of means value maybe the statistical maximum level recorder for all the cycles

was measured at 0.359 V. at that 0.359 V harvester voltage, the corresponding dc output voltage of 2.88 V was obtained with a gain of 8. The different gain between the two different circuit test, can be explain in such that experiments are not carry out at the same condition nor for the same parameters of the control system (magnitude voltage, frequency).

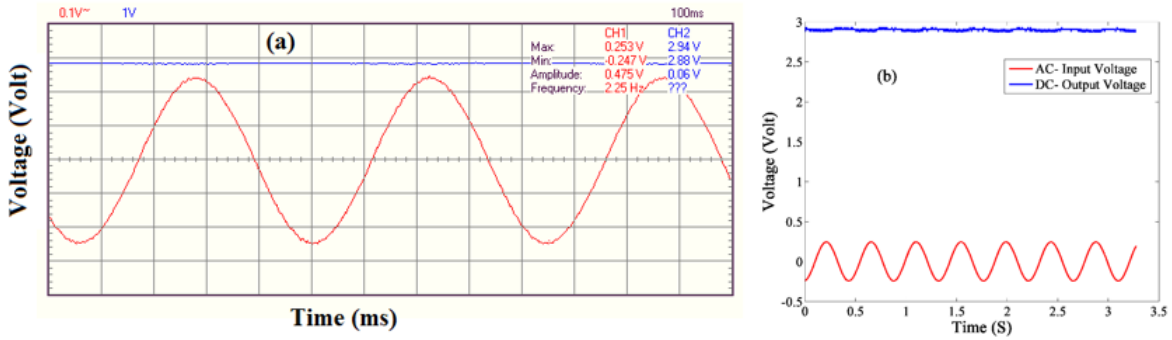

Figure 3.30: *Input voltage waveform of converter (red), and output dc voltage of converter (blue) for $f = 2.25\ Hz$ at the open circuit; (a), visualization on Pc-oscilloscope, (b) data plot.*

Next, resistive loads are connected to the circuit output, and the voltage gain and efficiency can be determined at each loading condition and input voltage amplitude. Note that considering any lost, the circuit is supposed to boost 8 times theoretically, the given input voltage which corresponds to 100% efficiency. But in the experiment, we found that the theoretical gain of 8 was more attained. The simulated components lead to a maximum efficiency of 74% for an input power voltage of 0.253 V. One important figure of merit for a power voltage harvester is its AC-to-DC power conversion efficiency: We thus define the circuit efficiency as [89] below:

$$\eta(\%) = \frac{V_{intAC}}{V_{outDC}} \times 100$$

Where we determine V_{outDC} by measuring the total power voltage in our measurement apparatus. Theoretically we assumed $V_{outDC} = V_{out} = 8V_P$.
A plot of the voltage efficiency vs. load resistance is shown in Fig. 3.31(a).
From Fig. 3.31(a), it can be seen that the circuit efficiency increase with the load resistance. It can also be observed that the maximal efficiency is about 74%.
Another measurement presented in Fig. 3.31(b) was performed to evaluate the

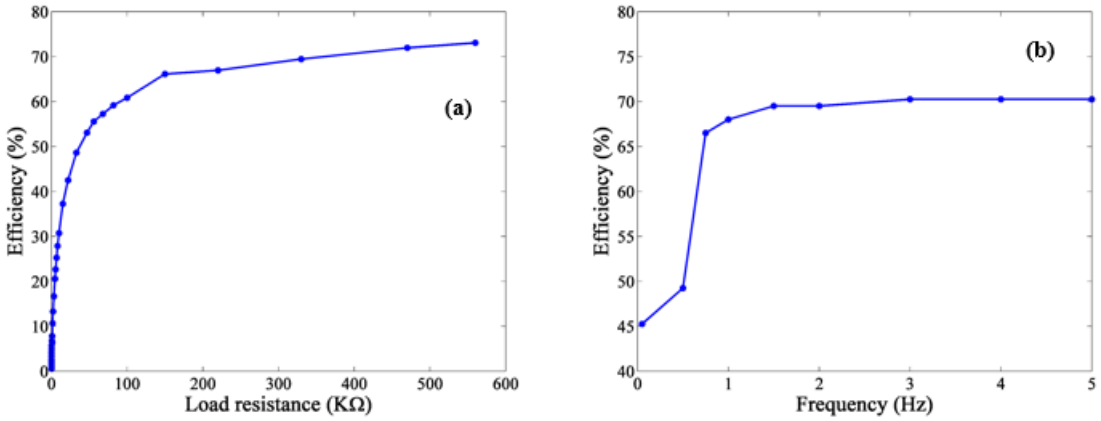

Figure 3.31: *Circuit efficiency versus load resistance at the frequency* $f = 2.25\ Hz$ *(a), and versus frequency at the open circuit (b).*

operating frequency range of the circuit. With the input voltage amplitude fixed at the minimum self-start voltage 0.3 V, and no load resistance (open circuit), the frequency was gradually increased till 5 Hz. As the frequency increases, the efficiency also increases.

3.4.3 Circuit performance measure with an energy harvesting system

In this subsection, the circuit was further tested in a proposed complete vibrational energy harvesting system of Fig. 3.32. It consists of a clamped-free beam made of wood with a transducer at its free end. The beam is subjected to the periodic pressure of a transversal wind generated by a fan. When the generator is vibrating, the electric coil moves towards the magnet. As a result, electric power will be induced across the coil according to *Faraday's* law of induction. The input of the generator is the vibration displacement of the flexible cantilever beam with the coil at its tips. This harvester offers a simplicity in its design and fabrication and can be easily implemented in remote areas, e.g., near a tree submitted to the permanent action of wind.

The output voltage amplitude versus time is shown in Fig. 3.33. One observes the generation of a variable voltage of a maximum amplitude voltage equal to 0.359 V (the period of the exciting force on the beam due to the fan rotation is

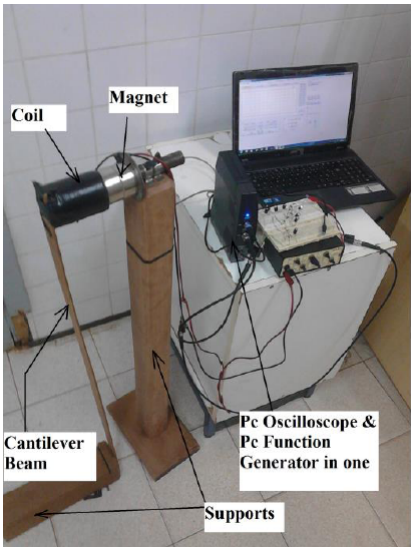

Figure 3.32: *Experimental setup of the energy harvester.*

approximately $T = 10\ s$).

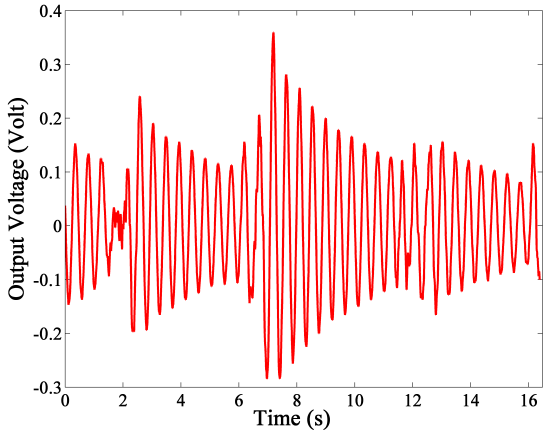

Figure 3.33: *AC output voltage at the open-circuit from the energy harvester..*

The output lead wires of the harvester are then connected to AC/DC converter of Fig. 3.29 that contains a four cascading double multiplier rectifier of 1N5817 Schottky diodes. The rectified voltage signal then passes through a resistor. For comparative purposes, the AC input generated voltage, and the DC output voltage of the circuit converter are both observed on the PC Oscilloscope in Fig. 3.33 respectively in red and blue.

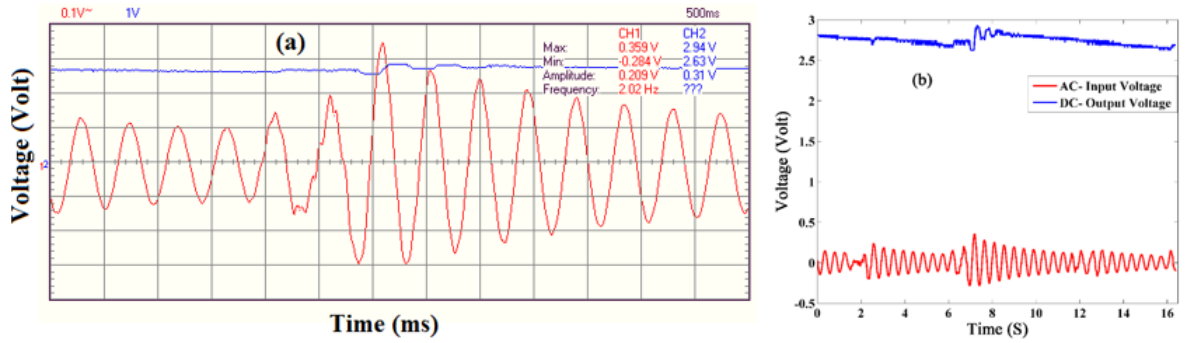

Figure 3.34: *Output AC voltage waveform from the energy harvester (red), and output DC voltage of converter (blue) from the variable/DC converter measured at the open circuit; (a), visualization on Pc- oscilloscope, (b) data plot, with the frequency of visualization part response for* $f = 2.02\ Hz$.

Note that Fig. 3.34(a) is a visualization on PC-oscilloscope during of a part of the all data plot of Fig. 3.34(b). The variable voltage coming from the energy harvester has a maximum voltage value of 0.359 V and minimum of 0.284 V and frequency response of about 2.02 Hz. Its conversion by the AC/DC converter leads to a DC root mean square ($RMS = (max + min)/2$) amplitude voltage of about 2.78 V.
In the first case of Fig. 3.30, voltage magnitude was constant during the time with a constant frequency, while in the next case of Fig. 3.34, voltage amplitude was not constant as the time varied but changing with the exciting frequency along the time. This amplitude change statistical with the time and the statistical maximum level recorded for all the cycle is observe in Fig. 3.33.

3.5 Conclusion

This chapter presented results on electromagnetic conversion of tree/beam vibration into electrical energy using a movement of coil inside the permanent magnet. The results exposed first the study of an energy harvester that uses electromagnetic induction to convert tree/flexible beam vibration into electrical energy. A laboratory test has been conducted to demonstrate that harvesting energy from tree motion is possible. The maximum power is delivered to the electrical load when its optimal resistance was equal to the sum of coil internal resistance and

the electrical analogue of the mechanical damping coefficient. It is seen that the device can produce power of the order of 8.5 mW . This was followed by a preliminary field investigation where we used a representative of tree inside the university campus to capture electric energy from tree motion. Then, the next one designed and analysed the pendulum electromechanical energy harvester, excited by a periodic air flow, taking into account the effects of spring constant and pendulum length. As it was observed in the experimental part, there were ranges of length and spring coefficient where the power increased. We presented both a theoretical approach and an experimental investigation of a method to harvest energy from wind/fan excitation using electromagnetic induction. Experiment and theory were in reasonably good agreement when using the same test conditions. Next, a circuit to rectify and boost a low AC voltage amplitude to a high DC voltage was proposed. The gain of the circuit increased with the amplitude of the input voltage, with the frequency of the input signal and the capacities of the capacitors used. But the maximum gain was 8.

Chapter Four

Results on electrostatic conversion of tree/beam vibration into electrical energy and extension to conversion of the arterial pulsating pressure

4.1 Introduction

The tree/beam vibration can be transferred to an electrostatic energy harvester with constant or variable characteristics. This chapter presents the results in the case of electrostatic energy harvester with variable area and variable permittivity. But this will also include the case of variable radius and an extension to the conversion of pulsatile blood pressure will be conducted.

Section IV-2 considers the case of a system with variable area and variable permittivity due to external vibration coming from tree/beam or other structures. Section IV-3 deals with a system with variable radius. An extension of this last case to the conversion of pulsatile blood pressure is conducted in Section IV-4. The conclusion is given in Section IV-5.

4.2 Electrostatic EH with variable area and permittivity in parallel plate.

The transduction mechanisms discussed in the literature involves changing the capacitance of parallel plate capacitor by modifying the distance between the electrodes, all other parameters remaining fixed. Let us consider the basic definition of the capacitance as $C = \varepsilon A/d$, where ε is the permittivity, A is the effective area and d is the distance between the electrodes. It is clear that three parameters can be varied to change the capacitance. Let us now consider what would happen

if we chose to vary A or ε in order to produce a variable transducer instead of varying the distance d between the electrodes.

4.2.1 Energy harvesters with variable area

First consider a capacitor in which A varies. The effective area can be changed by allowing one of the plates to move orthogonally to the direction of the electric field. Then the effective area of the capacitor is given by the area in which the two plates overlap. A schematic representation of the device studied is shown in Fig. 4.1

The operation of Fig. 4.1 can be described as a micro-actuator modelled as

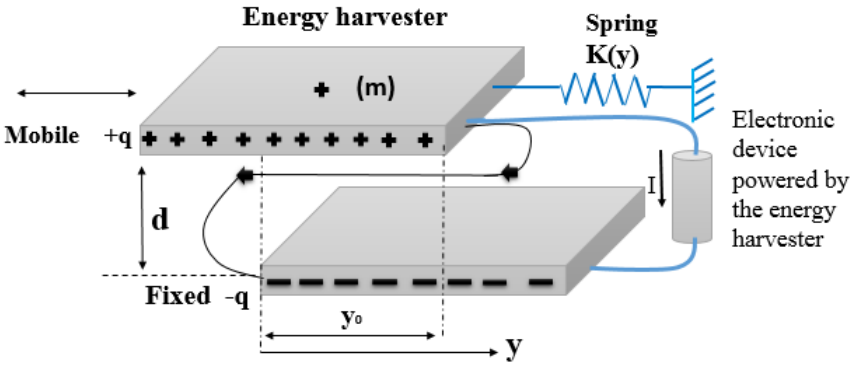

Figure 4.1: *Energy harvester capacitive transducer in which the effective area varies dynamically.*

a parallel-plates capacitor consisting of a movable top plate and a fixed bottom plate. The mobile plate is attached to a spring of variable constant $K(y)$. When an external sinusoidal force $f_0 \cos(\omega t)$ is applied on the upper plate, an electrostatic force is induced on the moveable plate.

Let us consider $R,\ I,\ q,\ y$, and $V = q/C$ as the load resistance, the induced current, charge, plate displacement, and actuation voltage respectively. We assume that (i) both plates are perfect conductors, and are separated by a dielectric layer of permittivity $\varepsilon = \varepsilon_0 \varepsilon_r$ where ε_r is the air permittivity, (ii) the plates are maintained at a fixed separation distance, (iii) the bottom plate is rigid and fixed, and the top one moves parallel to plate surface, (iv) a potential difference $v = e$ exists between the two plates.

Using the principles of mechanics and electricity, one can establish that the har-

vester is described by the following set of equations:

$$\begin{aligned} &m\ddot{Y} + a\dot{Y} + bY + cY^3 - \frac{Q^2 d}{2\varepsilon_0 w Y^2} = f_0 \cos(\omega t) \\ &R\dot{Q} + \frac{Q}{C} = 0 \quad with \quad C = \frac{\varepsilon w Y}{d} \end{aligned} \tag{4.1}$$

where w is the width of the plates, Y is the displacement along which they overlap.m, a, b and c are the mass of the moveable upper electrode, the damping coefficient, the linear and nonlinear elastic constants of the spring.
Let us write the motion (lateral position) of the moving plate and the electric charge in the following manner:

$$Y = y_0 + \hat{y}, \tag{4.2a}$$

$$Q = q_0 + \hat{q}. \tag{4.2b}$$

where y_0 and q_0 are the initial values of the displacement and charge. Then, in the dimensionless form, the electromechanical system is governed by the set of equations rewritten as:

$$\begin{aligned} &\ddot{y} + \alpha\dot{y} + \beta y + \gamma y^3 - \eta\left[1 + 2\left(q - y\right) + \left(q^2 - 4qy + 3y^2\right)\right] \\ &\qquad -\eta\left(6qy^2 - 2q^2 y - 4y^3\right) = F_0 \cos(\Omega\tau) \\ &\dot{q} + \mu\left[1 + \left(q - y\right) + \left(y^2 - qy\right) + \left(qy^2 - y^3\right)\right] = 0 \end{aligned} \tag{4.3}$$

where we assume that $|\hat{q}|$ and $|\hat{y}|$ are small, then higher order terms more than $\hat{q}^3$, $\hat{y}^3$ and $\hat{q}\hat{y}^2$ are negligible. Then, the non-dimensional variables and parameters are given as:

$$\begin{aligned} &q = \frac{\hat{q}}{q_0}, \quad y = \frac{\hat{y}}{y_0}, \quad \tau = \omega_0 t, \quad \Omega = \frac{\omega}{\omega_0}, \quad C_0 = \frac{\varepsilon_0 w y_0}{d} \\ &\alpha = \frac{a}{m\omega_0}, \quad \beta = \frac{b}{m\omega_0^2}, \quad \omega_0 = \sqrt{\frac{b}{m}}, \quad \gamma = \frac{cy_0^2}{m\omega_0^2} \\ &\eta = \frac{q_0^2}{2m\omega_0^2 C_0 y_0^2}, \quad \mu = \frac{1}{R\omega_0 C_0}, \quad F_0 = \frac{f_0}{m\omega_0^2 y_0} \end{aligned} \tag{4.4}$$

The steady-state response of the set of Eqs. 4.3 are determined by applying the harmonic balance method [78] by setting

$$y = a_0 + a_1 \cos(\Omega t) + a_2 \sin(\Omega t), \tag{4.5a}$$

$$q = b_0 + b_1 \cos(\Omega t) + b_2 \sin(\Omega t). \tag{4.5b}$$

Inserting Eqs. 4.5 in Eqs. 4.3 and equating the coefficients of and separately to zero (assuming that the terms due to higher frequencies can be neglected), one obtains:

$$\begin{aligned}&\tfrac{3}{4}\gamma a_1^3+\tfrac{3}{4}\gamma a_0 a_1 a_2^2+\beta a_1+2\eta a_1+3\gamma a_0^2 a_1+\alpha a_2\Omega-a_1\Omega^2-6\eta a_0 a_1\\&\quad+4\eta b_0 a_1-a_1\Omega^2+4\eta a_0 b_1-2\eta a_0 b_1-2\eta b_1=F_0,\end{aligned}\tag{4.6a}$$

$$\begin{aligned}&\tfrac{3}{4}\gamma a_2^3+\tfrac{3}{4}\gamma a_0 a_2 a_1^2+\beta a_2+2\eta a_2+3\gamma a_0^2 a_2-\alpha a_1\Omega-a_1\Omega^2-6\eta a_0 a_2\\&\quad+4\eta b_0 a_2-a_2\Omega^2+4\eta a_0 b_2-2\eta b_0 b_2-2\eta b_2=0,\end{aligned}\tag{4.6b}$$

$$2\mu a_0 a_1-\mu a_1(1+b_0)+\mu(1-a_0)b_1+\Omega b_2=0,\tag{4.6c}$$

$$2\mu a_0 a_2-\mu a_2(1+b_0)+\mu(1-a_0)b_2-\Omega b_1=0.\tag{4.6d}$$

It comes after some algebraic manipulations that the amplitudes satisfy the following nonlinear equations

$$\begin{aligned}&\tfrac{9}{16}\gamma^2 A^6+\tfrac{3}{2}\gamma F_2 A^4+(F_2^2+G_2^2)A^2-F_0^2=0\\&B=\frac{\mu\sqrt{\rho^2+\sigma^2\Omega^2}}{D1}A\end{aligned}\tag{4.7}$$

where

$$\begin{aligned}&A^2=a_1^2+a_2^2\qquad B^2=b_1^2+b_2^2\\&D1=\Omega^2+\mu^2(a_0-1)^2\\&F_2=\beta+2\eta+3\gamma a_0^2-6\eta a_0+4\eta b_0-\Omega^2-\tfrac{2\eta\mu\sigma\rho}{D1}\\&G_2=\alpha\Omega+\tfrac{2\eta\mu\Omega\sigma^2}{D1}\\&\sigma=2a_0-b_0-1;\quad \textit{and}\quad \rho=\mu\left(2a_0^2-3a_0-a_0b_0+b_0+1\right)\end{aligned}\tag{4.8}$$

Eqs. Eqs. 4.7 will be used to plot the amplitude of the displacement and that of the charge versus the external force frequency. The comparison will then been made with the results obtained from the direct numerical simulation of the differential equations. For the numerical calculation and simulation, the values of the parameters used in this case are given in Table 4.1.

The plot in Fig. 4.2 presents the displacement amplitude and charge amplitude versus the frequencies ratio obtained from the mathematical development above and from the numerical simulation of the differential Eqs. 4.3 using the fourth order Runge-Kutta algorithm. There is a qualitative agreement between the results

Table 4.1: Characteristics of the electrostatics harvester.

Circuit components	**Value**
Plates gap,	$d = 8.85\ \mu m$
Plates width,	$w = 10\ cm$
Initial length,	$y_0 = 10\ cm$
Initial capacitance,	$1\ mF$
Initial charge,	$5 \times 10^{-7}\ C$
Proof mass,	$0.6\ g$
Damping coefficient,	$a = 0.01\ N.s/m$
Linear constant of the spring,	$b = 0.02\ N/m$
Nonlinear constant of the spring,	$c = 0.01\ N/m^3$
Air permittivity,	$\varepsilon_0 = 8.85 \times 10^{-12}\ F/m$

from the direct simulation of the differential and the results obtained from the analytical calculation. Both results indicate the decrease of the amplitude when the frequency increases. However, there is a quantitative difference which can be due to the approximation made when solving analytically Eqs. 4.3.

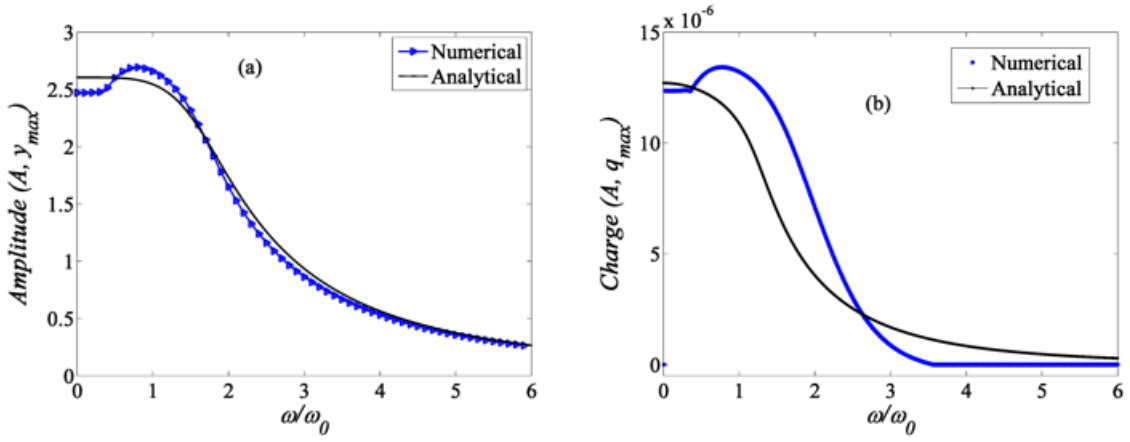

Figure 4.2: *Comparison of the analytical results and the numerical simulation results for the harvester with variable area: displacement (a) and charge amplitude (b) versus the frequency for* $f_0 = 0.2\ N,\ R_{load} = 25\ k\Omega,\ a_0 = 0.01\ m,\ b_0 = 0.006\ C$ *and other parameters in Table. 4.2*

The next steps deals with the analysis of the effects of external parameters on the power generated by the harvester. In particular the variation of the power versus the amplitude f_0 and frequency $\Omega = \frac{\omega}{\omega_0}$ of the external force will be plotted and analyzed. Moreover, the effects of the load resistance R_{load} will also be taken into consideration.

The power in the resistive load is defined as

$$P_{load} = R_{load} I^2 = \frac{V_{load}^2}{R_{load}} \tag{4.9}$$

The power and voltage are plotted in Fig. 4.3. The voltage versus the excitation amplitude is plotted in Fig. 4.3(a) while Fig. 4.3(b) presents the power versus the frequency. Then Fig. 4.3(c) presents the variation of the power as a function of the frequency while Fig. 4.3(d) corresponds to the variation of the power versus the load resistance.

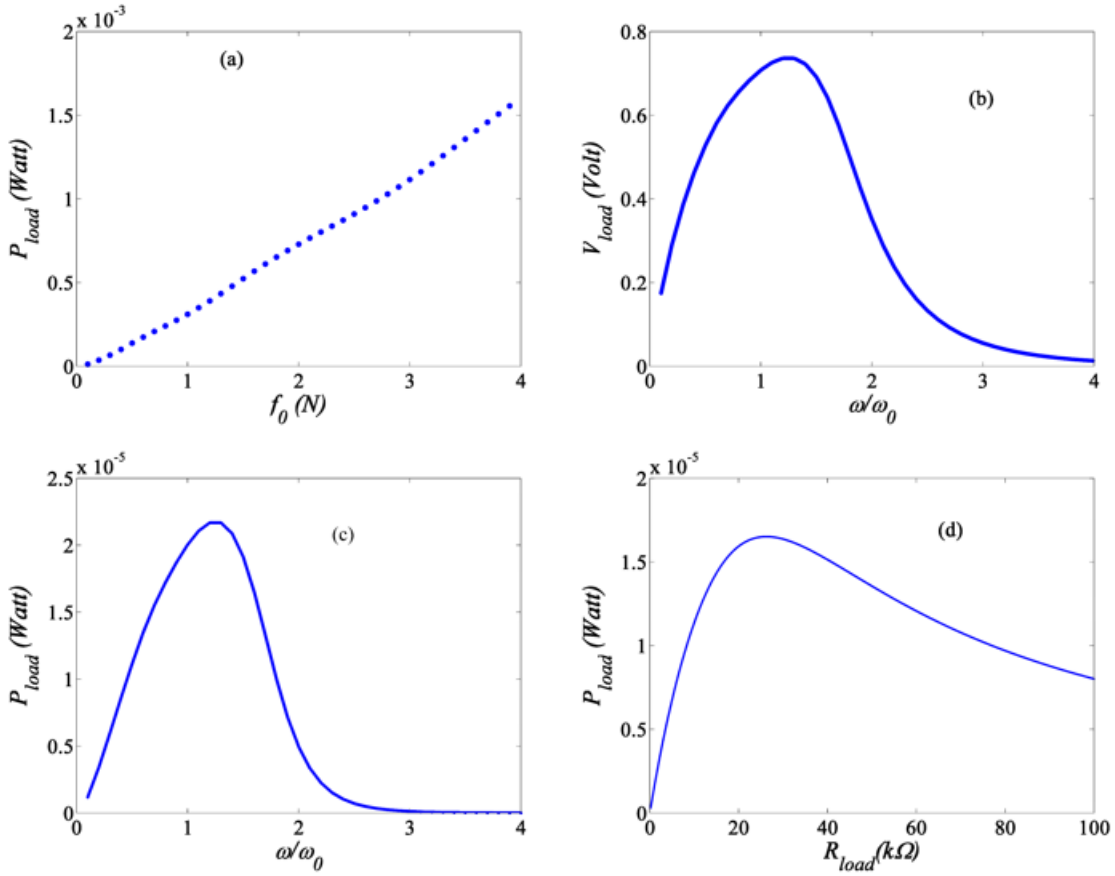

Figure 4.3: *(a) Voltage versus the amplitude of the excitation for* $R_{load} = 25k\Omega$ *and* $\omega/\omega_0 = 1.6$. *(b) Voltage versus the frequency for* $R_{load} = 25k\Omega$, $f0 = 0.2\ N$. *(c)Power versus the frequency for* $R_{load} = 25k\Omega$, $f_0 = 0.2\ N$. *(d) Power versus the load resistance for* $f_0 = 0.2\ N$ *and* $\omega/\omega_0 = 1.6$.

Fig. 4.3(a) shows that the power increases almost linearly with the amplitude of the excitation. In Fig. 4.3(b) and Fig. 4.3(c), one can observe that the harvester voltage and power of 0.75 V and 22.0 μW are obtained respectively at the dimen-

sionless frequency equal to 1.6. Above this value, a power decrease is observed to approach zero for high frequency. Fig. 4.3(d) shows the output power versus the load resistance at the input vibration frequency of 1.6. For an applied excitation amplitude of $f_0 = 0.2\ N$, the optimal power of 17.0 μW is obtained corresponding at a resistance of $R_{load} = 26\ k\Omega$.

We have also analyzed the same device, looking whether it can deliver other types of dynamical behavior such as chaos. It comes that for some selected parameters, transitions to different types of behaviors can be found as it is represented in the bifurcation diagram of Fig. 4.4. One finds that the system present period-doubling bifurcation to chaos as well as abrupt transition to chaos or to periodicity.

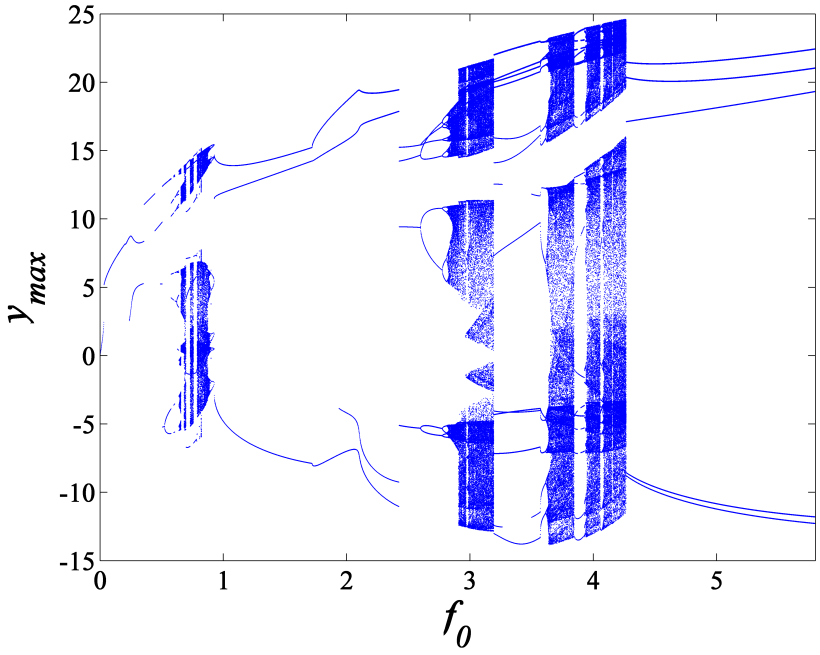

Figure 4.4: *Bifurcation diagram when the amplitude of external force varies with the following parameters* $R_{load} = 10\ k\Omega$, $\Omega = \omega/\omega_0 = 3$, $a = 0.001$, $b = 0.002$, $c = 0.001$, *and the same parameters in the Table 4.1 above.*

4.2.2 Energy harvesters with Variable permittivity

Now consider the possibility of varying the electrical permittivity of the material between the plates of the capacitor. This is normally done by laterally moving a dielectric material into and out of the space between the electrodes as shown in Fig. 56. This changes the effective value of the electric permittivity of the entire

medium between the plates of the capacitor and can be used to detect motion of the dielectric material (see Ref. [90] for some other details).

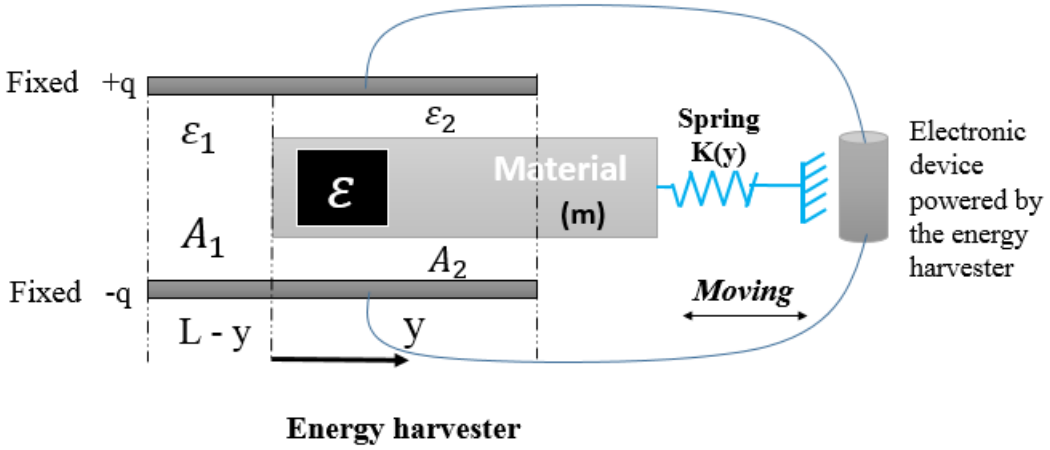

Figure 4.5: *Electrostatic energy harvester in which the permittivity varies spatially.*

The mechanical part of the system is modeled as a spring-mass-damper system assembly for which m', a', b', and c' are the mass of the moveable dielectric material, the damping coefficient, the linear and nonlinear elastic constant respectively. When the external sinusoidal forces $f_0\cos(\omega t)$ is applied on the dielectric material, an electrostatic force is induced on the moveable plate.

To determine the effective electric permittivity, ε_{eff}, consider an instant in which the moving dielectric is neither totally removed from nor totally occupying the plate gap. Then the capacitor can be divided into two pieces. One piece has area A_1 and a dielectric with permittivity ε_1. The other portion has area A_2 and electric permittivity ε_2. The active area of the capacitor is fixed at A. Thus $A = A_1 + A_2$, and the length of the capacitor plates in the direction of motion of the dielectric is l. Since there is a single voltage difference between the plates, the two capacitor segments have the same voltage. Considering the basic equation of the standard form $q = \varepsilon Ae/d$, we see that the effective electric permittivity is given by

$$\varepsilon_{eff} = \frac{\varepsilon_1 A_1 + \varepsilon_2 A_2}{A} = \frac{\varepsilon_1 y + \varepsilon_2 (l - y)}{l}, \tag{4.10}$$

The constitutive relation of the voltage applied between the plates is written as:

$$V = e = \frac{qd}{\left[\varepsilon_1 y + \varepsilon_2 \left(l - y\right)\right] w} \tag{4.11}$$

And the induced electrostatic lateral force between the plates of the capacitor is given as:

$$F_{eletr} = -\frac{\left(\varepsilon_1 - \varepsilon_2\right) q^2 d}{2w \left[\varepsilon_1 y + \varepsilon_2 \left(l - y\right)\right]^2} \tag{4.12}$$

The motion of the harvester in the case of varying permittivity is thus governed by the following equation

$$\begin{array}{l} m'\ddot{Y} + a'\dot{Y} + b'Y + c'Y^3 - F_{eletr} = f_0 \cos(\omega t) \\ R\dot{Q} + \frac{Q}{C} = 0 \quad with \quad C = \frac{\varepsilon_{eff} A}{d} = \frac{[\varepsilon_1 Y + \varepsilon_2 (l-Y)]w}{d} \end{array} \tag{4.13}$$

where w is the width of the plates, Y is the varying length of the dielectric material into and out of the space between the electrodes.
Proceeding as in the above case, one obtains the following set of equations

$$\begin{array}{l} m_1\ddot{\hat{y}} + a_1\dot{\hat{y}} + b_1\hat{y} + c_1\hat{y} - F_{elect} = f_0 \cos(\omega t) \\ F_{elect} = \frac{\chi d}{2w\varepsilon_2 l}\left[q_0^2 + 2(q_0\hat{q} - \frac{\chi}{l}q_0^2\hat{y}) + (\hat{q}^2 - 4\frac{\chi}{l}q_0\hat{q}\hat{y} + 3\frac{\chi^2}{l^2}q_0^2\hat{y}^2)\right] \\ \quad + \frac{\chi d}{2w\varepsilon_2 l}\left[(6\frac{\chi^2}{l^2}\hat{q}\hat{y}^2 - 2\frac{\chi}{l}\hat{q}^2\hat{y} - 4\frac{\chi^3}{l^3}q_0^2\hat{y}^3)\right] \\ R\dot{\hat{q}} + \frac{d}{w\varepsilon_2 l}\left[q_0 + (\hat{q} - \frac{\chi}{l}q_0\hat{y}) + (\frac{\chi^2}{l^2}q_0\hat{y}^2 - \frac{\chi}{l}\hat{q}\hat{y}) + (\frac{\chi^2}{l^2}\hat{q}\hat{y}^2 - \frac{\chi^3}{l^3}q_0\hat{y}^3)\right] = 0 \end{array} \tag{4.14}$$

Then, in the dimensionless form, the system with variable permittivity is governed by the set of Eqs. 4.15:

$$\begin{array}{l} \ddot{y} + \alpha_1\dot{y} + \beta_1 y + \gamma_1 y^3 - \eta_1\left[1 + 2\left(q - \chi y\right) + \left(q^2 - 4\chi q y + 3\chi^2 y^2\right)\right] \\ \quad -\eta_1\left(6\chi^2 q y^2 - 2\chi q^2 y - 4\chi^3 y^3\right) = F_{01}\cos(\Omega_1\tau) \\ \dot{q} + \mu_1\left[1 + \left(q - \chi y\right) + \left(\chi^2 y^2 - q y\right) + \left(\chi^2 q y^2 - \chi^3 y^3\right)\right] = 0 \end{array} \tag{4.15}$$

The non-dimensional variables and coefficients are given in Eqs. 4.16 as:

$$\begin{array}{l} q = \frac{\hat{q}}{q_0}, \quad y = \frac{\hat{y}}{l}, \quad \tau = \omega_{01}t, \quad \Omega_1 = \frac{\omega}{\omega_{01}}, \quad \chi = \frac{\varepsilon_1 - \varepsilon_2}{\varepsilon_2} \\ \alpha_1 = \frac{a'}{m_1\omega_{01}}, \quad \beta_1 = \frac{b'}{m_1\omega_{01}^2}, \quad \omega_{01} = \sqrt{\frac{b'}{m_1}}, \quad \gamma_1 = \frac{c'l^2}{m_1\omega_{01}^2} \\ \eta_1 = \frac{\chi q_0^2}{2C_{01}m_1\omega_{01}^2 l}, \quad \mu_1 = \frac{1}{R.C_{01}\omega_{01}}, \quad F_{01} = \frac{f_0}{m_1\omega_{01}^2 l}, \quad C_{01} = \frac{\varepsilon_2 wl}{d} \end{array} \tag{4.16}$$

The steady-state response of the set of eqs. Eqs. 4.15 is determined by applying the harmonic balance method as for the case of Eqs. 4.3. It comes after some algebraic manipulations that the amplitudes A_2 and B_2 (of the displacement and charge) satisfy the following nonlinear algebraic equations

$$\begin{aligned} &\tfrac{9}{16}\gamma_1^2 A_1^6 + \tfrac{3}{2}\gamma_1 F_2' A_1^4 + (F_2'^2 + G_2'^2)A_1^2 - F_{01}^2 = 0 \\ &B_1 = \frac{\mu_1\sqrt{(\rho_1^2+\Omega^2\Lambda^2)}}{D2} A_1 \end{aligned} \tag{4.17}$$

where

$$\begin{aligned} &A_1^2 = a_1'^2 + a_2'^2 \quad B_1^2 = b_1'^2 + b_2'^2 \\ &D_1 = \Omega_1^2 + \mu_1^2(a_0-1)^2 \\ &F_2' = \beta_1 + 3\gamma_1 a_0'^2 + 4\eta_1\chi b_0 - 6\eta_1\chi^3 a_0 + \eta_1\chi - \Omega_1^2 - \tfrac{2\eta_1\mu_1\rho_1\sigma_1}{D_1} \\ &G_2' = \alpha_1\Omega_1 + \tfrac{2\eta_1\Omega_1\mu_1\sigma_1\Lambda}{D_2}; \quad \Lambda = \left(2\chi^2 a_0 - \chi - b_0\right) \\ &\sigma = 2\chi a_0 - b_0 - 1; \ and \ \rho = \mu\left(2\chi^2 a_0^2 - 2\chi^2 a_0 - \chi a_0 - a_0 b_0 + b_0 + \chi\right) \end{aligned} \tag{4.18}$$

As before, Eqs. 4.17 will be used to plot the variation of the amplitudes of the mechanical displacement and charge as the frequency varies and comparison will be made with the numerical results.

We consider a parallel capacitor with a variable electric permittivity ε_{eff} as shown in Fig. 4.5. The same values for the damping coefficient and elastic constants are taken as in the preceding case. The permittivity coefficients are $\varepsilon_1 = \varepsilon_0\varepsilon_{r1}$ and $\varepsilon_2 = \varepsilon_0\varepsilon_{r2}$ where $\varepsilon_{r1} = 1.0 \quad and \quad \varepsilon_{r2} = 80$ are the relative permittivity of air and water respectively

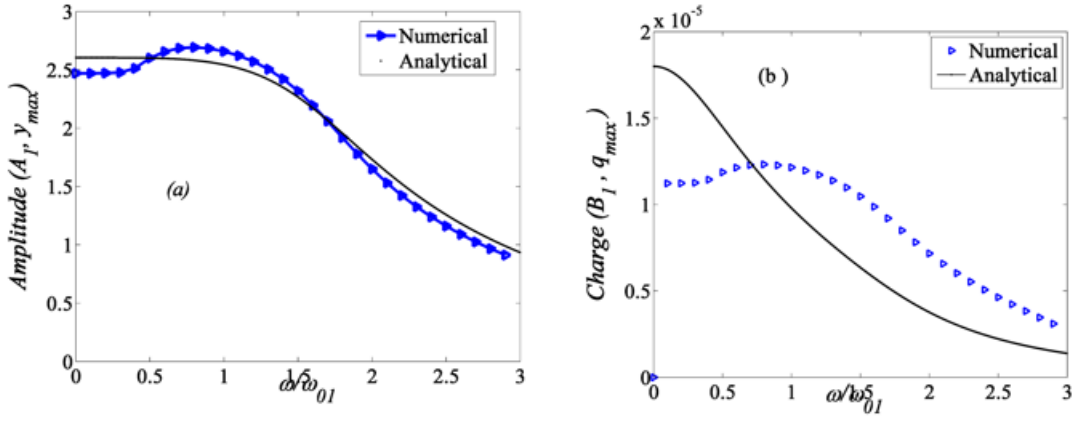

Figure 4.6: *Comparison of the analytical results and the numerical simulation results for the harvester with variable permittivity: (a) displacement and (b) charge amplitude versus the frequency.*

The plot of Fig. 4.6 shows some qualitative agreement between both curves. But one notices small quantitative disagreement at low frequencies in the case of charge amplitude in Fig. 4.6(b).

The variations of the voltage and power in terms of the parameters of this energy harvester are plotted in Fig. 4.7 and Fig. 4.8. A maximal voltage of 0.78 V and a maximal electrical power of 30.0 μW are obtained at the resonance frequency of 1.6 in case of air and water.

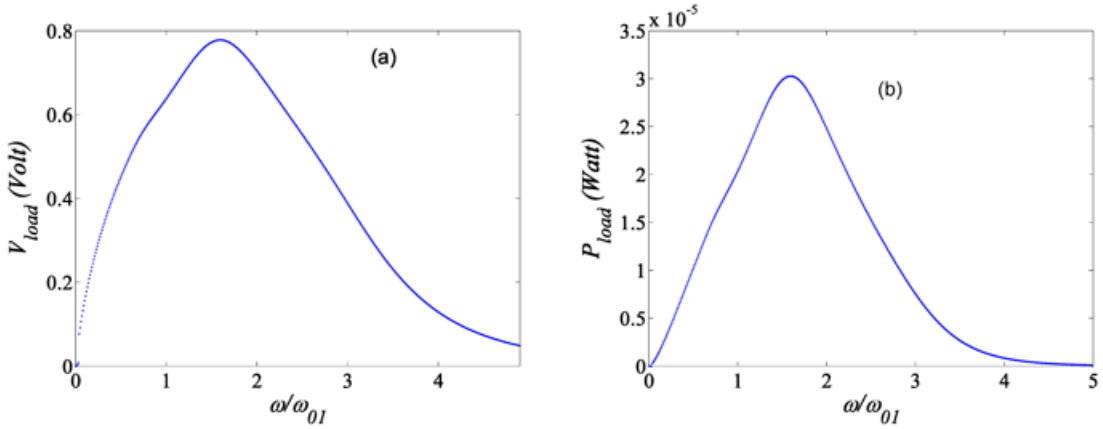

Figure 4.7: *Variation of the voltage (a) and power (b) versus the frequency in the case of the harvester with variable permittivity.*

In order to analyze the effects of the difference in permittivity coefficients on the

power generated by the harvester, we have used the following ratio $\chi = \frac{\varepsilon_1 - \varepsilon_2}{\varepsilon_2}$. The power output of the harvester is plotted for the following values of the ratio $\chi = -0.987;\ -0.875;\ -0.750$ corresponding respectively to $\varepsilon_{r1} = 1.0;\ 10;\ 20$ and for a fixed $\varepsilon_{r2} = 80.0$. It appears that the power increases with the ratio (consider the absolute value of the ratio). As in the first case, it has been found that

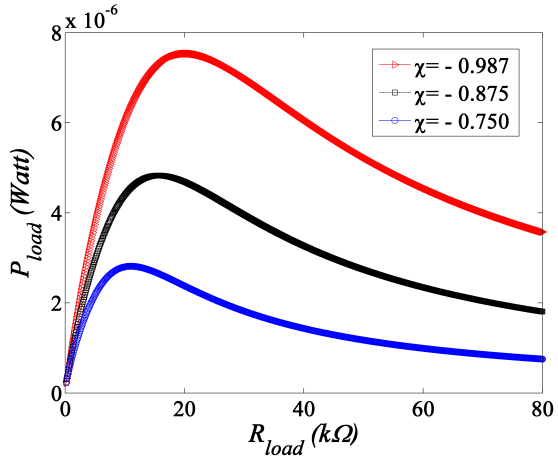

Figure 4.8: *Power generated in the resistive load versus the load resistance and different values of the ratio of the permittivity coefficients.*

by varying some parameters of this energy harvester, one can observe dynamics different to the periodic ones. The bifurcation diagram of Fig. 4.9 presents various types bifurcations points including the transition to chaos.

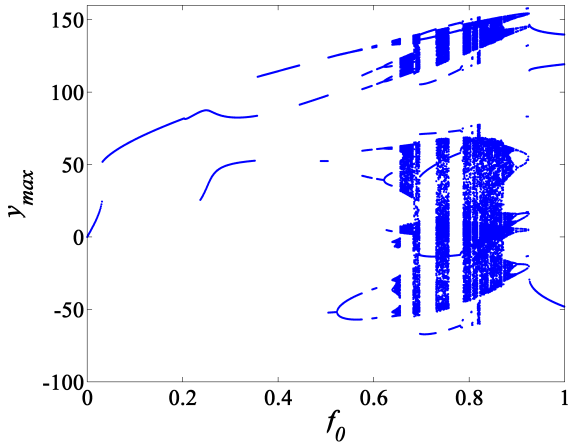

Figure 4.9: *Bifurcation diagram when the amplitude of the external force f_0 varies with fixed frequency $\Omega = \frac{\omega}{\omega_{02}} = 2$ and with the parameters $a = 0.001,\ b = 0.002,\ c = 0.001$.*

4.3 Energy harvesters with variable radius

Up to now, we have considered the parallel plate capacitor geometry only. Here we consider that we have a cylinder of radius r_1 centered inside a cylindrical shell with an outer radius of r_2. This situation is shown in Fig. 4.10. The radius ratio could be varied by allowing the outer or inner electrode to be made of a flexible material, thus deformable in presence of periodic variation. The pressure can act either inside or outside the cylindrical structure. In this configuration, the equations should take into account the membrane partial differential equation. However, one can consider only one mode of vibration with frequency comparable to that of the varying pressure.

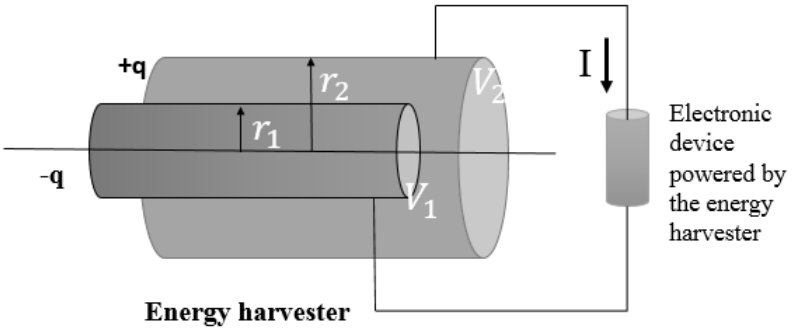

Figure 4.10: *Energy harvester capacitive transducer in which the radius ratio of cylindrical capacitor varies dynamically.*

One can thus assume that the one mode dynamics is equivalent to that of a spring-mass-damper system for which m'', a'', b'', *and* c'' are the mass of moveable outer radius electrode, the damping coefficient, the linear and nonlinear elastic constants respectively.

For this geometry, the capacitance is given by

$$C = \frac{2\pi\varepsilon l}{\ln(r_2/r_1)}, \tag{4.19}$$

where l is the cylinder length [91]-[95]. From the relation $q = CV$, we may write

$$V = e = \frac{q \ln(r_2/r_1)}{2\pi\varepsilon l} \tag{4.20}$$

This expression suggests that there are three control parameters which can be varied mechanically in order to induce a voltage, or which can be stimulated to change the voltage: the permittivity, the cylinder length, and the radius ratio r_2/r_1. The permittivity can be varied in the same manner as described for the parallel plate geometry. Similarly, the cylinder length can be made a function of time by moving one of the electrodes.

We study here the case in which the inner electrode radius is fixed and the outer radius varies. We choose this particular case as it represents the appropriate departure from the parallel plate geometry. Let us remind the following constitutive relations for the voltage and the electrostatic radial force F_{elect}:

$$V = e = \frac{Q \ln(r_2/r_1)}{2\pi\varepsilon l} \tag{4.21}$$

$$F_{elect} = \frac{Q^2}{4\pi\varepsilon l r_2}. \tag{4.22}$$

Thus the equations of motion of the system are obtained as:

$$\begin{array}{l} m^{''}\ddot{r_2} + a^{''}\dot{r_2} + b^{''}r_2 + c^{''}r_{2^3} + \frac{Q^2}{4\pi\varepsilon l r_2} = f_0\cos(\omega t) \\ R\dot{Q} + \frac{Q}{c} = 0 \quad with \quad C = \frac{2\pi\varepsilon l}{\ln(r_2/r_1)} \end{array} \tag{4.23}$$

If we assume that the charge, voltage, and varying radius can each be expressed as a static term (subscript 0) and a small perturbation: $r_2 = r_{20} + \hat{r}_2$, $Q = q_0 + \hat{q}$ one obtains

$$\begin{array}{l} m_2\ddot{\hat{r}_2} + a_2\dot{\hat{r}_2} + b_2\hat{r}_2 + c_2\hat{r}_2^3 + F_{elect} = f_0\cos(\omega t) \\ F_{elect} = \frac{1}{4\pi\varepsilon l r_2}\left[q_0^2 + \left(2q_0\hat{q} - \frac{q_0^2}{r_{20}}\hat{r}_2\right) + \left(\hat{q}^2 + \frac{q_0^2}{r_{20}}\hat{r}_2^2 - \frac{q_0}{r_{20}}\hat{q}.\hat{r}_2\right)\right] \\ \qquad + \frac{1}{4\pi\varepsilon l r_2}\left(2\frac{q_0}{r_{20}^2}\hat{q}.\hat{r}_2^2 - \frac{1}{r_{20}}\hat{q}^2\hat{r}_2 - \frac{q_0^2}{r_{20}^3}\hat{r}_2^3\right) \\ R\dot{\hat{q}} + \frac{1}{2\pi\varepsilon l}\left\{q_0.\ln(r_{20}/r_1) + \left[\frac{q_0}{r_{20}}\hat{r}_2 + \hat{q}\ln(r_{20}/r_1)\right]\right\} = 0 \end{array} \tag{4.24}$$

Then, in the dimensionless form, the model system is governed by the set of equations rewritten as:

$$\begin{aligned}
&\ddot{r_2} + \alpha_2 \dot{r_2} + \beta_2 r_2 + \gamma_3 {r_2}^3 + F_{electr} = F_{02}\cos(\Omega_2 \tau) \\
&F_{electr} = \eta_2 \left[1 + (2.q - r_2) + (q^2 + r_2^2 - 2q.r_2) + (2q.r_2^2 - q^2.r_2 - r_2^3)\right] \\
&\dot{q} + \mu_2 \left\{1 + \left[q + \frac{r_2}{\ln(r_{20}/r_1)}\right]\right\} = 0
\end{aligned} \tag{4.25}$$

with the following dimensionless parameters

$$\begin{aligned}
&q = \frac{\hat{q}}{q_0}, \quad r_2 = \frac{\hat{r}_2}{r_{20}}, \quad \tau = \omega_{02} t, \quad \Omega_2 = \frac{\omega}{\omega_{02}}, C_{02} = \frac{2\pi\varepsilon h}{\ln(r_{20}/r_1)} \\
&\alpha_2 = \frac{a''}{m_2 \omega_{02}}, \quad \beta_2 = \frac{b''}{m\omega_{02}^2}, \quad \omega_{02} = \sqrt{\frac{b''}{m_2}}, \quad \gamma_2 = \frac{c'' r_{20}^2}{m_2 \omega_{02}^2} \\
&\eta_2 = \frac{q_0^2}{2C_{02} m_2 \omega_{02}^2 r_{20}^2 . \ln(r_{20}/r_1)}, \quad \mu_2 = \frac{1}{C_{02} R \omega_{02}}, \quad F_{02} = \frac{f_0}{m_2 \omega_{02}^2 r_{20}}
\end{aligned} \tag{4.26}$$

Using the harmonic balance method, it comes that the amplitude of the displacement and charge satistfy the following set of nonlinear algebraic equations:

$$\begin{aligned}
&\frac{9}{16}\gamma_2^2 A_2^6 + \frac{3}{2}\gamma_2 F_2'' A_2^4 + (F_2''^2 + G_2''^2) A_2^2 - F_{02}^2 = 0 \\
&B_2 = \frac{\mu_2}{D2.\ln(r_{20}/r_1)} A_2
\end{aligned} \tag{4.27}$$

where

$$\begin{aligned}
&A_2^2 = a_1''^2 + a_2''^2 \qquad B_2^2 = b_1''^2 + b_2''^2 \\
&D_2 = \mu_2^2 + \Omega_2^2; \qquad \rho_2 = (-a_0 + b_0 + 1) \\
&F_2'' = \beta_2 + 3\gamma_2 a_0''^2 + 2\eta_2 a_0 - 2\eta_2 b_0 - \eta_2 - \Omega_2^2 - \frac{2\eta_2 \mu_2^2 \rho_2}{D_2.\ln(r_{20}/r_1)} \\
&G_2'' = \alpha_2 \Omega_2 + \frac{2\eta_2 \mu_2 \Omega_2 \rho_2}{D_2.\ln(r_{20}/r_1)}
\end{aligned} \tag{4.28}$$

Eqs. 4.27 will be used to plot the amplitude of the displacement versus the external force frequency. The comparison will then been made with the results obtained from the direct numerical simulation of the differential equations. We consider a cylinder of static radius $r_1 = 6\ cm$ centered inside a cylindrical shell with a variable outer radius r_1 varying around a static radius term $r_{20} = 12\ cm$ as shown in Fig. 4.10. The length of the cylindrical capacitor is $l = 30\ cm$. The capacitance is $C_0 = 1\ \mu F$, with the initial charge of $q_0 = 5 \times 10^{-7} C$, the mass of a movable outer membrane is $m_2 = 6\ g$. The damping coefficient and elastic constants are those chosen for the two first cases. Values of the used parameters are given in Table 4.2

Table 4.2: Geometric and electromechanical parameters of the sample harvester.

Parameters	**Prototype value**
Length of cylindrical,	$l = 3.0 \times 10^{-2}\ m$
Initial inner radius,	$r_{10} = 12.5 \times 10^{-3}\ m$
Initial charge,	$q_0 = 5.0 \times 10^{-7}\ C$
Initial capacitance,	$C_0 = 10\ \mu F$
Static outer radius,	$r_2 = 15.5 \times 10^{-3}\ m$
Inner area,	$S = 2\pi r_{10} l = 2.355 \times 10^{-3}\ m^2$
Mass per unit inner area,	$m = 15.0 \times 10^{-3}\ kg/m^2$
Viscosity,	$a = 1.0035\ kg/m^2.s$
Linear Spring stiffness,	$b = 3\ kg/m^2.s^2$
Nonlinear Spring stiffness,	$c = 1.05\ kg/m^4.s^2$
Load resistance,	$Variable.$

The plot in Fig. 4.11 shows the value of the amplitude of the displacement of the outer membrane versus the frequencies ratio. As in the first case, one notices the decrease of the amplitude versus the frequency.

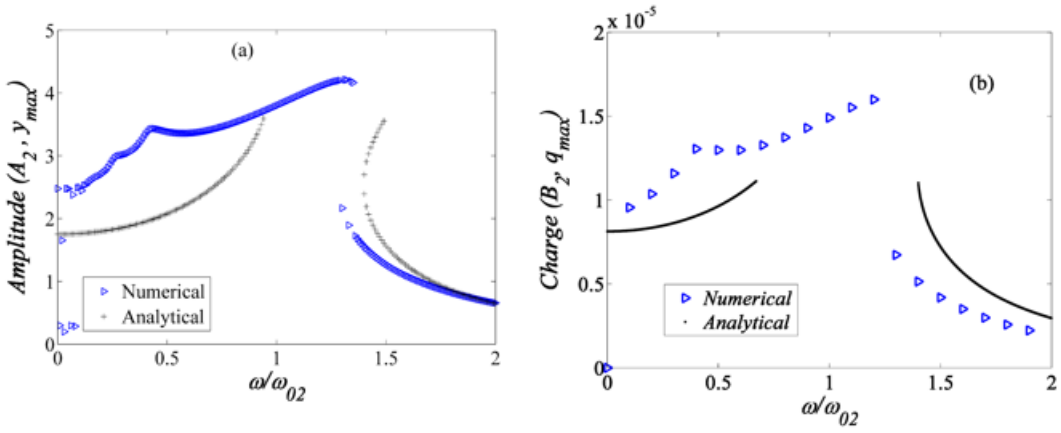

Figure 4.11: *Amplitude of the outer membrane deformation (a) and corresponding charge amplitude (b) versus the frequency of the external force.*

Fig. 4.12 presents the variation of the power in the load versus the frequency of the external force (Eqs. 4.12(a)) and versus the load resistance (Fig. 4.12(b)) for different values of the initial radius ratio $r_p = (r_{20}/r_1)$. One finds that the power increases with the increase of radius ratio r_p. One also observes that the increases of results in the increase of r_p the value of the frequency leading to the maximal power.

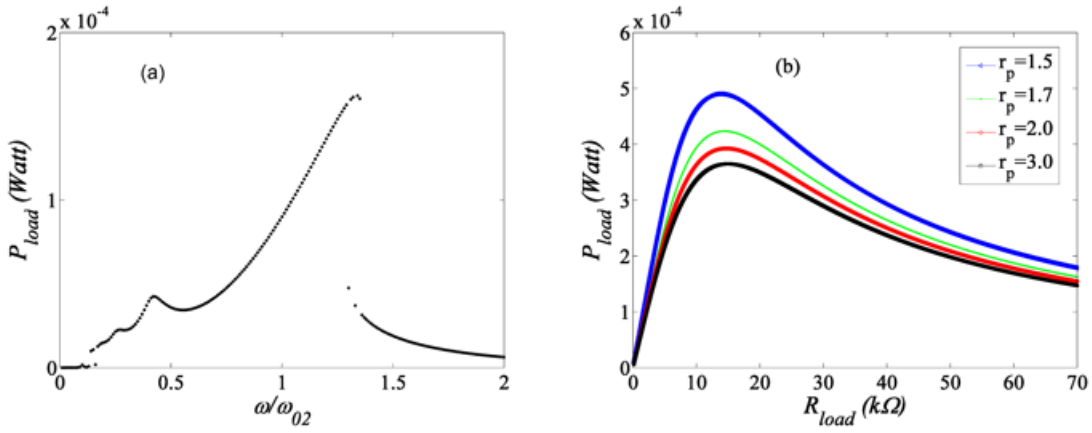

Figure 4.12: *Variation of the power produced by the cylindrical electrostatic energy harvester versus the frequency (a) and the load resistance (b) for different values of the radius ratio.*

Again, as in the preceding cases, the cylindrical shape electrostatic energy harvester can generate chaotic dynamics as it appears in the bifurcation diagram of Fig. 4.13.

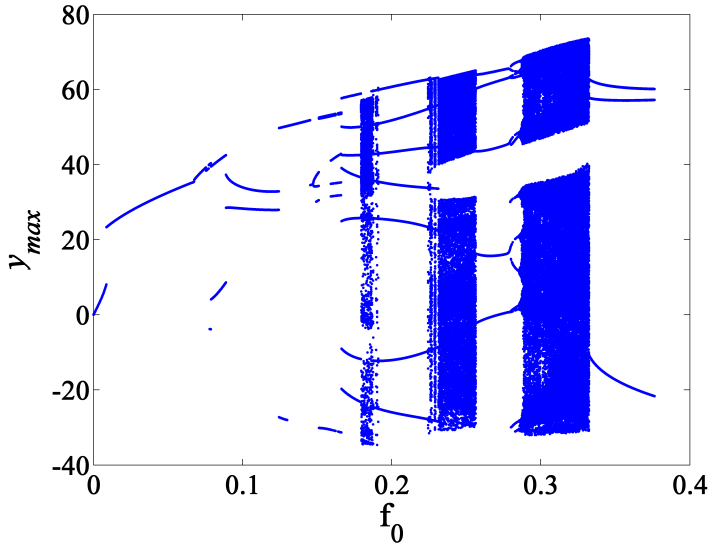

Figure 4.13: *Bifurcation diagram when the amplitude of the external force f_0 vary with the frequency* $\Omega = \frac{\omega}{\omega_{02}} = 2$ *and* $a = 0.001,\ b = 0.002,\ c = 0.001$.

4.4 Electrostatic Energy for pulsating arterial pressure

This subsection aims of using of blood pressure variation in artery with a cylindrical electrostatic membrane. The cylindrical electrostatic material is exposed to blood on the selected cover area of cylindrical artery with constant pressure flowing inside the artery. The blood pressure acts as force that modulates the gap between the two cylindrical electrodes, thus producing electricity.

4.4.1 Description and its equations

Fig. 4.14 represents the structure studied here. It is constituted of an inner cylinder of radius r_1 perfectly bonded to the arterial external wall. The inner cylinder is covered by an external cylinder of radius of r_2. When the blood flows inside the artery, its shell deforms as the results of the blood pressure. This modifies the gap between the two cylinders and thus generates an electric signal as the results of the modification of the electrostatic energy. The energy harvester is connected to the electronic device circuit through the electrodes.

The harvester is connected to the electronic device circuit through the elec-

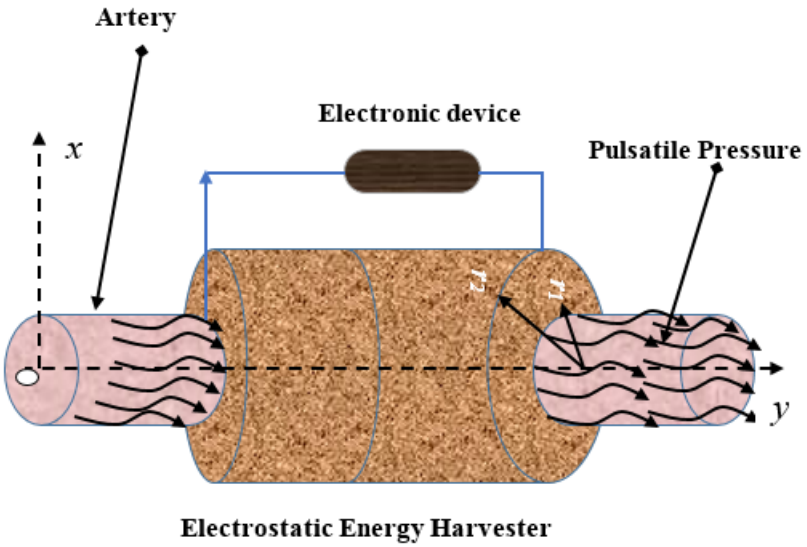

Figure 4.14: *Geometry of artery with a micro- electrostatic vibrational energy harvester system.*

trodes. The radius ratio is varied by allowing the inner electrode to be made of a flexible material, so deformable in presence of the pulsatile pressure variation.

This structure is different to the one using piezoelectric energy harvester as reported by Potkay and Brooks (2008) [96].

We assume that the blood pressure is uniformly distributed along the surface of the inner cylinder. The capacitance of the cylindrical electrostatic capacitor is given by Eqs. 4.19 and the corresponding voltage through capacitor may be written as in Eqs. 4.20.

The radial constitutive radial force, F_{elect} is given for a variation of inner radius as

$$F_{elect} = \frac{Q^2}{4\pi\varepsilon l r_1} \tag{4.29}$$

This expression suggests that there are three control parameters which can be varied mechanically in order to induce a voltage, or which can be stimulated to change the voltage. These parameters are the two radius and the length. We present the case in which the outer electrode radius is fixed and the inner radius varies. Then the radius ratio r_1/r_2 varies.

As Eqs. 4.19 and Eqs. 4.20 indicate, the transduction mechanism with cylindrical geometry leads to nonlinear constitutive relations. The charge Q, voltage $e(t)$, and varying radius r_1 can each be expressed as made of a static term (subscript 0) and a variable component (quantities with a circumflex),

$$Q = q_0 + \hat{q}; \qquad e = e_0 + \hat{e}, \tag{4.30a}$$

$$r_1 = r_{10} + \hat{r}_1; \qquad F = F_0 + \hat{F}, \tag{4.30b}$$

Then we have the following relations:

$$\begin{aligned} e(t) = e_0 + \hat{e} &= \tfrac{(q_0+\hat{q})[\ln(r_2/r_{10}) - \ln(1+\hat{r}_1/r_{10})]}{2\pi\varepsilon l}; \\ F_{electr} = F_0 + \hat{F} &= -\tfrac{(q_0+\hat{q})^2}{4\pi\varepsilon l r_{10}(1+\hat{r}_1/r_{10})} \end{aligned} \tag{4.31}$$

We may rewrite those expressions (in Eqs. 4.31 using a Taylor series expansion for $\ln\left(1+\frac{\hat{r_1}}{r_{10}}\right)$ with the assumption that $r_{10} \succ\succ \hat{r}_1$, and then we can linearize those relationship by assuming the force to consist of a large DC component and a small AC component, while the voltage similarly consists of a large DC and

small AC component. This yields

$$\begin{aligned} e(t) &= \tfrac{1}{2\pi\varepsilon l}\left[q_0\ln(r_2/r_{10}) + \hat{q}\ln(r_2/r_{10}) - \tfrac{q_0\hat{r}_1}{r_{10}} + \tfrac{q_0\hat{r}_1^2}{2r_{10}^2} - \tfrac{\hat{q}\hat{r}_1}{r_{10}} + \tfrac{\hat{q}\hat{r}_1^2}{2r_{10}^2} - \tfrac{q_0\hat{r}_1^3}{3r_{10}^3}\right] \\ F_{electr} &= -\tfrac{1}{4\pi\varepsilon l r_{10}}\left[q_0^2 + 2q_0\hat{q} - \tfrac{q_0^2\hat{r}_1}{r_{10}} + \tfrac{q_0^2\hat{r}_1^2}{r_{10}^2} + \hat{q}^2 - \tfrac{2q_0\hat{q}\hat{r}_1}{r_{10}} - \tfrac{q_0\hat{r}_1^3}{3r_{10}^3} - \tfrac{2q_0\hat{q}\hat{r}_1^2}{r_{10}^2} + \tfrac{\hat{q}^2\hat{r}_1}{r_{10}}\right] \end{aligned} \tag{4.32}$$

Balancing the static terms, one obtains:

$$e_0 = \frac{q_0\ln(r_2/r_{10})}{2\pi\varepsilon l}, \tag{4.33a}$$

$$F_0 = -\frac{q_0^2}{4\pi\varepsilon l r_{10}}, \tag{4.33b}$$

e_0 *and* F_0 are the resulting zeroth-order relations of the voltage and electrostatic force respectively corresponding to initial value. The higher order terms produce

$$\begin{aligned} \hat{e} &= \tfrac{1}{2\pi\varepsilon l}\left[\hat{q}\ln(r_2/r_{10}) - \tfrac{q_0\hat{r}_1}{r_{10}} + \tfrac{q_0\hat{r}_1^2}{2r_{10}^2} - \tfrac{\hat{q}\hat{r}_1}{r_{10}} + \tfrac{\hat{q}\hat{r}_1^2}{2r_{10}^2} - \tfrac{q_0\hat{r}_1^3}{3r_{10}^3}\right] \\ \hat{F} &= -\tfrac{1}{4\pi\varepsilon l r_{10}}\left[2q_0\hat{q} - \tfrac{q_0^2\hat{r}_1}{r_{10}} + \tfrac{q_0^2\hat{r}_1^2}{r_{10}^2} + \hat{q}^2 - \tfrac{2q_0\hat{q}\hat{r}_1}{r_{10}} - \tfrac{q_0\hat{r}_1^3}{3r_{10}^3} - \tfrac{2q_0\hat{q}\hat{r}_1^2}{r_{10}^2} + \tfrac{\hat{q}^2\hat{r}_1}{r_{10}}\right] \end{aligned} \tag{4.34}$$

These higher order terms monitor the variation of variation of the vibration and electric voltage in the electrostatic energy harvester. Thus the equations of motion of the vibration of the inner radius of artery and generated voltage are obtained as:

$$\begin{aligned} &m\ddot{\hat{r}}_1 + a\dot{\hat{r}}_1 + b\hat{r}_1 + c\hat{r}_1^3 + \hat{F}(\hat{r}_1,\hat{q}) = f(t) \\ &R_{load}\dot{\hat{q}} + \hat{e} = 0; \end{aligned} \tag{4.35}$$

m, a, b, and c are the mass of moveable inner electrode radius, the damping coefficient, the linear and nonlinear elastic constants respectively, l is the considered length of the cylinder segment, $e(t)$ is the voltage generated by the capacitor, $f(t)$ is the external exciting force per unit of area. It is the blood pressure $P(t)$ (the global force is the product of $P(t)$ and the resulting surface of the internal cylinder,$S = 2\pi r_1 l$).

4.4.2 Case of pulsating pressure force

According to Ref. [97] the pulsatile pressure takes the form of the following Fourier series:

$$P(t) = P_e + \sum_{r=1}^{4} \alpha_{0r} \cos(r\omega t) + \beta_{0r} \sin(r\omega t) \tag{4.36}$$

where P_e is the mean pressure and $\omega = \frac{2\pi}{T}$ is the pulsation frequency with a period T. r is the Fourier series rank. The values in $(mmHg)$ of P_e, α_{0r} *and* β_{0r} are given in Table 4.3 [97].

The constant means pressure P_e gives the equilibrium state of the blood flow

Table 4.3: Values of the parameters P_e, α_{0r} *and* β_{0r}.

Artery vessel	**r**	α_{0r}	β_{0r}
Aorta,	1	8.1269	−12.4156
	2	−6.1510	−1.10720
$P_e = 97.2222$,	3	−1.3330	−0.38490
	4	−2.9473	+1.16030

through the artery. If we assume the non-dimensional variables: $x = \frac{\hat{r}_1}{r_{10}}$, $q = \frac{\hat{q}}{q_0}$, $\tau = \omega_0 t$, one obtains the following set of equations for the time dependent components of the harvester:

$$\begin{aligned} &\ddot{x} + \alpha\dot{x} + \beta x + \gamma x^3 - \eta\left[(2q - x) + \left(x^2 - 2qx + q^2\right) - \left(x^3 - 2qx^2 + q^2 x\right)\right] \\ &\qquad = \sum_{r=1}^{4} \alpha_r \cos(r\Omega\tau) + \beta_r \sin(r\Omega\tau) \\ &\dot{q} + \mu\left\{\left(q - \tfrac{x}{\lambda_0}\right) + \tfrac{1}{\lambda_0}\left(\tfrac{1}{2}x^2 - qx\right) + \tfrac{1}{\lambda_0}\left(\tfrac{1}{2}qx^2 - \tfrac{1}{3}x^3\right)\right\} = 0 \end{aligned} \tag{4.37}$$

Since the simulation is carried out using international system, the pressure coefficients in Table 4.3 are converted in Pascal, this means that each coefficient is multiplied by the factor 133.32. Then, the non-dimensional variables and param-

eters are taken as:

$$\begin{aligned}
&\Omega = \frac{\omega}{\omega_0},\ C_0 = \frac{2\pi\varepsilon l}{\lambda_0},\ \omega_0 = \sqrt{\frac{b}{m}},\ \alpha_r = \frac{133.32\alpha_{0r}}{mr_{10}\omega_0^2} \\
&\alpha = \frac{a}{m\omega_0^2},\ \beta = \frac{b}{m\omega_0^2},\ \gamma = \frac{cr_{10}^2}{m\omega_0^2},\ \beta_r = \frac{133.32\beta_{0r}}{mr_{10}\omega_0^2} \\
&\eta = \frac{q_0^2}{4\pi\varepsilon l m\omega_0^2 r_{10}^2},\ \mu = \frac{1}{R_{load}C_0\omega_0},\ \lambda_0 = \ln\left(r_2/r_{10}\right)
\end{aligned} \tag{4.38}$$

All the coefficients characteristics of the transducer model in Eqs. 4.37 and Eqs. 4.38 are summarized in Table 4.4.

Table 4.4: Geometric and electromechanical parameters of the sample harvester.

Parameters	**Prototype value**
Length of cylindrical,	$l = 3.0\ \times 10^{-2}\ m$
Initial inner radius,	$r_{10} = 12.5\ \times 10^{-3}\ m$
Initial charge,	$q_0 = 5.0\ \times 10^{-7}\ C$
Initial capacitance,	$C_0 = 10\ \mu F$
Static outer radius,	$r_2 = 15.5\ \times 10^{-3}\ m$
Inner area,	$S = 2\pi r_{10}l = 2.355 \times 10^{-3}\ m^2$
Mass per unit inner area,	$m = 15.0 \times 10^{-3}\ kg/m^2$
Viscosity,	$a = 1.0035\ kg/m^2.s$
Linear Spring stiffness,	$b = 3\ kg/m^2.s^2$
Nonlinear Spring stiffness,	$c = 1.05\ kg/m^4.s^2$
Load resistance,	$Variable.$

For the artery, we consider that of a dog [98] : internal radius 12.5 mm; wall mass density 1060 kg/m^3; viscosity 0.0035 $N.S/m$. Other parameters in Table 4.4 are fixed by us taking into consideration that they should give sound results and be biologically implantable.

In the linear case the analytical results are compared to those obtained by the numerical simulation. The linearized form of Eqs. 4.37 is

$$\begin{aligned}
&\ddot{x} + \alpha\dot{x} + \beta x - \eta\left[(2q - x)\right] = \sum_{r=1}^{4} \alpha_r \cos\left(r\Omega\tau\right) + \beta_r \sin\left(r\Omega\tau\right) \\
&\dot{q} + \mu\left\{q - \frac{x}{\lambda_0}\right\} = 0
\end{aligned} \tag{4.39}$$

where $\lambda_0 = \ln\left(r_2/r_{10}\right)$

The solution of these set of Eqs. 4.39 is obtained by taking the following expres-

sions:

$$x(\tau) = \sum_{r=1}^{4} a_r \cos(r\Omega\tau) + b_r \sin(r\Omega\tau) \tag{4.40}$$

$$q(\tau) = \sum_{r=1}^{4} q_r \cos(r\Omega\tau) + p_r \sin(r\Omega\tau) \tag{4.41}$$

Inserting equations Eqs. 4.40 and Eqs. 4.41 in equation Eqs. 4.39 and identifying all the coefficients respect to $\cos(r\Omega\tau)$ and $\sin(r\Omega\tau)$, one obtains:

$$\begin{aligned} a_r &= \tfrac{F_r.\alpha_r - G_r.\beta_r}{G_r^2+F_r^2}; \quad b_r = \tfrac{G_r.\alpha_r + F_r.\beta_r}{G_r^2+F_r^2}; \\ q_r &= \tfrac{\mu^2 F - \mu r\Omega G_r}{D_r.(G_r^2+F_r^2)}\alpha_r - \tfrac{\mu r\Omega F_r + \mu^2 G_r}{D_r.(G^2+F^2)}\beta_r; \\ p_r &= -\tfrac{\mu r\Omega F_r + \mu^2 G_r}{D_r.(G_r^2+F_r^2)}\alpha_r + \tfrac{\mu^2 F_r - \mu r\Omega G_r}{D_r.(G_r^2+F_r^2)}\beta_r \end{aligned} \tag{4.42}$$

where

$$\begin{aligned} D_r &= \lambda_0\left(\mu^2 + (r.\Omega)^2\right) \\ F_r &= \beta + \eta - (r.\Omega)^2 - \tfrac{2\eta\mu^2}{D_r} \\ G_r &= \alpha(r\Omega) + \tfrac{2\eta(r.\Omega)\mu}{D_r} \end{aligned} \tag{4.43}$$

Eqs. 4.42 will be used to plot the induced current and harvester power versus time in the linear case. The comparison will then been made with the results obtained from the direct numerical simulation of the differential equations.

Fig. 4.15 presents the wave form of the pulsatile pressure (Eqs. 4.36).

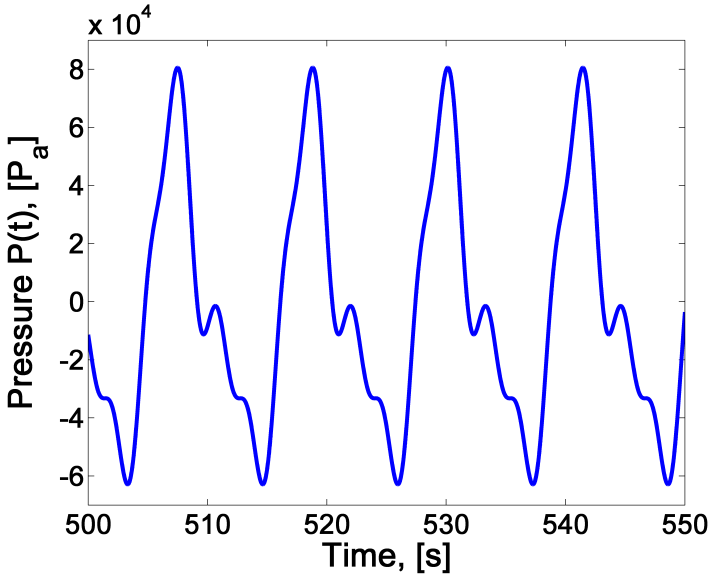

Figure 4.15: *Time trace of the pulsatile pressure with* $\omega = 7.85\ rad/s$; $R_{load} = 40\ k\Omega$, *and the same parameter given in Eqs. 4.2 and Table 4.3.*

In the linear case corresponding to Eqs. 4.39 to 4.43, Fig. 4.16(a) presents the time trace of the induced current while Fig. 4.16(b) presents that of the power generated in the load. One notice that the induced current follows the blood pressure shape. For the power, its time trace presents a high and small peaks inside one cycle. We remind the reader the power in the resistive load is defined as

$$P = R_{load} i^2(t) \tag{4.44}$$

where R_{load} is a variable resistive load.

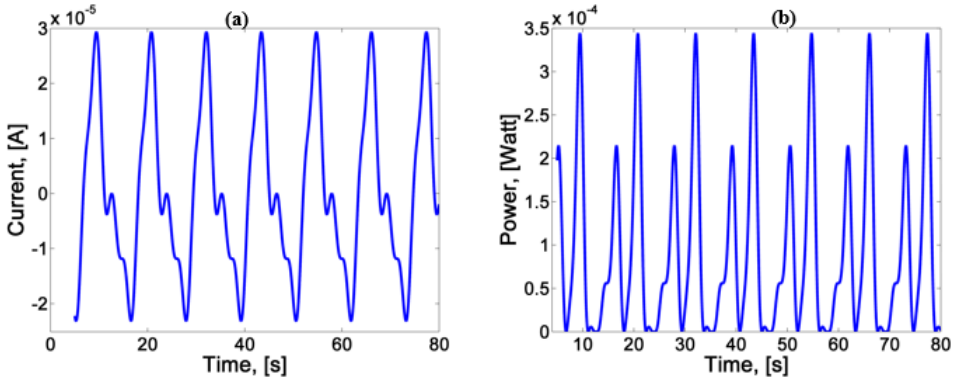

Figure 4.16: *The time traces for the linear case of the induced electrical current (a) and the harvester power output (b) with* $\omega = 7.85\ rad/s$; $R_{load} = 400\ k\Omega$.

Considering now the nonlinear Eqs. 4.37, we use the fourth order Runge-Kutta algorithm to solve the equations numerically. Fig. 4.17(a) presents a representative curve of the time trace of the membrane deflection. One observes the generation of bursting oscillations with frequency monitored by that of the blood pressure. Fig. 4.17(b) presents the corresponding phase portrait. The same behaviour appears for the induced current Fig. 4.17(c) and the smaller peak of the power Fig. 4.17(d) is reduced as compare to that of the higher peak.

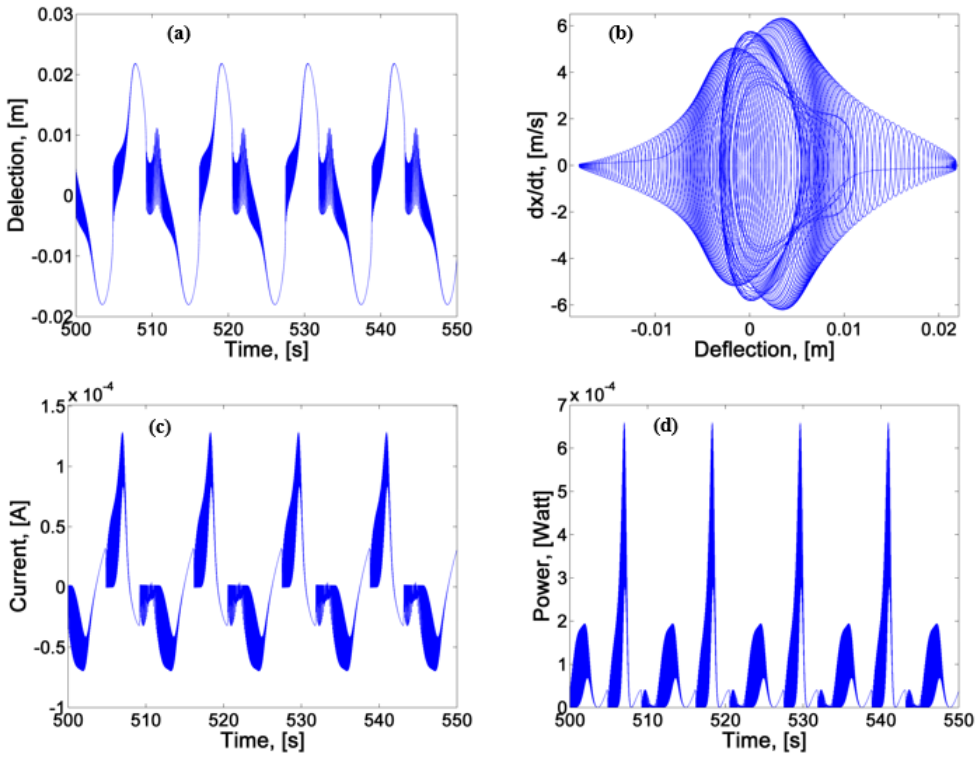

Figure 4.17: *Time traces, for the nonlinear case, of the one electrode deflection (a), phase portrait of the arterial deflection (b), the induced electrical current (c) and the harvester power output (d), by using the numerical simulation* $\omega = 7.85\ rad/s$; $R_{load} = 40\ k\Omega$.

In terms of frequency, Fig. 4.18 shows the variation of the output power as the frequency varies. It is seen that the power increases with the frequency and saturates to an almost constant value. This means that if the heartbeat frequency increases, the power generated by the harvester increases. However, after the heartbeat frequency has reached a limiting critical value, the power generated by the harvester remains constant.

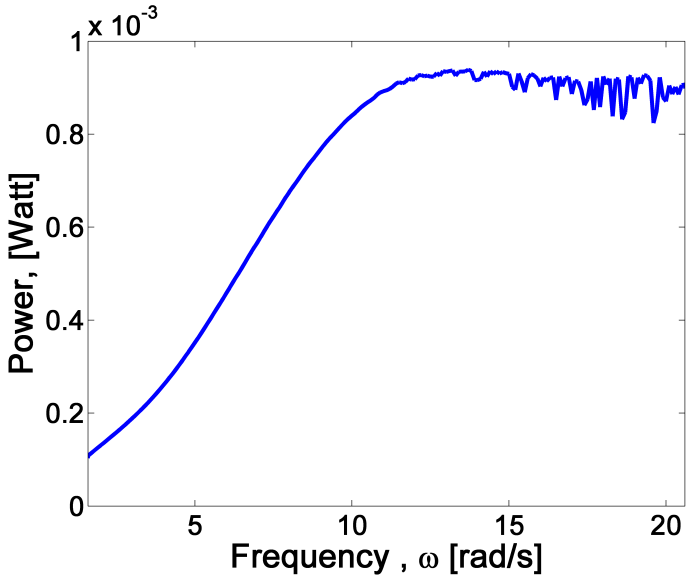

Figure 4.18: *Output power for $R_{load} = 40\ k\Omega$ versus the frequency of the blood pressure.*

Now considering how the power varies with the resistive load, Fig. 4.19 shows that the power increases with R_{load} till a value of about $R_{load} = 40\ k\Omega$ at which a maximal value is attained. After this value, the power decreases when the resistance increases. The maximal value of the generated power is $P_{\max} = 0.47\ mW$.

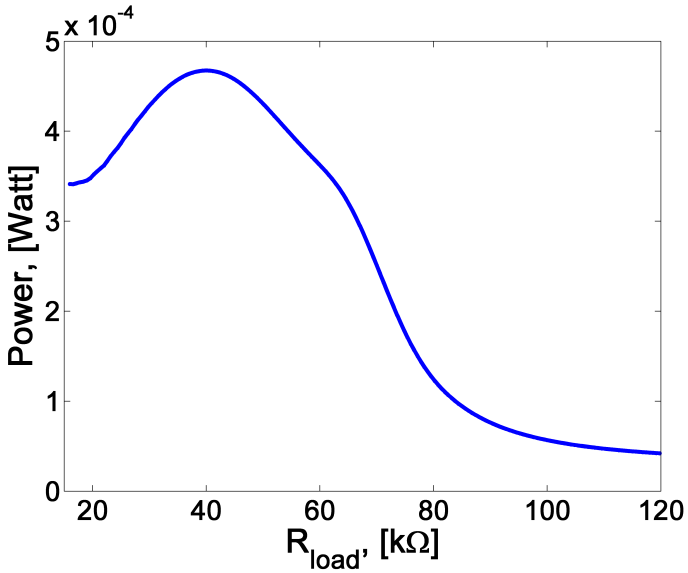

Figure 4.19: *Harvested power with respect to the resistive load for $\omega = 7.85\ rad/s$ and with others parameters of Table. 4.3 and Table. 4.4.*

4.4.3 Case of random process noise excitation

If one take into account the inter molecular agitation, and the physiological behaviour of human body, then the effects of parasympathetic and sympathetic innervation of the heart will produce random pulsating frequency pressure with the constant amplitude ranging from 28 beats per minute up to 200 beats per minute. A randomly varying pneumatic neck chamber stimulates the baroreceptors measuring the arterial blood pressure, whereas the venous baroreceptor is periodically stimulated by an oscillating tilt angle. The neuronal signals from these receptors are independently transmitted to the brain stem, which controls the heart rate and width of the blood vessels; after [99]. In this conditional state, the behaviour of the e-VEH under bounded noise could be investigate.
A harmonic function with constant amplitude and random frequency and phases is called bounded noise, which can be expressed by mathematical presentation as [100]

$$\xi(t) = \sigma \cos(\Omega t + \psi), \quad \psi = \delta B(t) + \Gamma, \tag{4.45}$$

where Ω and δ are positive constants, $B(t)$ is a standard Wiener process, Γ is a random variable uniformly distribution in $[0, 2\pi]$. $\xi(t)$ is a stationary random process in wide sense with zero mean. Its covariance function is

$$C_\xi(\tau) = \frac{\sigma^2}{2} \exp\left(-\frac{\delta^2 |\tau|}{2}\right) \cos(\Omega\tau) \tag{4.46}$$

and its spectral density is

$$S_\xi(\omega) = \frac{(\sigma\delta)^2}{2\pi} \left(\frac{1}{4(\omega - \Omega)^2 + \delta^2} + \frac{1}{4(\omega + \Omega)^2 + \delta^2}\right) \tag{4.47}$$

The variance of the bounded noise is

$$C(0) = \frac{\sigma^2}{2} \tag{4.48}$$

which implies that the bounded noise has finite power. The shape of spectral density depends on Ω and δ, while the bandwidth of the bounded noise mainly depends on δ. It is a narrow-band process when δ is small. This bounded noise

can be written as

$$\begin{aligned} &\xi(t) = \sigma\cos(\Omega t + \delta B(t) + \Gamma) = \sigma\cos\left(\varphi(t)\right) \\ &with \qquad\qquad \varphi(t) = \Omega t + \delta B(t) + \Gamma \\ &\qquad\qquad\quad \dot{\varphi}(t) = \Omega + \delta\dot{B}(t) = \Omega + \delta\zeta_n(t) \end{aligned} \tag{4.49}$$

Where $\zeta_n(t)$ is the distributed Gaussian white noise which is the derivate of the standard Wiener process respect to the time. The Kasdin algorithm [84] is used to generate the Gaussian white noise from random numbers which are uniformly distributed on the unit interval $[0, 1]$. Thus for each step Δt, the simulated set of the equation is as follows.

$$\begin{aligned} &\ddot{x} + \alpha\dot{x} + \beta x + \gamma x^3 - \eta\left[1 + (2q - x) + \left(x^2 - 2qx + q^2\right)\right] \\ &\qquad\qquad +\eta\left(x^3 - 2qx^2 + q^2x\right) = \sigma\cos\left(\varphi(t)\right) \\ &\dot{q} + \mu\left\{1 + \left(q - \tfrac{x}{\lambda_0}\right) + \tfrac{1}{\lambda_0}\left(\tfrac{1}{2}x^2 - qx\right) + \tfrac{1}{\lambda_0}\left(\tfrac{1}{2}qx^2 - \tfrac{1}{3}x^3\right)\right\} = 0 \\ &\dot{\varphi}(t) = \Omega + \delta\zeta_n(t) \end{aligned} \tag{4.50}$$

We now consider the response of the mechanism with stochastic forcing of the blood pressure on artery. The net integrated energy output from both cases is shown in Fig. 4.20.

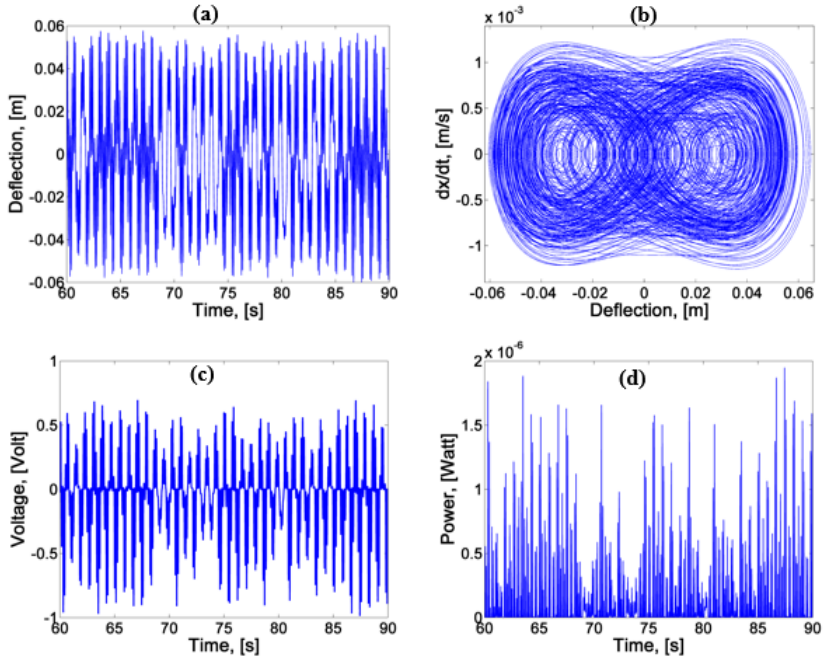

Figure 4.20: *Time trace of harvester model on stochastic excitation: (a) Electrodes deflection. (b) Phase Portrait. (c) Theoretical Voltage. (d) Maximum Power Harvested. When the exciting amplitude* $\sigma = 10.0\ P_a$ *at frequency* $\omega = 7.85\ rad/s$*, and noise amplitude* $\delta = 0.02$*.*

4.4.4 Electrostatic energy form cylindrical flexible pipes

In order to have a view on how the harvester will react if the harvester is used for other type of flexible pipes, an extension of the above study has been carried out. In this general case the equation of the motion is:

$$\begin{aligned} &\ddot{x} + \alpha\dot{x} + \beta x + \gamma x^3 - \eta\left[(2q - x) + \left(x^2 - 2qx + q^2\right) - \left(x^3 - 2qx^2 + q^2x\right)\right] \\ &\qquad = \Gamma * \sum_{r=1}^{4} \alpha_r \cos\left(r\Omega\tau\right) + \beta_r \sin\left(r\Omega\tau\right) \\ &\dot{q} + \mu\left\{\left(q - \tfrac{x}{\lambda_0}\right) + \tfrac{1}{\lambda_0}\left(\tfrac{1}{2}x^2 - qx\right) + \tfrac{1}{\lambda_0}\left(\tfrac{1}{2}qx^2 - \tfrac{1}{3}x^3\right)\right\} = 0 \end{aligned} \tag{4.51}$$

where Γ is multiplicative pressure coefficient. It is assumed that the mechanical excitation still has the shape of the pressure presented above in the case of blood pressure. However, its amplitude depends on the constant Γ. Moreover, frequency values out of the biological range have been considered. By varying Γ, Fig. 4.21 shows that the membrane deflection undergoes various bifurcations leading to different dynamical behaviours including chaos. Indeed, as Γ increases, different

transitions are captured: period doubling bifurcation, transition to bubbles sandwiched by symmetry breaking.

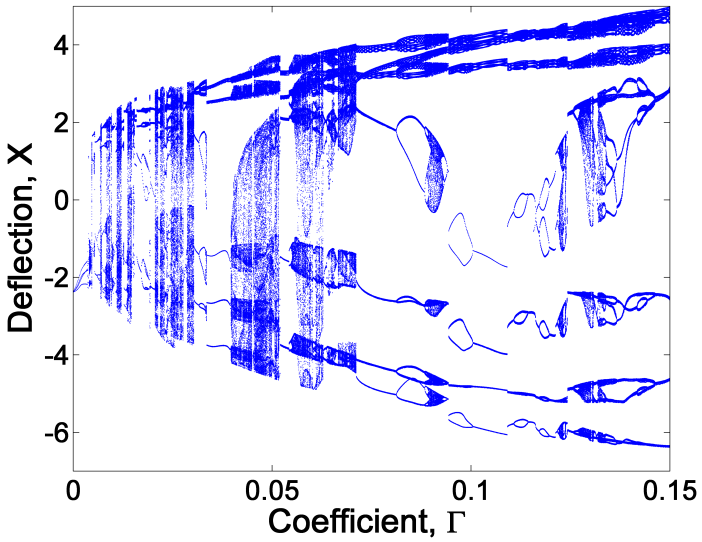

Figure 4.21: *Bifurcation diagram for* $\omega = 100.0$ *rad/s versus the amplitude* Γ.

4.5 Conclusion

In this chapter, we have investigated on electrostatic conversion of tree/beam vibration into electrical energy and extension to conversion of the arterial pulsating pressure. Frist, the power generated by an electrostatic energy harvester with variable area, variable permittivity has been analysed. The power generated by each configuration has been plotted in terms of appropriate parameters such as the frequency and value of the load resistance. Results show that the power increases almost linearly with the amplitude of excitation. It has appeared that the power increases with the permittivity ratio. We also included the case of variable radius and found that for different values of the initial radius, the power increases with the increase of the radius radio. We have also considered a cylindrical electrostatic energy harvester which converts the expansion and contraction of an artery (due to pulsatile blood pressure changes) into electrical energy. It has been found that the output power increases with the blood pressure frequency and attains a saturate limit at high blood pressure frequencies. The extension of the study to other

types of pulsating flows in flexible pipes has shown that the cylindrical energy harvester shows different bifurcation structures (including bifurcation to chaos) when the amplitude of the pressure increases. The device can find application in bioengineering to power artificial heart or artificial pacemakers. In this way, the artificial biological device directly responds to physiological activities.

General Conclusion

This thesis has been concerned with the **study of vibrations energy harvesters based on trees, cantilever beams, flexible tubes and variable geometric and physical parameters**. The vibration energy harvester in this thesis consists of two main techniques: electromagnetic transducer mechanism and electrostatic transducer mechanism.

Summary of the main results

The main results of the thesis can be given as follows:

– We have put in place energy harvesters which convert the trees vibration into electrical energy. They have been studied theoretically and experimentally on prototypes and in the field. A laboratory test has been conducted to demonstrate that harvesting energy from tree motion is possible. This was followed by a preliminary field investigation where we used a representative of tree inside the university campus to capture electric energy from tree motion. A pendulum electromechanical energy harvester excited by a periodic air flow taking into account the effects of spring constant and pendulum length has been studied. As it was observed in the experimental part, there were ranges of length and spring coefficient where the power increases. We demonstrated that: (i) by adding a spring constant in the system, its dynamics changes, and specific spring stiffness constant optimizes the energy harvesting, (ii) the choice of pendulum length also optimizes the energy harvesting.

– A new AC-DC amplifier was designed and studied. It used Schottky

diode and a voltage multiplier (octuplet) circuit for its optimum performance. Experimental results using an energy harvesting device made of a flexible beam undergoing electromagnetic transduction are obtained. The gain of the circuit increases with the amplitude of the input voltage, with the frequency of the input signal and the capacitances of the capacitors used. But the maximum gain was 8.

– An electrostatic vibration energy harvester (e-VEH) system with variable area, variable permittivity, and variable radius has been investigated. Nonlinear oscillator equations were established for each case, and solved analytically and numerically. The power produced by each configuration of the harvester was presented in terms of resistive load, frequency and external excitation. It comes that power generated by an electrostatic energy harvester with variable area, variable permittivity increased almost linearly with the amplitude of excitation. It appears that the power increases with permittivity ratio. We also found that for different values of the initial radius, the power increases with the increased of the radius radio.

– Next we have extended the electrostatic energy harvester to the conversion of a pulsating fluid pressure in elastic tubes into electrical energy using a cylindrical electrostatic vibration energy harvester attached to the tube. A special attention is paid on the case of blood flow in order to have energy that can be used to power artificial organs such as artificial pacemaker. The extension in the case of any other type of flexible pipe was done.

Future work

This thesis suggests several possible avenues of research that remain open for further exploration.

One part of this study focused on the design of an optimized electrostatic harvester using a variable area, permittivity and radius capacitor. However, ex-

perimental testing was not performed using the optimized capacitor model. Thus future research could move towards building and testing a harvester that follows the optimization results of this study.

Furthermore, we will study a network of energy harvesters fixed on a tree.

A challenge will be to harvest the required amount of energy such a situation, where the available trees are within a dense forest rather than a sparsely young Eucalypt tree treated in the field of investigation of this thesis.

In future work, we also plan to carry out experimental field tests with other types of trees and in other environments with different meteorological conditions.

Publication list of the PhD Candidate

- **Dianoré Tokoue Ngatcha**,Paul Woafo, **"Analysis of an electrostatic energy harvester with variable area, permittivity and radius"**. *Eur. Phys. J. B. 89*, 229 (2016). doi: 10.1140/epjb/e2016-70287-y; 11pp.

Bibliography

[1] A. Erturk and D. J. Inman, **"Introduction to Piezoelectric Energy Harvesting"**. in *Piezoelectric Energy Harvesting* Chichester, UK: John Wiley and Sons, Ltd, pp. 1-18, 2011.

[2] S. Beeby and W. Neil, **"Energy harvesting for autonomous systems"**. *Artech House*, 2010.

[3] S. Priya and D. J. Inman, Eds., **"Energy Harvesting Technologies"**. *Springer US* Boston, MA, 2009.

[4] S. Roundy, P. K. Wright, and J. M. Rabaey, **"Energy Scavenging for Wireless Sensor Networks"**. *Springer US* Boston, MA, 2004.

[5] J. Yick, B. Mukherjee, and D. Ghosal, **"Wireless sensor network survey"**. *Comput. Networks* , vol. 52, no. 12, pp. 2292-2330, 2008.

[6] W. Wang and O. A. Jianu, **"A Smart Sensing Unit for Vibration Measurement and Monitoring"**. *IEEE/ASME Trans. Mechatronics* vol. 15, no. 1, pp. 70-78, Feb. 2010.

[7] W. H. Liao, D. H. Wang, and S. L. Huang, **"Wireless Monitoring of Cable Tension of Cable-Stayed Bridges Using PVDF Piezoelectric Films"**. *J. Intell. Mater. Syst. Struct* vol. 12, no. 5, pp. 331-339, May 2001.

[8] J. M. Rabaey, M. J. Ammer, J. L. da Silva, D. Patel, and S. Roundy, **"PicoRodio supports ad hoc ultra-low power wireless networking"**, *Computer (Long. Beach. Calif)* vol. 33, no. 7, pp. 42-48, Jul. 2000.

[9] D. M. Doolin and N. Sitar, **Wireless sensors for wildfire monitoring**, p. 477, 2005.

[10] T. Wark et al, **"Springbrook: Challenges in developing a long-term, rainforest wireless sensor network"**. in *International Conference on Intelligent Sensors, Sensor Networks and Information Processing* pp. 599-604, 2008.

[11] A.-J. Garcia-Sanchez et al, **"Wireless Sensor Network Deployment for Monitoring Wildlife Passages"**. *Sensors* vol. 10, no. 8, pp. 7236-7262, Aug. 2010.

[12] S. McGarry and C. Knight, **"The Potential for Harvesting Energy from the Movement of Trees"**. *Sensors* vol. 11, no. 12, pp. 9275-9299, Sep. 2011.

[13] S. McGarry and C. Knight, **"Development and Successful Application of a Tree Movement Energy Harvesting Device, to Power a Wireless Sensor Node"**. *Sensors* vol. 12, no. 12, pp. 12110-12125, Sep. 2012.

[14] F. Fei, S. Zhou, J. Mai, and W. Li, **"Development of an Indoor Airflow Energy Harvesting System for Building Environment Monitoring"**. *Energies* vol. 7, no. 5, pp. 2985-3003, May 2014.

[15] F. Fei, J. D. Mai, and W. J. Li, **"A wind-flutter energy converter for powering wireless sensors"**. *Sensors Actuators A Phys* , vol. 173, no. 1, pp. 163-171, 2012.

[16] C. A. Kitio Kwuimy, G. Litak, M. Borowiec, and C. Nataraj, **"Performance of a piezoelectric energy harvester driven by air flow"**, *Appl. Phys. Lett.*, vol. 100, no. 2, p. 24103, Jan. 2012.

[17] I. Iliuk et al., **"A non-ideal portal frame energy harvester controlled using a pendulum"**, *Eur. Phys. J. Spec. Top.*, vol. 222, no. 7, pp. 1575-1586, Sep. 2013.

[18] J. W. Matiko, N. J. Grabham, S. P. Beeby, and M. J. Tudor, **"Review of the application of energy harvesting in buildings"**, *Meas. Sci. Technol.*, vol. 25, no. 1, p. 12002, Jan. 2014.

[19] A. N. Kadjie and P. Woafo, **"Effects of springs on a pendulum electromechanical energy harvester"**, *Theor. Appl. Mech. Lett.*, vol. 4, no. 6, p. 63001, 2014.

[20] E. Yildirim and H. Külah, **"Electrostatic energy harvesting by droplet-based multi-phase microfluidics"**, *Microfluid. Nanofluidics*, vol. 13, no. 1, pp. 107-111, Jul. 2012.

[21] A. Dudka, P. Basset, F. Cottone, E. Blokhina, and D. Galayko, **"Wideband Electrostatic Vibration Energy Harvester (e-VEH) Having a Low Start-Up Voltage Employing a High-Voltage Integrated Interface"**, *J. Phys. Conf. Ser.*, vol. 476, no. 1, p. 12127, Dec. 2013.

[22] P. Basset et al., **"Electrostatic vibration energy harvester with combined effect of electrical nonlinearities and mechanical impact"**, *J. Micromechanics Microengineering*, vol. 24, no. 3, p. 35001, Mar. 2014.

[23] S. Roundy et al., **"Improving Power Output for Vibration-Based Energy Scavengers"**, *IEEE Pervasive Comput.*, vol. 4, no. 1, pp. 28-36, Jan. 2005.

[24] N. S. Shenck and J. A. Paradiso, **"Energy scavenging with shoe-mounted piezoelectrics"**, *IEEE Micro*, vol. 21, no. 3, pp. 30-42, 2001.

[25] D. Guyomar, A. Badel, E. Lefeuvre, and C. Richard, **"Toward energy harvesting using active materials and conversion improvement by nonlinear processing"**, *IEEE Trans. Ultrason. Ferroelectr. Freq. Control*, vol. 52, no. 4, pp. 584-595, Apr. 2005.

[26] P. Glynne-Jones, S. P. Beeby, and N. M. White, **"Towards a piezoelectric vibration-powered microgenerator"**, *IEE Proc. - Sci. Meas. Technol.*, vol. 148, no. 2, p. 68, 2001.

[27] E. Lefeuvre, A. Badel, C. Richard, L. Petit, and D. Guyomar, **"A comparison between several vibration-powered piezoelectric generators for standalone systems"**, *Sensors Actuators A Phys.*, vol. 126, no. 2, pp. 405-416, 2006.

[28] N. E. Dutoit and B. L. Wardle, **"performance of microfabricated piezoelectric vibration energy harvesters"**, *Integr. Ferroelectr.*, vol. 83, no. 1, pp. 13-32, Nov. 2006.

[29] A. Erturk et al., **"An experimentally validated bimorph cantilever model for piezoelectric energy harvesting from base excitations"**, *Smart Mater. Struct.*, vol. 18, no. 2, p. 25009, Feb. 2009.

[30] S. Roundy et al., **"A piezoelectric vibration based generator for wireless electronics"**, *Smart Mater. Struct.*, vol. 13, no. 5, pp. 1131-1142, Oct. 2004.

[31] P. D. Mitcheson, P. Miao, B. H. Stark, E. M. Yeatman, A. S. Holmes, and T. C. Green, **"MEMS electrostatic micropower generator for low frequency operation"**, *Sensors Actuators A Phys.*, vol. 115, no. 2, pp. 523-529, 2004.

[32] S. Meninger, J. O. Mur-Miranda, R. Amirtharajah, A. Chandrakasan, and J. H. Lang, **"Vibration-to-electric energy conversion"**, *IEEE Trans. Very Large Scale Integr. Syst.*, vol. 9, no. 1, pp. 64-76, Feb. 2001.

[33] F. Peano and T. Tambosso, **"Design and optimization of a MEMS electret-based capacitive energy scavenger"**, *J. Microelectromechanical Syst.*, vol. 14, no. 3, pp. 429-435, Jun. 2005.

[34] T. Sterken, P. Fiorini, K. Baert, R. Puers, and G. Borghs, **"An electret-based electrostatic microgenerator"**, in *Transducers'03. 12th International Conference on Solid-State Sensors, Actuators and Microsystems.* Digest of Technical Papers (Cat. No.03TH8664), vol. 2, pp. 1291-1294.

[35] S. Roundy, P. K. Wright, and J. Rabaey, **"A study of low level vibrations as a power source for wireless sensor nodes"**, *Comput. Commun.*, vol. 26, no. 11, pp. 1131-1144, 2003.

[36] L. G. W. Tvedt, D. S. Nguyen, and E. Halvorsen, **"Nonlinear Behavior of an Electrostatic Energy Harvester Under Wide- and Narrowband**

Excitation", *J. Microelectromechanical Syst.*, vol. 19, no. 2, pp. 305-316, Apr. 2010.

[37] H. Kulah and K. Najafi, **"An electromagnetic micro power generator for low-frequency environmental vibrations"**,in *17th IEEE International Conference on Micro Electro Mechanical Systems.* Maastricht MEMS Technical Digest, pp. 237-240, 2004.

[38] P. Glynne-Jones, M. J. Tudor, S. P. Beeby, and N. M. White, **"An electromagnetic, vibration-powered generator for intelligent sensor systems"**, *Sensors Actuators A Phys.*, vol. 110, no. 1, pp. 344-349, 2004.

[39] J. M. H. Lee, S. C. L. Yuen, W. J. Li, and P. H. W. Leong, **"Development of an AA size energy transducer with micro resonators"**,in *Proceedings of the 2003 International Symposium on Circuits and Systems, ISCAS - 03.*, vol. 4, p. IV-876-IV-879, 2003.

[40] R. Amirtharajah and A. P. Chandrakasan, **"Self-powered signal processing using vibration-based power generation"**, *IEEE J. Solid-State Circuits*, vol. 33, no. 5, pp. 687-695, May 1998.

[41] S. P. Beeby et al., **"Energy harvesting vibration sources for microsystems applications"**, *Meas. Sci. Technol.*, vol. 17, no. 12, pp. R175-R195, Dec. 2006.

[42] C. B. Williams and R. B. Yates, **"Analysis of a micro-electric generator for microsystems"**, *Sensors Actuators A Phys.*, vol. 52, no. 1-3, pp. 8-11, Mar. 1996.

[43] N. G. Elvin and A. A. Elvin, **"An experimentally validated electromagnetic energy harvester"**, *J. Sound Vib.*, vol. 330, no. 10, pp. 2314-2324, 2011.

[44] S. Dong, J. Zhai, J. F. Li, D. Viehland, and S. Priya, **"Multimodal system for harvesting magnetic and mechanical energy"**, *Appl. Phys. Lett.*, vol. 93, no. 10, p. 103511, Sep. 2008.

[45] L. Wang et al., **"Vibration energy harvesting by magnetostrictive material"**, *Smart Mater. Struct.*, vol. 17, no. 4, p. 45009, Aug. 2008.

[46] S. Mohammadi and A. Esfandiari, **"Magnetostrictive vibration energy harvesting using strain energy method"**, *Energy*, vol. 81, pp. 519-525, 2015.

[47] H. Baudry, **"Screen Printing Piezoelectric Devices"**, *Microelectron. Int.*, vol. 4, no. 3, pp. 71-74, Mar. 1987.

[48] N. M. White et al., **"Thick-film sensors: past, present and future"**, *Meas. Sci. Technol.*, vol. 8, no. 1, pp. 1-20, Jan. 1997.

[49] A. J. Lovinger, **"Ferroelectric Polymers"**, *Science (80).*, vol. 220, no. 4602, 1983.

[50] N. E. Dutoit, B. L. Wardle, and S.-G. KIM, **"Design considerations for mems-scale piezoelectric mechanical vibration energy harvesters"**, *Integr. Ferroelectr.*, vol. 71, no. 1, pp. 121-160, Jul. 2005.

[51] S. Roundy, P. K. Wright, and K. S. J. Pister, **"Micro-Electrostatic Vibration-to-Electricity Converters"**,in *Microelectromechanical Systems*, 2002, vol. 2002, pp. 487-496.

[52] S. J. Roundy, **"Energy Scavenging for Wireless Sensor Nodes with a Focus on Vibration to Electricity Conversion"**, *University of California, Berkeley*, 2003.

[53] P. Basset, D. Galayko, A. M. Paracha, F. Marty, A. Dudka, and T. Bourouina, **"A batch-fabricated and electret-free silicon electrostatic vibration energy harvester"**, *J. Micromechanics Microengineering*, vol. 19, no. 11, p. 115025, Nov. 2009.

[54] D. Hoffmann, B. Folkmer, and Y. Manoli, **"Fabrication, characterization and modelling of electrostatic micro-generators"**, *J. Micromechanics Microengineering*, vol. 19, no. 9, p. 94001, Sep. 2009.

[55] D. S. Nguyen, E. Halvorsen, G. U. Jensen, and A. Vogl, **"Fabrication and characterization of a wideband MEMS energy harvester utilizing nonlinear springs"**, *J. Micromechanics Microengineering*, vol. 20, no. 12, p. 125009, Dec. 2010.

[56] L. Wang and F. G. Yuan, **"Energy harvesting by magnetostrictive material (MsM) for powering wireless sensors in SHM"**, p. 652941, 2007.

[57] X. Dai, Y. Wen, P. Li, J. Yang, and G. Zhang, **"Modeling, characterization and fabrication of vibration energy harvester using Terfenol-D/PZT/Terfenol-D composite transducer"**, *Sensors Actuators A Phys.*, vol. 156, no. 2, pp. 350-358, 2009.

[58] P. D. Mitcheson, T. C. Green, and E. M. Yeatman, **"Power processing circuits for electromagnetic, electrostatic and piezoelectric inertial energy scavengers"**, *Microsyst. Technol.*, vol. 13, no. 11-12, pp. 1629-1635, May 2007.

[59] A. D. Nath, K. Radhakrishnan, and E. K. A, **"Low-Voltage Direct AC-DC Boost Converter for Microgenerator Based Energy Harvesting"**, *ISSN Int. J. Adv. Res. Electr. Electron. Instrum. Eng.*, vol. 2, no. 3, pp. 2320-3765, 2013.

[60] R. Dayal, S. Dwari, and L. Parsa, **"Design and Implementation of a Direct AC-DC Boost Converter for Low-Voltage Energy Harvesting"**, *IEEE Trans. Ind. Electron.*, vol. 58, no. 6, pp. 2387-2396, Jun. 2011.

[61] G. D. Szarka, P. P. Proynov, B. H. Stark, S. G. Burrow, and N. McNeill, **"International Symposium on Low Power Electronics and Design: Fukuoka, Japan, August 1-3, 2011"**, *IEEE Press*, 2011.

[62] S. Dwari and L. Parsa, **"An Efficient AC-DC Step-Up Converter for Low-Voltage Energy Harvesting"**, *IEEE Trans. Power Electron.*, vol. 25, no. 8, pp. 2188-2199, Aug. 2010.

[63] G. K. Ottman, H. F. Hofmann, and G. A. Lesieutre, **"Optimized piezoelectric energy harvesting circuit using step-down converter in dis-**

continuous conduction mode", *IEEE Trans.* Power Electron., vol. 18, no. 2, pp. 696-703, Mar. 2003.

[64] S. Cheng, R. Sathe, R. D. Natarajan, and D. P. Arnold, **"A Voltage-Multiplying Self-Powered AC/DC Converter with 0.35-V Minimum Input Voltage for Energy Harvesting Applications"**, *IEEE Trans. Power Electron.*, vol. 26, no. 9, pp. 2542-2549, Sep. 2011.

[65] B. H. Stark, P. D. Mitcheson, Peng Miao, T. C. Green, E. M. Yeatman, and A. S. Holmes, **"Converter circuit design, semiconductor device selection and analysis of parasitics for micropower electrostatic Generators"**, *IEEE Trans. Power Electron.*, vol. 21, no. 1, pp. 27-37, Jan. 2006.

[66] S. Xu, K. D. T. Ngo, T. Nishida, G.-B. Chung, and A. Sharma, **"Low Frequency Pulsed Resonant Converter for Energy Harvesting"**, *IEEE Trans. Power Electron.*, vol. 22, no. 1, pp. 63-68, Jan. 2007.

[67] E. Lefeuvre, D. Audigier, C. Richard, and D. Guyomar, **"Buck-Boost Converter for Sensorless Power Optimization of Piezoelectric Energy Harvester"**, *IEEE Trans. Power Electron.*, vol. 22, no. 5, pp. 2018-2025, Sep. 2007.

[68] S. Dwari, R. Dayal, and L. Parsa, **"A Novel direct AC/DC converter for efficient low voltage energy harvesting"**, in *34th Annual Conference of IEEE Industrial Electronics*, pp. 484-488, 2008.

[69] S. Boisseau, G. Despesse, and B. A. Seddik, **"Electrostatic Conversion for Vibration Energy Harvesting"**, Oct. 2012.

[70] S. R. Anton et al., **"A review of power harvesting using piezoelectric materials (2003-2006)"**, *Smart Mater. Struct.*, vol. 16, no. 3, pp. R1-R21, Jun. 2007.

[71] X.-F. He and J. Gao, **"Wind energy harvesting based on flow-induced-vibration and impact"**, *Microelectron. Eng.*, vol. 111, pp. 82-86, 2013.

[72] C. Himes, E. Carlson, R. J. Ricchiuti, B. P. Otis, and B. A. Parviz, **"Ultralow Voltage Nanoelectronics Powered Directly, and Solely, From a Tree"**, *IEEE Trans. Nanotechnol.*, vol. 9, no. 1, pp. 2-5, Jan. 2010.

[73] G. Taylor, **"Analysis of the Swimming of Long and Narrow Animals"**, *Proc. R. Soc. London A Math. Phys. Eng. Sci.*, vol. 214, no. 1117, 1952.

[74] R. D. Blevins and R. D., **"Flow-induced vibration"**, *New York, Van Nostrand Reinhold Co.*, 1977. 377 p., 1977.

[75] A. Kurs, A. Karalis, R. Moffatt, J. D. Joannopoulos, P. Fisher, and M. Soljacic, **"Wireless Power Transfer via Strongly Coupled Magnetic Resonances"**, *Science*, vol. 317, no. 5834, 2007.

[76] A. Karalis, J. D. Joannopoulos, and M. Soljacic, **"Efficient wireless non-radiative mid-range energy transfer"**, *Ann. Phys. (N. Y).*, vol. 323, no. 1, pp. 34-48, 2008.

[77] J. A. Paradiso and T. Starner, **"Energy Scavenging for Mobile and Wireless Electronics"**, *IEEE Pervasive Comput.*, vol. 4, no. 1, pp. 18-27, Jan. 2005.

[78] A. H. Nayfeh and D. T. Mook, **"Nonlinear oscillations."**, *Wiley.*, 1979.

[79] C. Hayashi, **"Nonlinear Oscillations in physical systems"**, *New York: Mc-Graw-Hill*, 1964.

[80] W. H. Press, S. A. Teukolsky, W. T. Vetterling, and B. P. Flannery, **"Numerical Recipes: The Art of Scientic Computing"**, *Cambridge univ. press.*, 1982.

[81] J. D. Hoffman and S. Frankel, **"Numerical Methods for Engineers and Scientists"**, *Marcel Dek. New-York*, 2001.

[82] Y. K. Lin and G. Q. Cai, **"Probabilistic structural dynamics: advanced theory and applications"**, *McGraw-Hil. New York*, 1995.

[83] M. San Miguel and R. Toral, **"Stochastic Effects in Physical Systems"**, *Springer Netherlands*, pp. 35-127, 2000.

[84] N. J. Kasdin, **"Runge-Kutta Algorithm for the Numerical Integration of Stochastic Differential Equations"**, *J. Guid. Control. Dyn.*, vol. 18, no. 1, pp. 114-120, Jan. 1995.

[85] N. Manfoumbi, F. Dubois, and N. Sauvat, **"Comportement mécanique différé des essences tropicales en ambiances tropicales: Expérimentation et cadre règlementaire"**, 2011.

[86] S. Timoshenko, **"Théorie de la Stabilité Elastique"**, *Dunod. Paris*, 1966.

[87] M. F. White, **"Fluid Mechanics"**, *4th editio. Rhode Island*, 1998.

[88] G. T. O. Tékam, E. B. T. Tchuisseu, C. A. K. Kwuimy, and P. Woafo, **"Analysis of an electromechanical energy harvester system with geometric and ferroresonant nonlinearities"**, *Nonlinear Dyn.*, vol. 76, no. 2, pp. 1561-1568, Apr. 2014.

[89] A. M. Hawkes, A. R. Katko, and S. A. Cummer, **"A microwave metamaterial with integrated power harvesting functionality"**, *Appl. Phys. Lett.*, vol. 103, no. 16, pp. 0-3, 2013.

[90] M. Mizuno and D. G. Chetwynd, **"Investigation of a resonance microgenerator"**, *J. Micromechanics Microengineering*, vol. 13, no. 2, pp. 209-216, Mar. 2003.

[91] P. Lorrain and D. Corson, **"Electromagnetic Fields and Waves"**, *2nd ed. Fr. San Francisco*, 1970.

[92] E. M. Purcell, **"Electricity and magnetism"**, *McGraw-Hil. New York*, 1965.

[93] J. W. H., **"Engineering Electromagnetics"**, *McGraw-Hil. New York*, 1981.

[94] L. Eyges, **"The classical Electromagnetic Field"**, *Addison-We. MA*, 1972.

[95] I. J. Busch-Vishniac, **"Transduction Based on Changes in the Energy Stored in an Electric Field"**, *Springer New York*, pp. 59-99, 1999.

[96] J. A. Potkay and K. Brooks, **"An Arterial Cuff Energy Scavenger For Implanted Microsystems"**, in *2008 2nd International Conference on Bioinformatics and Biomedical Engineering*, pp. 1580-1583, 2008.

[97] B. Wiwatanapataphee, D. Poltem, Y. H. Wu, and Y. Lenbury, **"Simulation of pulsatile flow of blood in stenosed coronary artery bypass with graft."**, *Math. Biosci. Eng.*, vol. 3, no. 2, pp. 371-83, Apr. 2006.

[98] A. Kamura, T. Kawasaki, N. Koga, T. Inoue, and K. Node, **"Fracture of a sirolimus-eluting stent with migration"**, 2008.

[99] I. Hidaka, D. Nozaki, and Y. Yamamoto, **"Functional Stochastic Resonance in the Human Brain: Noise Induced Sensitization of Baroreflex System"**, *Phys. Rev. Lett.*, vol. 85, no. 17, pp. 3740-3743, Oct. 2000.

[100] W. Y. Liu, W. Q. Zhu, and Z. L. Huang, **"Effect of bounded noise on chaotic motion of duffing oscillator under parametric excitation"**, *Chaos, Solitons and Fractals*, vol. 12, no. 3, pp. 527-537, 2001.

[101] K. Joon Kim, F. Cottone, S. Goyal, and J. Punch, **"Energy scavenging for energy efficiency in networks and applications"**, *Bell Labs Tech. J.*, vol. 15, no. 2, pp. 7-29, Aug. 2010.

Eur. Phys. J. B (2016) 89: 229
DOI: 10.1140/epjb/e2016-70287-y

THE EUROPEAN PHYSICAL JOURNAL B

Regular Article

Analysis of an electrostatic energy harvester with variable area, permittivity and radius

Dianoré Tokoue Ngatcha[1] and Paul Woafo[1,2,a]

[1] Laboratory of Modelling and Simulation in Engineering, Biomimetics, and Prototypes and TWAS Research Unit, Faculty of Sciences, University of Yaounde I, P.O. Box 812, Yaounde, Cameroon
[2] Applied Physics Research Group (APHY), Vrije Universiteit Brussel, Pleinlaan 2, 1050 Brussels, Belgium

Received 9 May 2016 / Received in final form 1 July 2016
Published online 24 October 2016 –

Abstract. This paper reports on an electrostatic vibration energy harvester (e-VEH) system with variable area, variable permittivity, and variable radius. Nonlinear oscillator equations are established for each case, and solved analytically and numerically. The power produced by each configuration of the harvester is presented in terms of resistive load, frequency and external excitation.

1 Introduction

The process of capturing the energy from a system environment or surrounding and converting it into usable electrical energy is termed as energy harvesting. Vibration energy harvesters (VEHs) catch mechanical energy through a spring-mass system and then convert the largest possible fraction of this energy into electrical power.

One alternative means of generating energy for miniaturized systems is to utilize environmental sources such as heat, light, or vibration. Among these, vibration is a common environmental source due to its abundance. Vibration-based energy harvesters reported in the literature rely on electromagnetic [1–4], piezoelectric [5–13] or electrostatic [14–21] methods to convert mechanical energy of vibration of solid bodies or flexible materials to electrical energy.

VEHs with electrostatic transduction (e-VEH) display interesting features that differentiate them from other transduction mechanisms. They are particularly suitable for fabrication using silicon-based microelectromechanical systems (MEMS) technologies through a full batch fabrication process [22–24].

Most electrostatically actuated MEMS consist of an elastic plate suspended over a stationary rigid plate. The plates and the dielectric material filling the gap between them are conductive. An applied electric voltage between the two plates results in the deflection of the elastic plate, and a consequent change in the MEMS capacitance. The use of electrostatic micro-actuators is significantly limited by the pull-in instability [25]. This means that the applied electrostatic voltage has an upper limit, beyond which the electrostatic Coulomb force is not balanced by the elastic restoring force in the deformable plate, causing the two plates to snap together and the MEMS collapse. This pull-in instability was simultaneously observed experimentally by Taylor [26] and Nathanson et al. [27]. More refined linear and nonlinear models have been studied in the literature. Bai et al. [28] presented a preliminary work on an investigation of a nonlinear air-flow energy harvester integrating magnets and a piezoelectric cantilever array. Zhang et al. [29] suggested a model for energy harvesting from a rotating automotive tyre in which the principle of stochastic resonance was advantageously exploited. Batra et al. [30] investigated the effect of the ellipse aspect ratio on the pull-in instability of the electrostatic MEMS.

Yildiring and Külah [31] proposed an electrostatic energy harvesting technique utilizing droplet- based micro flow for continuous power generation. A study by Dudka et al. [32] focused on the architecture of a wideband electrostatic vibration energy harvester with a low start-up voltage and employing a high-voltage integrated interface. Recently, Basset et al. [33] presented an advanced study of an electrostatic vibration energy harvester with combined effects of electrical nonlinearities and mechanical impact. Their study included the design, characterization and theoretical analysis of a capacitive vibration energy harvester based on a resonant electromechanical device.

Fundamentally, electrostatic energy harvesters harness the work ambient vibrations exert on the electrostatic force of a variable capacitor. In more physical terms, vibrations cause the gap distance and/or overlap area of a parallel-plate capacitor to vary with a net effect [34], under constant charge or voltage conditions, of producing electrical energy [35]. Torres and Rincón-Mora [36] proposed and prototyped a circuit which indicates experimentally

[a] e-mail: pwoafo1@yahoo.fr

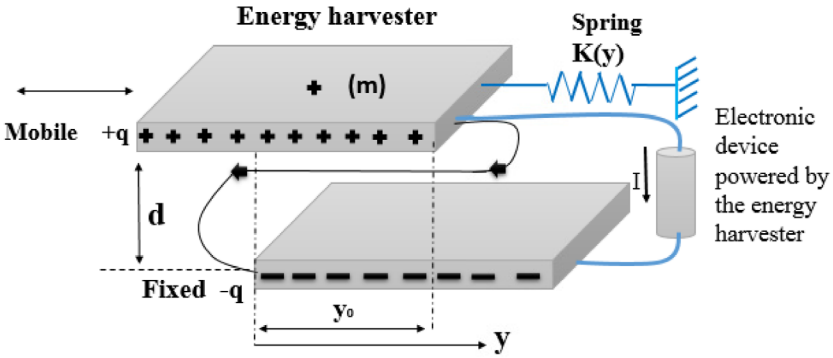

Fig. 1. Energy harvester capacitive transducer in which the effective area varies dynamically.

that harvesting energy electrostatically from vibrations is possible. Kempitiya et al. [37] proposed a low-power energy harvesting circuit that performs synchronous energy conversion on a triplate variable capacitor to improve the maximum achievable output power. Also, reference [22] presents a novel silicon-based and batch-processed MEMS electrostatic transducer for harvesting and converting the energy of vibrations into electrical energy without using an electret layer. Nguyen et al. [38] validated lumped models of an asymmetric bistable MEMS electrostatic energy harvester against measurements. The analysis of the effects of mistuning of natural frequencies and that of the coupling in a multiple pendulums energy harvester were conducted by Malaji and Ali [39].

The transduction mechanisms discussed above involve the variation of the distance or gap between the electrodes of a parallel plate capacitor, all parameters remaining fixed. Additional research has been undertaken recently which considers the variation of other parameters. Naruse et al. [40] developed a micro power generator technology consisting of micro-ball bearings which roll with the separation gap control and keep the separation gap firm, and they proposed a new electret structure to accommodate miniaturization. Le and Halvorsen [41] presented two microelectromechanical electrostatic energy harvester prototypes which take into account the end-stop effects under large amplitude displacement excitation. Galchev et al. [42] investigated the design, fabrication, and testing of a springless proximity inertial harvester that uses a suspension-less spherical inertial mass to capture multi-axial motion from the environment. Their transducers were variable-gap electrostatic harvester cells and the proof mass, which was a magnet, could then transfer energy to an array of underlying transducer cells through magnetic coupling.

In this study, electrostatic energy harvesters with variable area and permittivity and those with cylindrical configuration are considered.

The remainder of the paper is organized as follows. In Section 2, we present an energy harvester with variable area and permittivity in parallel plate configuration. The governing equations are solved analytically and numerically. Results obtained from the numerical simulation and analytical methods are presented and compared. In Section 3, the energy harvester with cylindrical configuration is investigated. Our conclusion is given in Section 4.

2 Energy harvester with variable area and permittivity in parallel plate configuration

The transduction mechanisms discussed in the literature involves changing the capacitance of a parallel plate capacitor by modifying the distance between the electrodes, all other parameters remaining fixed. Let us consider the basic definition of the capacitance as $C = \varepsilon A/d$, where ε is the permittivity, A is the effective area and d is the distance between the electrodes. It is clear that three parameters can be varied to change the capacitance. Let us now consider what would happen if we chose to vary A or ε in order to produce a variable transducer instead of varying the distance d between the electrodes.

2.1 Energy harvesters with variable area

First consider a capacitor in which the area A varies. The effective area can be changed by allowing one of the plates to move orthogonally to the direction of the electric field. Then the effective area of the capacitor is given by the area in which the two plates overlap. A schematic representation of the device studied is shown in Figure 1.

The operation of Figure 1 can be described as a microactuator modelled as a parallel- plates capacitor consisting of a movable top plate and a fixed bottom plate. The mobile plate is attached to a spring of variable constant $K(y)$. When an external sinusoidal force $f_0 \cos(\omega t)$ is applied on the upper plate, an electrostatic force is induced on the moveable plate.

Let us consider R, I, q, y, and $V = q/C$ as the load resistance, the induced current, charge, plate displacement, and actuation voltage respectively. We assume that (i) both plates are perfect conductors, and are separated by a dielectric layer of permittivity $\varepsilon = \varepsilon_0 \varepsilon_r$ where $\varepsilon_r = 1$ is the air relative permittivity, (ii) the plates are maintained at a fixed separation distance, (iii) the bottom plate is rigid and fixed, while the top one moves parallel to plate surface, and (iv) a potential difference $V = e$ exists between the two plates.

Using the principles of mechanics and electricity, one can establish that the harvester is described by the following set of equations

$$m\ddot{Y} + a\dot{Y} + bY + cY^3 - \frac{Q^2 d}{2\varepsilon_0 w Y^2} = f_0 \cos(\omega t)$$
$$R\dot{Q} + \frac{Q}{C} = 0 \qquad \text{with} \qquad C = \frac{\varepsilon w Y}{d} \tag{1}$$

where w is the width of the plates and Y is the displacement along which they overlap. m, a, b, and c are respectively the mass of the moveable upper electrode, the damping coefficient, the linear and nonlinear elastic constants of the spring.

Let us write the motion (lateral position) of the moving plate and the electric charge in the following manner:

$$Y = y_0 + \hat{y}$$
$$Q = q_0 + \hat{q} \tag{2}$$

where y_0 and q_0 are the initial values of the displacement and charge. Then, in the dimensionless form, the electromechanical system is governed by the set of equations rewritten as:

$$\ddot{y} + \alpha\dot{y} + \beta y + \gamma y^3 - \eta\left[1 + 2(q-y) + \left(q^2 - 4qy + 3y^2\right) + \left(6qy^2 - 2q^2 y - 4y^3\right)\right] = F_0 \cos(\Omega\tau)$$
$$\dot{q} + \mu\left[1 + (q-y) + \left(y^2 - qy\right) + \left(qy^2 - y^3\right)\right] = 0 \tag{3}$$

where we assume that $|\hat{q}|$ and $|\hat{y}|$ are small, and therefore higher order terms more than $\hat{q}^3$, $\hat{y}^3$ and $\hat{q}\hat{y}^2$ are negligible, and where the constant terms act on the electrostatic force and charge voltage. Then, the non-dimensional variables and parameters are given as:

$$q = \frac{\hat{q}}{q_0}, \quad y = \frac{\hat{y}}{y_0}, \quad \tau = \omega_0 t, \quad \Omega = \frac{\omega}{\omega_0},$$
$$C_0 = \frac{\varepsilon_0 w y_0}{d}, \ \alpha = \frac{a}{m\omega_0}, \quad \beta = \frac{b}{m\omega_0^2}, \quad \omega_0 = \sqrt{\frac{b}{m}},$$
$$\gamma = \frac{c y_0^2}{m\omega_0^2}, \quad \eta = \frac{q_0^2}{2m\omega_0^2 C_0 y_0^2}, \ \mu = \frac{1}{R\omega_0 C_0}, \ F_0 = \frac{f_0}{m\omega_0^2 y_0} \tag{4}$$

The steady-state response of the set of equations (3) are determined by applying the harmonic balance method [43] by setting

$$y = a_0 + a_1 \cos(\Omega t) + a_2 \sin(\Omega t)$$
$$q = b_0 + b_1 \cos(\Omega t) + b_2 \sin(\Omega t). \tag{5}$$

Inserting equations (5) in equations (3) and equating the coefficients of $\cos(\Omega t)$ and $\sin(\Omega t)$ separately to zero (assuming that the terms due to higher frequencies can be neglected), one obtains:

$$\frac{3}{4}\gamma a_1^3 + \frac{3}{4}\gamma a_0 a_1 a_2^2 + \beta a_1 + 2\eta a_1 + 3\gamma a_0^2 a_1 + \alpha a_2 \Omega - a_1\Omega^2 - 6\eta a_0 a_1 + 4\eta b_0 a_1 - a_1\Omega^2 + 4\eta a_0 b_1 - 2\eta a_0 b_1 - 2\eta b_1 = F_0$$
$$\frac{3}{4}\gamma a_2^3 + \frac{3}{4}\gamma a_0 a_2 a_1^2 + \beta a_2 + 2\eta a_2 + 3\gamma a_0^2 a_2 - \alpha a_1 \Omega - a_1\Omega^2 - 6\eta a_0 a_2 + 4\eta b_0 a_2 - a_2\Omega^2 + 4\eta a_0 b_2 - 2\eta b_0 b_2 - 2\eta b_2 = 0$$
$$2\mu a_0 a_1 - \mu a_1(1 + b_0) + \mu(1 - a_0)b_1 + \Omega b_2 = 0$$
$$2\mu a_0 a_2 - \mu a_2(1 + b_0) + \mu(1 - a_0)b_2 - \Omega b_1 = 0. \tag{6}$$

Through algebraic manipulations, the amplitudes A and B satisfy the following nonlinear equations

$$\frac{9}{16}\gamma^2 A^6 + \frac{3}{2}\gamma F_2 A^4 + \left(F_2^2 + G_2^2\right)A^2 - F_0^2 = 0$$
$$B = \frac{\mu\sqrt{\rho^2 + \sigma^2\Omega^2}}{D_1} A, \tag{7}$$

where

$$A^2 = a_1^2 + a_2^2, \qquad B^2 = b_1^2 + b_2^2,$$
$$D_1 = \Omega^2 + \mu^2 (a_0 - 1)^2,$$
$$F_2 = \beta + 2\eta + 3\gamma a_0^2 - 6\eta a_0 + 4\eta b_0 - \Omega^2 - \frac{2\eta\mu\sigma\rho}{D_1},$$
$$G_2 = \alpha\Omega + \frac{2\eta\mu\Omega\sigma^2}{D_1},$$
$$\sigma = 2a_0 - b_0 - 1, \quad \text{and} \quad \rho = \mu\left(2a_0^2 - 3a_0 - a_0 b_0 + b_0 + 1\right). \tag{8}$$

Equation (7) will be used to plot the amplitude of the displacement and that of the charge versus the external force frequency. Comparison will then be made with the results obtained from the direct numerical simulation of the differential equations.

For the numerical calculation and simulation, the values of the parameters used in this case are given in Table 1.

Table 1. Characteristics of the harvester.

Characteristics	Value
Plates gap	$d = 8.85\ \mu$m
Plates width	$w = 10$ cm
Initial length	$y_0 = 10.0$ cm
Initial capacitance	$C_0 = 1$ mF
Initial charge	$q_0 = 5 \times 10^{-7}$ C
Proof mass	$m = 0.6$ g
Damping coefficient	$a = 0.01$ N s/m
Linear constant of the spring	$b = 0.02$ N/m
Nonlinear constant of the spring	$c = 0.01$ N/m^3
Air permittivity	$\varepsilon_0 = 8.85 \times 10^{-12}$ F/m

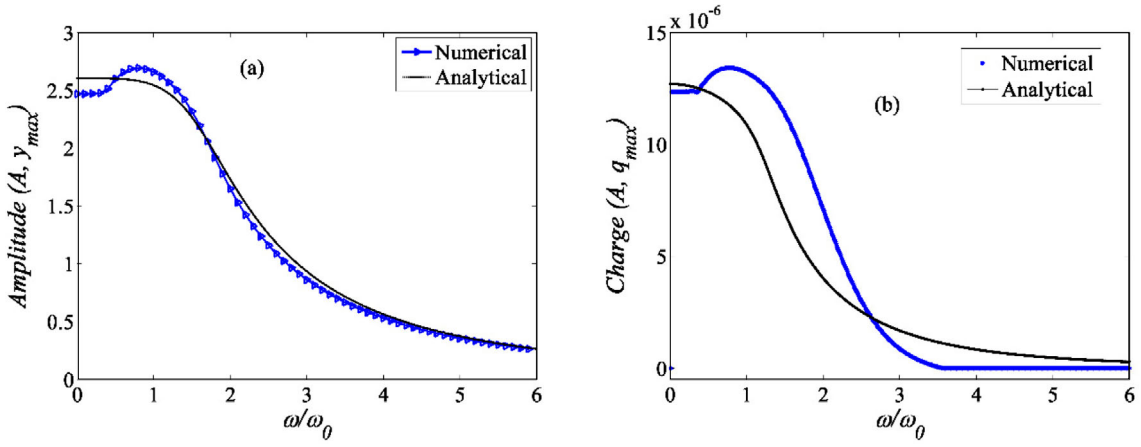

Fig. 2. Comparison of the analytical results and the numerical simulation results for the harvester with variable area. Displacement (a) and charge amplitude (b) versus the frequency for $f_0 = 0.2$ N, $R_{load} = 25$ kΩ, $a_0 = 0.01$, $b_0 = 0.006$ and other parameters in Table 1.

The plot in Figure 2 presents the displacement amplitude and charge amplitude versus the frequencies ratio obtained from the mathematical development above and from the numerical simulation of the differential equations (3) using the fourth order Runge-Kutta algorithm. There is a qualitative agreement between the results from the direct simulation of the differential equations and the results obtained from the analytical calculation. Both results indicate the decrease in amplitude when the frequency increases. However, there is a quantitative difference, which may be due to the approximation made when solving equations (3) analytically.

The next step is to analyse the effects of external parameters on the power generated by the harvester. In particular the variation of the power versus the amplitude f_0 and frequency $\Omega = \frac{\omega}{\omega_0}$ of the external force will be plotted and analysed. Moreover, the effects of the load resistance R_{load} will also be taken into consideration.

The power in the resistive load is defined as:

$$P_{load} = R_{load} I^2 = \frac{V_{load}^2}{R_{load}}. \tag{9}$$

The power and voltage are plotted in Figure 3. The voltage versus the excitation amplitude is plotted in Figure 3a, while Figure 3b presents the power versus the frequency. Figure 3c presents the variation of the power as a function of the frequency, while Figure 3d corresponds to the variation of the power versus the load resistance.

Figure 3a shows that the power increases almost linearly with the amplitude of the excitation. In Figures 3b and 3c, one can observe that the harvester voltage and power of 0.75 V and 22 μW are obtained respectively at the dimensionless frequency equal to 1.6. Above this value, a power decrease is observed to approach zero for high frequency. Figure 3d shows the output power versus the load resistance at the input vibration frequency of 1.6. For an applied excitation amplitude of $f_0 = 0.2$ N, the optimal power of 17.0 μW is obtained at a resistance of 26.0 kΩ.

We have also analyzed the same device, looking at whether it can deliver other types of dynamical behavior such as chaos. It happens that, for some selected parameters, transitions to different types of behaviors can be found, as represented in the bifurcation diagram of Figure 4. One finds that the system presents period-doubling bifurcation to chaos as well as abrupt transition to chaos or to periodicity.

2.2 Energy harvesters with variable permittivity

Now consider the possibility of varying the electrical permittivity of the material between the plates of the capacitor. This is normally done by laterally moving a dielectric material into and out of the space between the electrodes, as shown in Figure 5. This changes the effective value of the electric permittivity of the entire medium between the plates of the capacitor, and can be used to detect motion of the dielectric material (see Ref. [21] for some other details).

The mechanical part of the system is modeled as a spring-mass-damper system assembly for which m', a', b', and c' are the mass of the moveable dielectric material, the damping coefficient, the linear and nonlinear elastic constant respectively. When the external sinusoidal force $f_0 \cos(\omega t)$ is applied on the dielectric material, an electrostatic force is induced on the moveable plate.

To determine the effective electric permittivity, ε_{eff}, consider an instant in which the moving dielectric is neither totally removed from nor totally occupying the plate gap. Then the capacitor can be divided into two pieces. One piece has area A_1 and a dielectric with permittivity ε_1. The other portion has area A_2 and electric permittivity ε_2. The active area of the capacitor is fixed at A. Thus $A = A_1 + A_2$, and the length of the capacitor plates in the direction of motion of the dielectric is l. Since there is a single voltage difference between the plates, the two capacitor segments have the same voltage. Considering the basic equation of the standard form $q = \varepsilon Ae/d$,

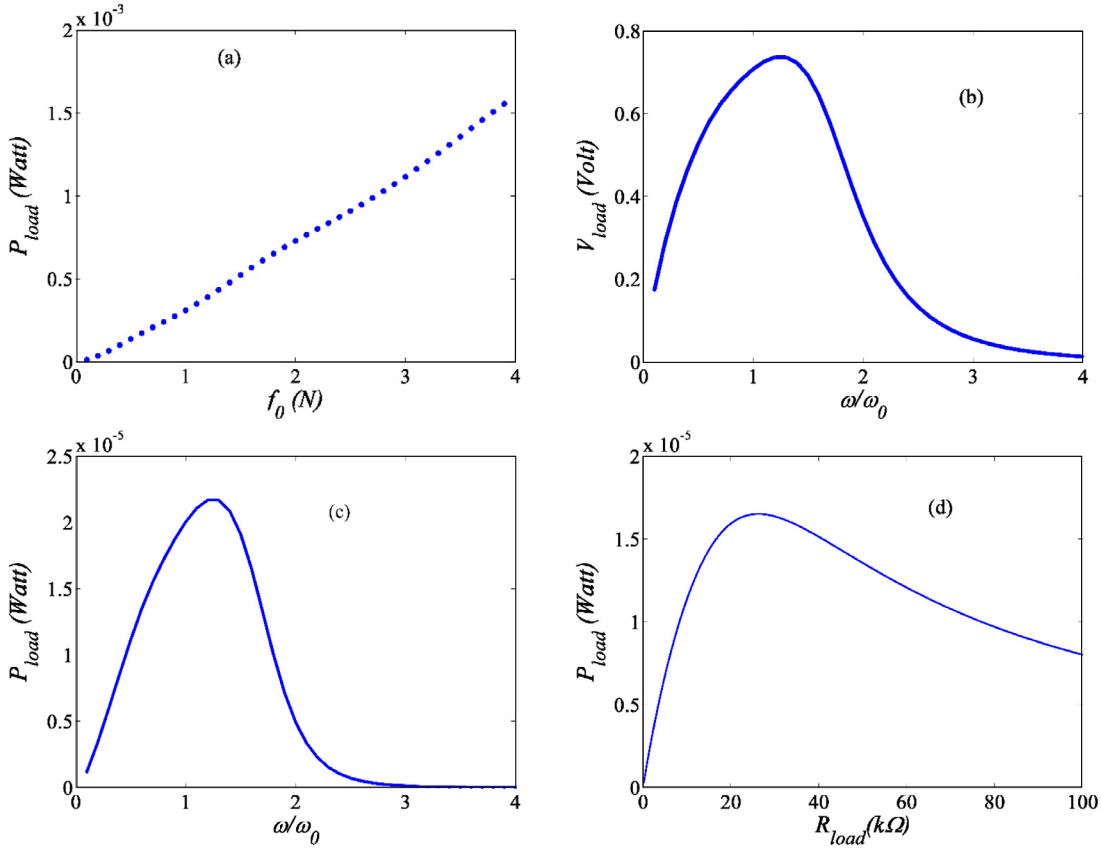

Fig. 3. (a) Voltage versus the amplitude of the excitation for $R_{load} = 25$ kΩ and $\omega/\omega_0 = 1.6$. (b) Voltage versus the frequency for $R_{load} = 25$ kΩ, $f_0 = 0.2$ N. (c) Power versus the frequency for $R_{load} = 25$ kΩ, $f_0 = 0.2$ N. (d) Power versus the load resistance for $f_0 = 0.2$ N and $\omega/\omega_0 = 1.6$.

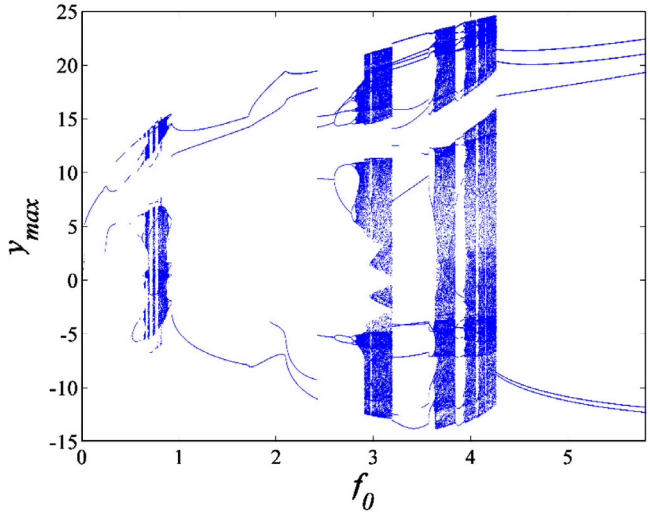

Fig. 4. Bifurcation diagram where the amplitude of external force varies with the following parameters $R_{load} = 10$ kΩ, $\Omega = \omega/\omega_0 = 3$, $a = 0.001$, $b = 0.002$, $c = 0.001$ and the same parameters as in Table 1.

we see that the effective electric permittivity is given by:

$$\varepsilon_{eff} = \frac{\varepsilon_1 A_1 + \varepsilon_2 A_2}{A} = \frac{\varepsilon_1 y + \varepsilon_2 (l-y)}{l}. \tag{10}$$

The constitutive relation of the voltage applied between the plates is written as:

$$V = e = \frac{qd}{[\varepsilon_1 y + \varepsilon_2 (l-y)]\, w}. \tag{11}$$

The induced electrostatic lateral force between the plates of the capacitor is given as:

$$F_{eletr} = -\frac{(\varepsilon_1 - \varepsilon_2)\, q^2 d}{2w\, [\varepsilon_1 Y + \varepsilon_2 (l-Y)]^2}. \tag{12}$$

The motion of the harvester in the case of varying permittivity is thus governed by the following equations:

$$\begin{aligned} &m'\ddot{Y} + a'\dot{Y} + b'Y + c'Y^3 - F_{eletr} = f_0 \cos(\omega t) \\ &R\dot{Q} + \frac{Q}{C} = 0 \quad \text{with} \quad C = \frac{\varepsilon_{eff} A}{d} = \frac{[\varepsilon_1 Y + \varepsilon_2 (l-Y)]\, w}{d} \end{aligned} \tag{13}$$

where w is the width of the plates, Y is the varying length of the dielectric material into and out of the space between the electrodes.

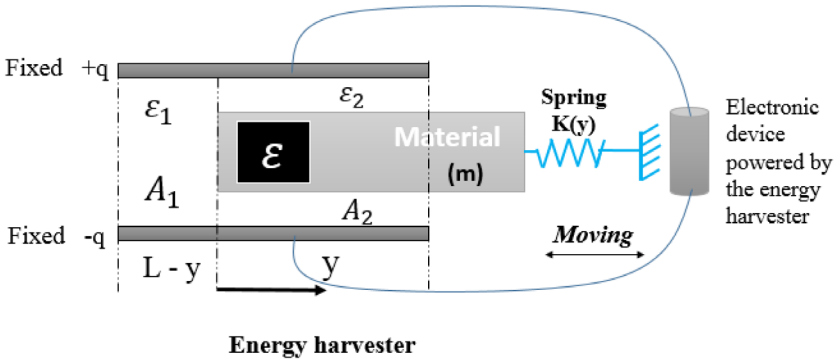

Fig. 5. Electrostatic energy harvester in which the permittivity varies spatially.

Proceeding as in the above case, one obtains the following set of equations

$$m_1\ddot{\hat{y}} + a_1\dot{\hat{y}} + b_1\hat{y} + c_1\hat{y} - F_{elect} = f_0\cos(\omega t)$$

$$F_{elect} = \frac{\chi d}{2w\varepsilon_2 l}\left[q_0^2 + 2\left(q_0\hat{q} - \frac{\chi}{l}q_0^2\hat{y}\right) + \left(\hat{q}^2 - 4\frac{\chi}{l}q_0\hat{q}\hat{y} + 3\frac{\chi^2}{l^2}q_0^2\hat{y}^2\right) + \left(6\frac{\chi^2}{l^2}\hat{q}\hat{y}^2 - 2\frac{\chi}{l}\hat{q}^2\hat{y} - 4\frac{\chi^3}{l^3}q_0^2\hat{y}^3\right)\right]$$

$$R\dot{\hat{q}} + \frac{d}{w\varepsilon_2 l}\left[q_0 + \left(\hat{q} - \frac{\chi}{l}q_0\hat{y}\right) + \left(\frac{\chi^2}{l^2}q_0\hat{y}^2 - \frac{\chi}{l}\hat{q}\hat{y}\right) + \left(\frac{\chi^2}{l^2}\hat{q}\hat{y}^2 - \frac{\chi^3}{l^3}q_0\hat{y}^3\right)\right] = 0. \quad (14)$$

Then, in the dimensionless form, the system with variable permittivity is governed by the set of equations (15):

$$\ddot{y} + \alpha_1\dot{y} + \beta_1 y + \gamma_1 y^3 - \eta_1\left[1 + 2\left(q - \chi y\right) + \left(q^2 - 4\chi qy + 3\chi^2y^2\right) + \left(6\chi^2qy^2 - 2\chi q^2y - 4\chi^3y^3\right)\right] = F_{01}\cos\left(\Omega_1\tau\right)$$

$$\dot{q} + \mu_1\left[1 + (q - \chi y) + \left(\chi^2y^2 - qy\right) + \left(\chi^2qy^2 - \chi^3y^3\right)\right] = 0. \quad (15)$$

The non-dimensional variables and coefficients are given in equation (16) as:

$$q = \frac{\hat{q}}{q_0}, \quad y = \frac{\hat{y}}{l}, \quad \tau = \omega_{01}t, \quad \Omega_1 = \frac{\omega}{\omega_{01}},$$

$$\chi = \frac{\varepsilon_1 - \varepsilon_2}{\varepsilon_2}, \quad \alpha_1 = \frac{a'}{m_1\omega_{01}}, \quad \beta_1 = \frac{b'}{m_1\omega_{01}^2},$$

$$\omega_{01} = \sqrt{\frac{b'}{m_1}}, \quad \gamma_1 = \frac{c'l^2}{m_1\omega_{01}^2}, \quad \eta_1 = \frac{\chi q_0^2}{2C_{01}m_1\omega_{01}^2 l},$$

$$\mu_1 = \frac{1}{RC_{01}\omega_{01}}, \; F_{01} = \frac{f_0}{m_1\omega_{01}^2 l}, \; C_{01} = \frac{\varepsilon_2 wl}{d}. \quad (16)$$

The steady-state response of the set of equations (15) is determined by applying the harmonic balance method as in the case of equations (3). Through algebraic manipulations, we find that the amplitudes A_1 and B_1 (of the displacement and charge) satisfy the following nonlinear algebraic equations:

$$\frac{9}{16}\gamma_1^2A_1^6 + \frac{3}{2}\gamma_1F_2'A_1^4 + \left(F_2'^2 + G_2'^2\right)A_1^2 - F_{01}^2 = 0$$

$$B_1 = \frac{\mu_1\sqrt{\left(\rho_1^2 + \Omega^2\Lambda^2\right)}}{D_2}A_1 \quad (17)$$

where

$$A_1^2 = a_1'^2 + a_2'^2, \qquad B_1^2 = b_1'^2 + b_2'^2,$$

$$D_1 = \Omega_1^2 + \mu_1^2\left(a_0 - 1\right)^2,$$

$$F_2' = \beta_1 + 3\gamma_1a_0'^2 + 4\eta_1\chi b_0 - 6\eta_1\chi^3a_0 + \eta_1\chi - \Omega_1^2 - \frac{2\eta_1\mu_1\rho_1\sigma_1}{D_1},$$

$$G_2' = \alpha_1\Omega_1 + \frac{2\eta_1\Omega_1\mu_1\sigma_1\Lambda}{D_2}, \quad \Lambda = \left(2\chi^2a_0 - \chi - b_0\right),$$

$$\sigma = 2\chi a_0 - b_0 - 1, \quad \text{and}$$

$$\rho = \mu\left(2\chi^2a_0^2 - 2\chi^2a_0 - \chi a_0 - a_0b_0 + b_0 + \chi\right). \quad (18)$$

As before, equation (17) will be used to plot the variation of the amplitudes of the mechanical displacement and charge as the frequency varies and comparison will be made with the numerical results.

We consider a parallel capacitor with a variable electric permittivity ε_{eff} as shown in Figure 5. The same values for the damping coefficient and elastic constants are taken as in the preceding case. The permittivity coefficients are $\varepsilon_1 = \varepsilon_0\varepsilon_{r1}$ and $\varepsilon_2 = \varepsilon_0\varepsilon_{r2}$ where $\varepsilon_{r1} = 1.0$ and $\varepsilon_{r2} = 80$ are the relative permittivity of air and water respectively.

The plot of Figure 6 shows some qualitative agreement between both curves. But one notices small quantitative disagreement at low frequencies in the case of charge amplitude in Figure 6b.

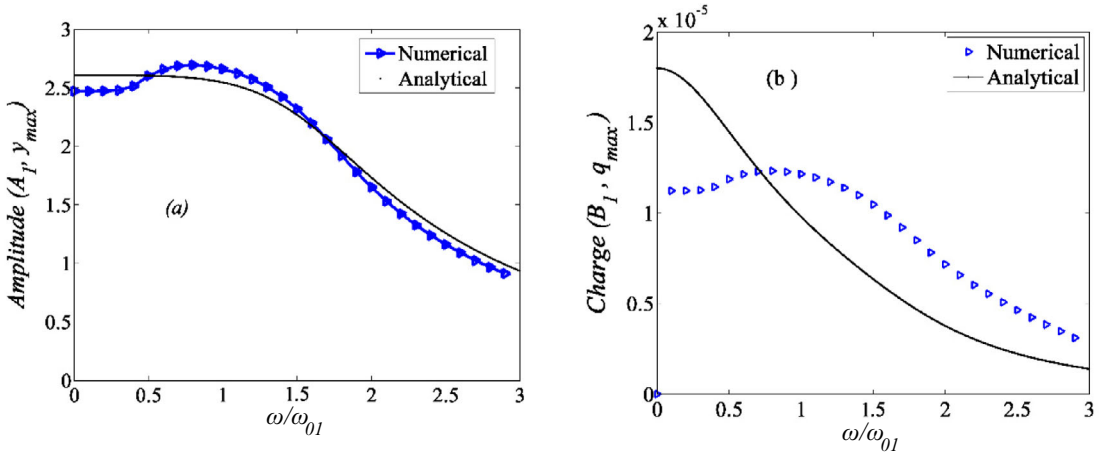

Fig. 6. Comparison of the analytical results and the numerical simulation results for the harvester with variable permittivity; (a) displacement and (b) charge amplitude versus the frequency.

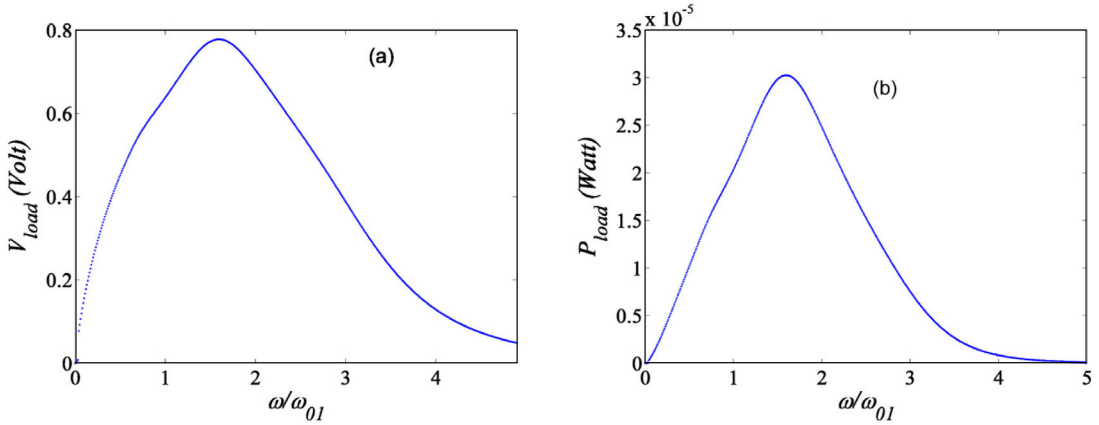

Fig. 7. Variation of the voltage (a) and power (b) versus the frequency in the case of the harvester with variable permittivity.

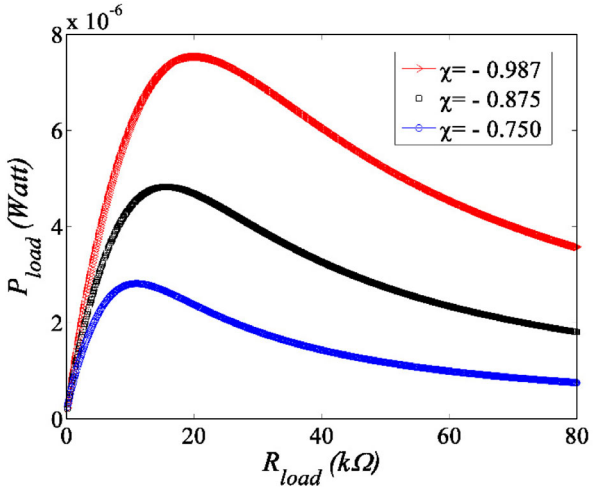

Fig. 8. Power generated in the resistive load versus the load resistance and different values of the ratio of the permittivity coefficients.

The variations of the voltage and power in terms of the parameters of this energy harvester are plotted in Figures 7 and 8. A maximal voltage of 0.78 V and a maximal electrical power of 30.0 μW are obtained at the resonance frequency of 1.6.

In order to analyse the effects of the difference in permittivity coefficients on the power generated by the harvester, we have used the following ratio $\chi = \frac{\varepsilon_1 - \varepsilon_2}{\varepsilon_2}$. The power output of the harvester is plotted for the following values of the ratio $\chi = -0.987$; -0.875; -0.750 corresponding respectively to $\varepsilon_{r1} = 1.0$; 10; 20 and for a fixed $\varepsilon_{r2} = 80$. It appears that the power increases with the ratio (consider the absolute value of the ratio).

As in the first case, it has been found that, by varying some parameters of this energy harvester, one can observe dynamics different from the periodic ones. The bifurcation diagram in Figure 9 presents various types of bifurcation points, including the transition to chaos.

3 Energy harvesters with cylindrical configuration

Up to now, we have considered only the geometry of parallel plate capacitor. Here we consider that we have a cylinder of radius r_1 centered inside a cylindrical shell with an outer radius r_2. This situation is shown in Figure 10.

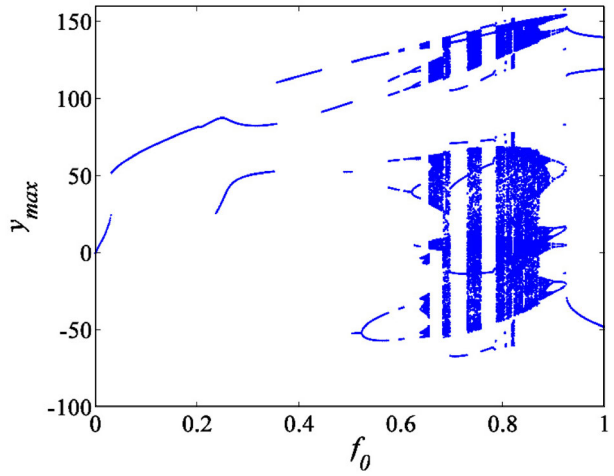

Fig. 9. Bifurcation diagram when the amplitude of the external force f_0 varies with fixed frequency $\Omega = \frac{\omega}{\omega_{02}} = 2$ and with the parameters $a = 0.001$, $b = 0.002$, $c = 0.001$.

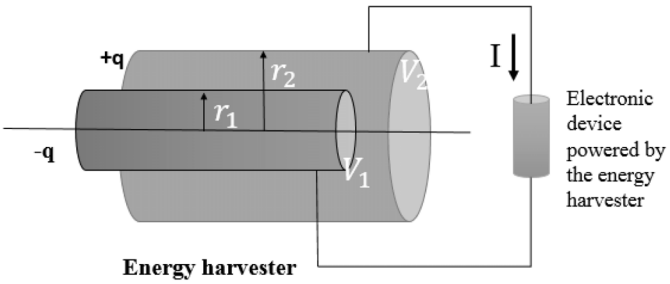

Fig. 10. Energy harvester capacitive transducer in which the radius ratio of cylindrical capacitor varies dynamically.

The radius ratio can be varied by allowing the outer or inner electrode to be made of a flexible material, thus deformable in the presence of periodic variation in pressure. The pressure can act either inside or outside the cylindrical structure. In this configuration, the equations should take into account the membrane partial differential equation. However, one can consider only one mode of vibration with frequency comparable to that of the varying pressure.

One can thus assume that the dynamics of the cylindrical shape electrostatic energy harvester is equivalent to that of a spring-mass-damper system for which m'', a'', b'', and c'' are the mass of the moveable outer radius electrode, the damping coefficient, the linear and nonlinear elastic constants respectively.

For this geometry, the capacitance is given by

$$C = \frac{2\pi\varepsilon l}{\ln(r_2/r_1)}, \tag{19}$$

where l is the cylinder length [44–48]. From the relation $q = CV$, we may write

$$V = e = \frac{q\ln(r_2/r_1)}{2\pi\varepsilon l}. \tag{20}$$

This expression suggests that there are three control parameters which can be varied mechanically in order to induce a voltage, or which can be stimulated to change the voltage: the permittivity, the cylinder length, and the radius ratio r_2/r_1. The permittivity can be varied in the same manner as described for the parallel plate geometry. Similarly, the cylinder length can be made a function of time by moving one of the electrodes.

We study here the case in which the inner electrode radius is fixed and the outer radius varies. We choose this particular case as it represents the appropriate departure from the parallel plate geometry.

Let us call the following constitutive relations for the voltage and the electrostatic radial force F_{elect}:

$$V = e = \frac{Q\ln(r_2/r_1)}{2\pi\varepsilon l}, \tag{21}$$

$$F_{elect} = \frac{Q^2}{4\pi\varepsilon l r_2}. \tag{22}$$

Thus the equations of motion of the system are obtained as:

$$m_2\ddot{r}_2 + a_2\dot{r}_2 + b_2 r_2 + c_2 r_2^3 + \frac{Q^2}{4\pi\varepsilon l r_2} = f_0\cos(\omega t)$$

$$R\dot{Q} + \frac{Q}{c} = 0 \qquad \text{with} \qquad C = \frac{2\pi\varepsilon l}{\ln(r_2/r_1)}. \tag{23}$$

Using the same development as in the first case, one obtains that the equations describing the variations of the system from the initial state are

$$m_2\ddot{\hat{r}}_2 + a_2\dot{\hat{r}}_2 + b_2\hat{r}_2 + c_2\hat{r}_2^3 + F_{elect} = f_0\cos(\omega t)$$

$$F_{elect} = \frac{1}{4\pi\varepsilon l r_2}\left[q_0^2 + \left(2q_0\hat{q} - \frac{q_0^2}{r_{20}}\hat{r}_2\right)\right.$$

$$\left. + \left(\hat{q}^2 + \frac{q_0^2}{r_{20}}\hat{r}_2^2 - \frac{q_0}{r_{20}}\hat{q}\hat{r}_2\right) + \left(2\frac{q_0}{r_{20}^2}\hat{q}\hat{r}_2^2 - \frac{1}{r_{20}}\hat{q}^2\hat{r}_2 - \frac{q_0^2}{r_{20}^3}\hat{r}_2^3\right)\right]$$

$$R\dot{\hat{q}} + \frac{1}{2\pi\varepsilon l}\left\{q_0\ln(r_{20}/r_1) + \left[\frac{q_0}{r_{20}}\hat{r}_2 + \hat{q}\ln(r_{20}/r_1)\right]\right\} = 0. \tag{24}$$

Then, in the dimensionless form, the system is governed by the set of equations rewritten as:

$$\ddot{r}_2 + \alpha_2\dot{r}_2 + \beta_2 r_2 + \gamma_3 r_2^3 + F_{electr} = F_{02}\cos(\Omega_2\tau)$$

$$F_{electr} = \eta_2\left[1 + (2q - r_2) + \left(q^2 + r_2^2 - 2qr_2\right)\right.$$

$$\left. + \left(2qr_2^2 - q^2 r_2 - r_2^3\right)\right]$$

$$\dot{q} + \mu_2\left\{1 + \left[q + \frac{r_2}{\ln(r_{20}/r_1)}\right]\right\} = 0 \tag{25}$$

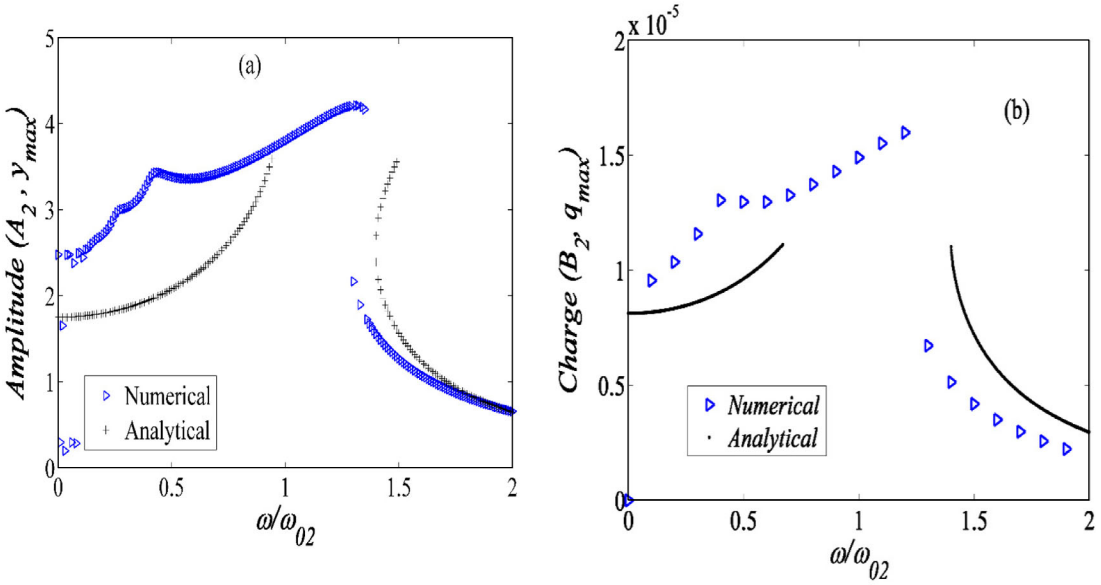

Fig. 11. Amplitude of the outer membrane deformation (a) and corresponding charge amplitude (b) versus the frequency of the external force.

with the following dimensionless parameters

$$q = \frac{\hat{q}}{q_0}, \qquad r_2 = \frac{\hat{r}_2}{r_{20}},$$

$$\tau = \omega_{02} t, \qquad \Omega_2 = \frac{\omega}{\omega_{02}},$$

$$C_{02} = \frac{2\pi\varepsilon h}{\ln(r_{20}/r_1)}, \qquad \alpha_2 = \frac{a_2}{m_2\omega_{02}},$$

$$\beta_2 = \frac{b_2}{m\omega_{02}^2}, \qquad \omega_{02} = \sqrt{\frac{b_2}{m_2}},$$

$$\gamma_2 = \frac{c_2 r_{20}^2}{m_2\omega_{02}^2}, \qquad \eta_2 = \frac{q_0^2}{2C_{02}m_2\omega_{02}^2 r_{20}^2 \ln(r_{20}/r_1)},$$

$$\mu_2 = \frac{1}{C_{02}R\omega_{02}}, \qquad F_{02} = \frac{f_0}{m_2\omega_{02}^2 r_{20}}. \tag{26}$$

Using the harmonic balance method, the amplitude of the displacement and that of the charge satistfy the following set of nonlinear algebraic equations:

$$\frac{9}{16}\gamma_2^2 A_2^6 + \frac{3}{2}\gamma_2 F_2'' A_2^4 + \left(F_2''^2 + G_2''^2\right) A_2^2 - F_{02}^2 = 0$$

$$B_2 = \frac{\mu_2}{D_2 \ln(r_{20}/r_1)} A_2 \tag{27}$$

where

$$A_2^2 = a_1''^2 + a_2''^2, \quad B_2^2 = b_1''^2 + b_2''^2$$

$$D_2 = \mu_2^2 + \Omega_2^2, \quad \rho_2 = (-a_0 + b_0 + 1)$$

$$F_2'' = \beta_2 + 3\gamma_2 a_0''^2 + 2\eta_2 a_0 - 2\eta_2 b_0 - \eta_2 - \Omega_2^2 - \frac{2\eta_2\mu_2^2\rho_2}{D_2 \ln(r_{20}/r_1)}$$

$$G_2'' = \alpha_2\Omega_2 + \frac{2\eta_2\mu_2\Omega_2\rho_2}{D_2 \ln(r_{20}/r_1)}. \tag{28}$$

Table 2. Model parameters for the cylindrical energy harvester.

Parameters	Prototype value
Proof mass	$m_2 = 6$ g
Static outer radius	$r_{20} = 12$ cm
Variable inter radius	$r_1 = 6$ cm
Cylindrical length	$l = 30$ cm
Initial capacitance	$C_0 = 1$ μF
Damping coefficient	$a = 0.01$ N s/m
Linear Spring stiffness	$b = 0.01$ N m^{-1}
Nonlinear Spring stiffness	$c = 0.01$ N m^{-3}
Load resistance	$R_{load} = 10\ \Omega \ldots 100$ kΩ

Equation (17) will be used to plot the amplitude of the displacement versus the external force frequency. Comparison will then been made with the results obtained from the direct numerical simulation of the differential equations.

We consider a cylinder of static radius $r_1 = 6$ cm centered inside a cylindrical shell with a variable outer radius r_2 varying around a static radius term $r_{20} = 12$ cm, as shown in Figure 10. The length of the cylindrical capacitor is $l = 30$ cm. The initial capacitance is $C_0 = 1$ μF, with the initial charge of $q_0 = 5 \times 10^{-7}$ C, the mass of a movable outer membrane is assumed to be $m_2 = 6$ g. The damping coefficient and elastic constants are those chosen for the two first cases. Table 2 gives the values of the other parameters.

The plot in Figure 11 shows the value of the amplitude of the displacement of the outer membrane versus the frequencies ratio. One first observes an increase of amplitudes. This is followed by a decrease when the frequency increases.

Figure 12 presents the variation of the power in the load versus the frequency of the external force (Fig. 12a) and versus the load resistance (Fig. 12b) for different

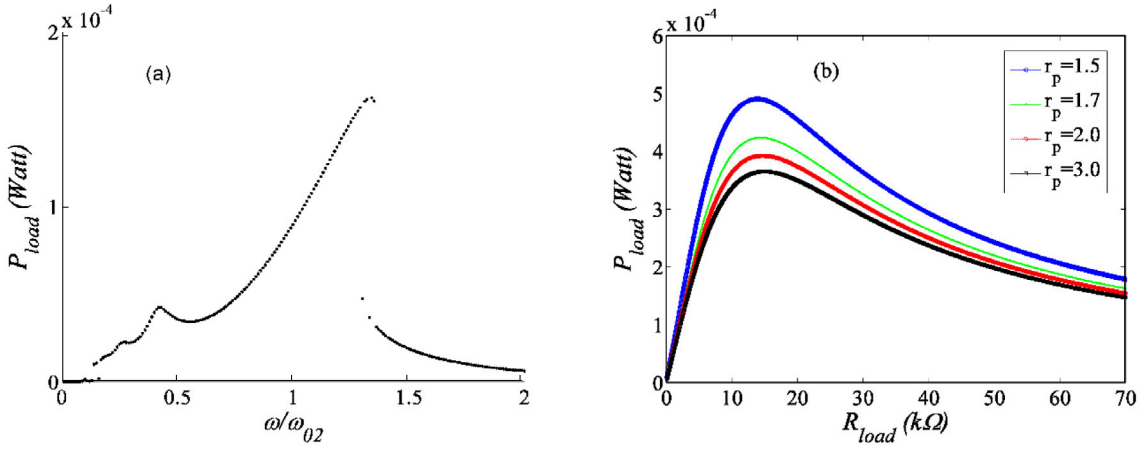

Fig. 12. Variation of the power produced by the cylindrical electrostatic energy harvester versus the frequency (a) and the load resistance (b) for different values of the radius ratio.

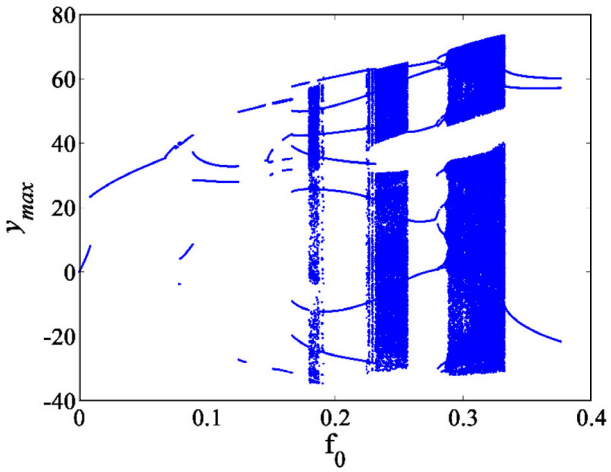

Fig. 13. Bifurcation diagram when the amplitude of the external force f_0 varies with the frequency $\Omega = \frac{\omega}{\omega_{02}} = 2$ and $a = 0.001$, $b = 0.002$, $c = 0.001$.

values of the initial radius ratio $r_p = (r_{20}/r_1)$. One finds that the power increases with the increase of radius ratio r_p. One also observes that the increases of r_p results in the increase of the value of the frequency leading to the maximal power.

Again, as in the preceding cases, the cylindrical electrostatic energy harvester can generate chaotic dynamics as it appears in the bifurcation diagram in Figure 13.

4 Conclusion

In summary, we have analyzed the power generated by electrostatic energy harvesters with variable area, variable permittivity, and variable radius. The algebraic equations for the amplitude of the electrical and mechanical components of each configuration have been established. The power generated by each configuration has been plotted in terms of appropriate parameters such as the frequency and value of the load resistance. In all the configurations analysed here, it has been found an increase of the power with the frequency of the external excitation and with the load resistance until a maximal value, after which it decreases as those parameters increase. It has also been shown that these devices can show period-doubling and sudden transitions to chaos. For the electrostatic harvester with variable permittivity, it has been found the power strongly depends on the relative ratio between the two media inserted in the electrostatic device. In the case of a cylindrical electrostatic harvester with variable radius, it has been established that the power increases with the ratio between the outer and inner radi of the cylinder.

The results obtained in this paper shed light on the electrostatic energy harvester with variable parameters. The configurations studied here may find application in fields such as bio-engineering, where the cylindrical configuration could be attached to blood vessel, thus providing energy for artificial organs or artificial pacemakers [49].

Author contribution statement

This work is part of the Ph.D. work of D. Tokoue Ngatcha supervised by P. Woafo.

References

1. I. Sari, T. Balkan, H. Kulah, J. MEMS **19**, 14 (2010)
2. S.P. Beeby, R.N. Torah, M.J. Tudor, P. Glynne-Jones, T. O'Donnell, C.R. Saha, S. Roy, J. Micromech. Microeng. **17**, 1257 (2007)
3. B.S. Joyce, J. Farmer, D.J. Inman, Wind Energ. **17**, 869 (2014)
4. P. Glynne-Jones, M.J. Tudor, S.P. Beeby, N.M. White, Sens. Actuators A **110**, 344 (2004)
5. F. Cottone, M. Mattarelli, H. Vocca, L. Gammaitoni, Eur. Phys. J. Special Topics **224**, 2855 (2015)
6. S. Roundy, E.S. Leland, J. Baker, E. Carleton, E. Reilly, E. Lai, V. Sundararajan, Per. Comp. IEEE **4**, 28 (2005)
7. G. Poulin, E. Sarraute, F. Costa, Sens. Actuators A **116**, 461 (2004)

8. Z.L. Wang, J. Song, Science **312**, 242 (2006)
9. Y. Qin, X. Wang, Z.L. Wang, Nature **451**, 809 (2008)
10. S. Roundy, P.K. Wright, Smart Mater. Struct. **13**, 1131 (2004)
11. M. Marzencki, Y. Ammar, S. Basrour, Sens. Actuators A **145**, 363 (2008)
12. M. Renaud, K. Karakaya, T. Sterken, P. Fiorini, C. Van Hoof, R. Puers, Sens. Actuators A **145**, 380 (2008)
13. L. Garbuio, M. Lallart, D. Guyomar, C. Richard, D. Audigier, Ind. Elect. IEEE Trans. **56**, 1048 (2009)
14. S. Meninger, J.O. Mur-Miranda, R. Amirtharajah, A.P. Chandrakasan, J.H. Lang, VLSI IEEE Trans. **9**, 64 (2001)
15. P. Miao, P.D. Mitcheson, A.S. Holmes, E.M. Yeatman, T.C. Green, B.H. Stark, Microsyst. Tech. **12**, 1079 (2006)
16. A.M. Paracha, P. Basset, F. Marty, A.V. Chasin, P. Poulichet, T. Bourouina, arXiv:0802.3063 (2008)
17. G. Despesse, T. Jager, C. Jean-Jacques, J.M. Léger, A. Vassilev, S. Basrour, B. Charlot, in *Proc. of DTIP'05, 2005*, pp. 386–390
18. P. Miao, P.D. Mitcheson, A.S. Holmes, E.M. Yeatm, T.C. Green, B.H. Stark, Microsyst. Tech. **12**, 1079 (2006)
19. M.E. Kiziroglou, C. He, E.M. Yeatman, Ind. Elect. IEEE Trans. **56**, 1101 (2009)
20. B.C. Yen, J.H. Lang, Circ. Syst. I: Regular Papers, IEEE Tran. **53**, 288 (2006)
21. M. Mizumo, D.G. Chetwynd, J. Micromech. Microeng. **13**, 209 (2003)
22. P. Basset, D. Galayko, A.M. Paracha, F. Marty, A. Dudka, T. Bourouina, J. Micromech. Microeng. **19**, 115025 (2009)
23. D. Hoffmann, B. Folkmer, Y. Manoli, J. Micromech. Microeng. **19**, 094001 (2009)
24. D.S. Nguyen, E. Halvorsen, G.U. Jensen, A. Vogl, J. Micromech. Microeng. **20**, 125009 (2010)
25. K.O. Owusu, F.L. Lewis, in *2nd IEEE International Conference on Nano/Micro Eng. Molec. Syst., NEMS'07, 2007*, pp. 1190–1195
26. G. Taylor, Proc. R. Soc. London A **306**, 423 (1968)
27. H.C. Nathanson, W.E. Newell, R.A. Wickstrom, J.R. Davis Jr., Electron Devices, IEEE Trans. **14**, 117 (1967)
28. Y. Bai, Z. Havránek, P. Tofel, C. Meggs, H. Hughes, T.W. Button, Eur. Phys. J. Special Topics **224**, 2675 (2015)
29. Y. Zhang, R. Zheng, T. Kaizuka, D. Su, K. Nakano, M.P. Cartmell, Eur. Phys. J. Special Topics **224**, 2687 (2015)
30. R.C. Batra, M. Porfiri, D. Spinello, Eng. Analy. Bound Elements. **30**, 949 (2006)
31. E. Yildiring, H. Külah, Microfluid. Nanofluid. **13**, 107 (2012)
32. A. Dudka, P. Basset, F. Cottone, E. Blohina, D. Galayko, J. Phys.: Conf. Ser. **476**, 012127 (2013)
33. P. Basset, D. Galayko, F. Cottone, R. Guillemet, E. Blokhina, F. Marty, T. Bourouina, J. Micromech. Microeng. **24**, 035001 (2014)
34. S. Roundy, P.K. Wright, J.M. Rabaey, *Ener. Scav. Wireless Sens. Networks With Special Focus on Vibrations*, 1st ed. (Norwell, MA: Kluwer Academic Publishers, 2004)
35. S. Meninger, J.O. Mur-Miranda, R. Amirtharajah, A.P. Chandrakasan, J.H. Lang, Very Large Scale Integration (VLSI) Syst. IEEE Trans. **9**, 64 (2001)
36. E.O. Torres, G.A. Rincón-Mora, Circ. Syst. I: Regular Papers IEEE Trans. **56**, 1938 (2009)
37. A. Kempitiya, D.A. Borca-Tasciuc, M.M. Hella, Power Elec. IEEE Trans. **28**, 609 (2013)
38. C.H. Nguyen, D.S. Nguyen, E. Halvorsen, J. Phys.: Conf. Ser. **557**, 012114 (2014)
39. P.V. Malaji, S.F. Ali, Eur. Phys. J. Special Topics **224**, 2823 (2015)
40. Y. Naruse, N. Matsubara, K. Mabuchi, M. Izumi, S. Suzuki, J. Micromech. Microeng. **19**, 094002 (2009)
41. C.P. Le, E. Halvorsen, J. Micromech. Microeng. **22**, 074013 (2012)
42. T. Galchev, R. Raz, O. Paul, in *IEEE 26th Int. Conf. Micro Electro Mech. Syst. 2013*, pp. 102–105
43. A.H. Nayfeh, D.T. Mook, *Nonlinear Oscillations* (John Wiley and Sons, New York, 1979)
44. P. Lorrain, D. Corson, *Electromagnetic fields and waves* (Freeman & Co Ltd, New York, 1970)
45. E.M. Purcell, *Electricity and magnetism* (McGraw-Hill, New York, 1965)
46. W.H. Hayt Jr., *Engineering Electromagnetics* (McGraw-Hill, New York, 1981)
47. L. Eyges, *The classical Electromagnetic Field* (Addison-Wesley, Reading, MA, 1972)
48. I.J. Busch-Vishniac, *Electromechanical sensors and actuators* (Springer, Berlin, 1999)
49. P.R. Nwagoum Tuwa, P. Woafo, J. Mech. Med. Biol. **16**, 1650073 (2016)